Copyright Undertaking

CORE@SHELL-STRUCTURED NANOMATERIALS AS CATALYTIC ELECTRODES FOR RECHARGEABLE LITHIUM-BASED BATTERIES

MAN LONG HIN

MPhil

The Hong Kong Polytechnic University

2021

The Hong Kong Polytechnic University

Department of Electrical Engineering

Core@Shell-Structured Nanomaterials as Catalytic Electrodes for Rechargeable Lithium-Based Batteries

Man Long Hin

A thesis submitted in partial fulfilment of the
requirements for the degree of Master of Philosophy

June 2021

CERTIFICATE OF ORIGINALITY

I hereby declare that this thesis is my own work and that, to the best of my knowledge and belief, it reproduces no material previously published or written, nor material that has been accepted for the award of any other degree or diploma, except where due acknowledgement has been made in the text.

____(Signed)

________________Man Long Hin________________(Name of Student)

Abstract

This thesis reports the experimental and theoretical investigations on a promising type of electrocatalytic nanomaterials (i.e., electrocatalysts), featuring different configurations of core@shell structure and physicochemical properties. It also presents the development of the nanomaterials into novel catalytic electrodes and their rechargeable lithium (Li)-based batteries. The nanomaterials, catalytic electrodes, and Li-based batteries under study include:

(1) $FeSn_2$@C nanocapsules, having a $FeSn_2$ stannide alloy nanoparticle core coated by a carbon onion-like layer shell, as an improved electrocatalytic anode for lithium-ion batteries (LIBs); and

(2) Mn_3O_4@C mesoporous multihollow microspheres, having a Mn_3O_4 manganese oxide nanoparticle-assembled hollow microsphere core coated by a carbon spongy-like layer shell, as an enhanced electrocatalytic cathode for lithium–oxygen batteries (LOBs).

The introduction of the specific configurations of the core@shell structure aims to inspire an interesting and appropriate set of physicochemical properties in the nanomaterials and, hence, higher electrochemical performance in the catalytic electrodes for enabling emerging rechargeable batteries and energy storages. Proposals of the theoretical formation mechanism of materials are suggested by adopting the observations of the physicochemical properties. Through establishing electrochemical models and applying scientific computations, the experimental observations are analysed, and the underlying reaction mechanisms are revealed. The original work, findings, and contributions are summarised in the 'Contributions' section.

Contributions

The original work, findings, and contributions are summarised as follows:

(1) $FeSn_2@C$ nanocapsules with a confined size range of sub-50 nm are synthesized via an in-situ arc-discharge process. They are evaluated physiochemically and electrochemically in comparison with $FeSn_2$ nanoparticles as an improved stannide-based electrocatalytic anode material for LIBs. The use of the in-situ arc-discharge process allows a facile one-pot procedure for forming crystalline $FeSn_2$ stannide alloy nanoparticle cores coated by carbon onion-like layer shells of ~1 nm thickness and defective surface morphology in addition to confined crystal growth of the $FeSn_2$ nanoparticle cores. A formation mechanism is proposed to describe the confined crystal growth of the $FeSn_2$ nanoparticle cores and the formation of the core@shell structure. The LIB cells assembled using the proposed $FeSn_2@C$ nanocapsules as the electrocatalytic anodes exhibit improved electrochemical performance in higher rate capacity, reversible capacity, and cyclability compared to their $FeSn_2$ nanoparticle anode-based LIB cells counterpart. The observed performance improvements are ascribed to the synergetic effects of the enabling of a reversible lithiation process during charge-discharge of the LIB cells by the $FeSn_2$ nanoparticle cores, as well as the protection of the $FeSn_2$ nanoparticle cores from volume change-induced

pulverization and solid electrolyte interphase-induced passivation by the carbon onion-like layer shells.

(2) As an intermediary for the subsequent synthesis of the Mn_3O_4@C mesoporous multihollow microspheres as an enhanced electrocatalytic cathode for LOBs, MnO_2/Mn_2O_3 hybrid manganese oxide nanoparticle-assembled hollow microcages are firstly prepared via a specific templateless solvothermal process. For comparison purposes, Mn_3O_4 manganese oxide nanoparticle-assembled hollow microcages are also prepared using a traditional carbon sacrificial template process. The proposed templateless solvothermal method shows the distinct advantages of increasing product yield by 30–35% and reducing preparation time by four days. The physiochemical properties of the as-prepared MnO_2/Mn_2O_3 and Mn_3O_4 hollow microcages are evaluated, and the electrochemical performances of their resulting cathode-based LOB cells are characterised. The proposed MnO_2/Mn_2O_3 hollow microcage cathode-based LOB cells demonstrate much higher electrochemical performance than the Mn_3O_4 ones due to the comparatively larger pore volume, higher electroconductivity, and lower kinetic resistance at the electrode/electrolyte interfaces.

(3) Mn_3O_4@C mesoporous multihollow microspheres, consisting of a Mn_3O_4 manganese oxide nanoparticle-assembled hollow microsphere core of ~0.6 μm average diameter coated by a carbon spongy-like layer shell of ~3 nm thickness and porous surface morphology, are synthesized using the intermediary

MnO_2/Mn_2O_3 hollow microcages described in (2) via a hydrothermal process and a carbonisation process. Their physicochemical properties are evaluated for further comparison with the MnO_2/Mn_2O_3 and Mn_3O_4 hollow microcages in (2). The use of the intermediary MnO_2/Mn_2O_3 hollow microcages, instead of the direct synthesis of the Mn_3O_4 hollow microcages as the core followed by the coating of a carbon layer as the shell, is found to effectively prevent the core material from structural deformation during the high-temperature coating of the carbon layer shell. The LOB cells assembled using the proposed Mn_3O_4@C mesoporous multihollow microspheres as the electrocatalytic cathodes show even higher electrochemical performance than their parental MnO_2/Mn_2O_3 hollow microcage cathode-based LOB cells. An investigation into the formation mechanism, the reversible oxygen reduction reaction (ORR)–oxygen evolution reaction (OER) activity, and the post-mortem results reveals that the tactful combination of the electrocatalytic Mn_3O_4 hollow microsphere core with the electroconductive carbon spongy-like layer shell can simultaneously and effectively enable substantial amounts of electrocatalytic active surface sites and high electroconductivity to enhance and stabilise the ORR–OER process against the accumulation and passivation of the insulating discharge product Li_2O_2. Moreover, the porous and thin surface morphology of the electroconductive carbon shell can simultaneously secure O_2 accommodation, allow electrocatalysis, promote electro-conduction, and protect the electrocatalytic Mn_3O_4 hollow microsphere core from pulverization and aggregation.

(4) To obtain an insight into the enhanced electrocatalytic activity, the density functional theory (DFT) calculations are implemented with surface slab models from an atomistic-scale point of view. The binding energies between the cathode materials and the reactive species are examined to study the initial ORR mechanism. The higher adsorption energy for O_2, LiO_2, and Li_2O_2 on the surface of the proposed Mn_3O_4@C mesoporous multihollow microspheres than the parental MnO_2/Mn_2O_3 hollow microcages indicates the existence of a more energetic ORR activity in the Mn_3O_4@C mesoporous multihollow microspheres with an enhanced discharge capacity. The results of the partial electronic densities of states show that the proposed Mn_3O_4@C mesoporous multihollow microspheres have prominent spin-splitting states of the Mn-atom 3d orbital around the Fermi-level, suggesting a more vigorous electrocatalytic activity with a much higher affinity to all reactive species.

List of Publications

[1] D. Han, A. Chatterjee, L. H. Man, and S. W. Or, "In-situ arc discharge-derived $FeSn_2$/onion-like carbon nanocapsules as improved stannide-based electrocatalytic anode materials for lithium-ion batteries," *Catalysts*, vol. 9, issue 11, article 950, Nov. 2019.

[2] L. H. Man, Z. Sadighi, X. Liang, S. W. Or, and J. Dai, "MnO_2/Mn_2O_3 hybrid manganese oxide nanoparticle hollow microcages-derived Mn_3O_4@C microspheres with mesoporous multi-hollow core@shell structure as improved electrocatalytic cathodes for Li–O_2 batteries," *Electrochimica Acta*, 2021. (Under preparation)

Acknowledgements

I would like to express my appreciation to my chief supervisor, Professor Siu Wing Or, for his guidance through my MPhil study. He taught me a great deal of academic knowledge, thinking methods, and how to become a leader in the future. I would also like to thank my co-supervisor, Professor Jiyan Dai, for his valuable advice and assistance. Without their support, this work may not be possible.

Thanks are also due to my research colleagues: Dr Zoya Sadighi, Dr Johnny Wang, Dr Amrita Chatterjee, Dr Ronnie Zhang, and Mr. Patrick Yip, for providing technical advices and supports. It is a pleasure to study with them. To Ms. Cindy Pang in the AP department, who has helped in SEM and XRD measurements, thank you very much. To Dr Xiongyi Liang, who has provided a great support in computational stimulation, I give my sincere thanks.

Last, but not least, I would like to extend my appreciation to my family and friends for their encouragement during my study period.

Table of Contents

Chapter 2 $FeSn_2$@C Nanocapsules as Anode for Lithium-Ion Batteries 30

Chapter 4 Mn_3O_4@C Microspheres as Cathode for Lithium–Oxygen Batteries 82

List of Figure Captions

List of Table Captions

List of Symbols and Their Units

Symbol	***Description***	***Unit***
e	Specific Energy (Gravimetric Energy Density)	W·h/kg or J/kg
u	Energy Density (Volumetric Energy Density)	J/m^3
U	Energy	J
m_u	Unit Mass	kg
V	Volume	m^3
C_s	Specific Capacity	Ah/kg
t	Time	s
I_d	Discharge Current	A
e/t	Specific Power	W/kg
d	Interplanar spacing of crystallographic planes	m
$\Delta H'$	Effective Heat of Formation	kJ·(mol·atom)$^{-1}$
R_{ct}	Interface Charge Transfer Resistance	Ω
R_{s}	Ohmic Resistance	Ω
Z_{w}	Warburg Impedance	Ω
CPE	Constant Phase Element	F

Symbol	***Description***	***Unit***
P	Pressure	Pa
P/P_0	Relative Pressure	-
θ	Angle	°
dV(r)	Pore Size Distribution	cm^3 g^{-1} nm^{-1}
CPE$_{dl}$	Double Layer Constant Phase Element	F
σ	Electrical Conductivity	S/m
τ	Average Crystalline Size	m
β	Full Width at Half Maximum	°
λ	Wavelength	m
K	Shape Factor	-
I_D/I_G	Intensity Ratio	-
R_e	Electrolyte Ionic Resistance	Ω
$V_{\text{ext}}(\mathbf{r})$	External Potential Functional	V
$\mathbf{r}$	Specific Point	-
E_{11}	Interaction between Nuclei	J
$n(\boldsymbol{r})$	Density for the Non-interacting System	kg/m^3
$T_S[n]$	Particle Kinetic Energy	J
$E_H[n]$	Hartree Energy	J

Symbol	***Description***	***Unit***
$E_{xc}[n]$	Exchange Correlation	J
$\varepsilon_{xc}([n],\boldsymbol{r})$	Energy for one electron at point **r**	J
E_{Total}	Total Energy of Adsorption System	J
E_{Surface}	Energy of Surface	J
$E_{\mathrm{O_2}/Li}$	Energy of Triple-stated Oxygen Molecule or Lithium in Bulk Metal State	J
γ	Relative Surface Energy	-
E_{bulk}	Bulk Energy per Atom	J
E_{slab}	Total Energy of Surface Slab	J
A	Area of Surface	m^2
N	Atoms Number in the Surface Slab	-
E_f	Energy at Fermi-level	eV

Chapter 1 Introduction

1.1 Rechargeable Lithium-based Batteries

1.1.1 Features

Lithium-based batteries (LBBs) have received a tremendous amount of attention from both scientists and engineers over the last three decades because of the tremendous desire to develop economical and effective energy storage devices to satisfy the technology requirement of society [1]–[3]. Compared with other energy storage devices, rechargeable LBBs have been considered as one of the most suitable electrical energy storage options and near-term renewable energy sources solution [4]–[7].

LBBs are generally considered as cells that consist of two electrodes (cathode and anode), with at least one of them are made of lithium-related materials, electrolyte, as well as an electrical-insulated separator that is permeable for ions and electrolyte to move between [8], [9]. The Rechargeable LBB family includes majorly three types of batteries: lithium-ion batteries (LIBs), lithium–oxygen batteries (LOBs), and lithium–sulfur batteries (LSBs) [9]. Although the three types of batteries consist of similar components, the electrochemistry between them is distinct. Even more, LOBs required a continuous supply of oxygen to function. This thesis will focus on the discussion of LIBs and LOBs.

The milestones of the development in rechargeable batteries are briefly summarized in Table 1.1:

Table 1.1. A summary of rechargeable batteries and their specific energies and energy densities.

Rechargeable Batteries	e $(\mathbf{W \cdot h/kg})$	u $(\mathbf{W \cdot h/L})$	**Comments**
Lead-acid battery	35–40	80–90	First reported rechargeable battery, 1859 [10].
Nickel–cadmium battery	40–60	50–150	First reported nickel-based rechargeable battery, 1899 [11].
Nickel-metal hydride battery	60–120	140–300	Improved version of Nickel–cadmium battery with lower toxicity, 1987 [12].
Lithium-ion battery	100–265	250–693	First reported commercial lithium-based rechargeable batteries with high specific energy, 1991 [13].
Lithium–sulfur battery	350–500	2,199 (Theoretical)	Sulfur-based cathode, 2009 [14].
Lithium–oxygen battery	500–900	11,680 (Theoretical)	Praised as the “holy grail” of rechargeable lithium-based batteries, 2009 [15].

From the perspective of energy storage, two key parameters to evaluate the efficacy of a battery are specific energies (e) and energy densities (u). Specific energy, also refers as the gravimetric energy density, is defined as the amount of energy (U) stored in a system per unit mass (m_u):

$$e = \frac{U}{m_u} \tag{1.1}$$

, where *e* is usually used to determine the weight of the battery required to achieve a given electric range. Energy density, also refers as the volumetric energy density, is defined as the amount of energy (*U*) stored in a system per unit volume (*V*):

$$u = \frac{U}{V} \tag{1.2}$$

, where *u* is usually used to determine the size of the battery required to achieve a given electric range.

Comparing with the non-LBBs such as lead-acid, nickel–cadmium, and nickel-metal hydride batteries, LBBs demonstrate higher specific energies with greater energy densities. In other words, LBBs can provide the same amount of energy with lighter and smaller cells.

It is easy to find the rising trend of *e* and *u* in Table 1.1. Nonetheless, for research purposes in LBBs or other types of rechargeable batteries, we may be more concerned about measuring specific capacity (C_s). The relationship between C_s and the total hours (*t*) available when a battery is discharged from 100% state-of-charge to the cut-off voltage, the voltage that generally defines the empty state of the battery, at a certain discharge current (I_d) per unit of active material is shown in Eq. (1.3):

$$C_s = \frac{I_d \times t}{m_u} \tag{1.3}$$

It is critical to distinguish between the definition of *e* and *u* mentioned in Eq. (1.1)/(1.2) and C_s measured during the experiment section. The former (*e* and *u*) describe the characteristics of the battery chemistry and packaging. In contrast, the latter (C_s) describes the maximum amount of energy that could be extracted from a practical battery under specified conditions.

Recently, nanotechnology, the applications of adopting nanomaterials with a single unit sized lower than 100 nanometers (nm) in at least one dimension [16], has had a revolutionary role in synthesizing new electrode materials as the unique properties of nanostructures bring breakthroughs for LBBs [9]. For example, nanomaterials made $LiCoO_2$ cathode for LIB reveal different physical and electrochemical behaviors with improved results compared with its corresponding counter bulk material [17]. Therefore, it is essential to apply nanomaterials to manipulate the properties of electrodes, hence coping with the challenges faced in different types of batteries and improving the electrochemical performances of LBBs.

Among the manipulating techniques for nanomaterials, core@shell-structured nanomaterials, biphasic materials which have an inner core and an outer shell made of different components, have been widely adopted for LBB materials as they can demonstrate special characteristics arising from the variation of core and shell material combination, synthesis design, and geometry [18], [19]. Advantages of applying this structure as electrode materials include enhancing surface area, increasing electroconductivity, and offer advanced lithium storage mechanisms [20]–[22].

1.1.2 Development

LIBs, state-of-the-art LBBs, have gained plenty of interests since their commercialization in the 1990s because of the comparatively high energy density and long cyclic performance among other battery systems at that moment [23], [24]. The comparisons of specific energy (*e*) and specific power (*e/t*) between LIB and other battery systems are shown in Fig. 1.1.

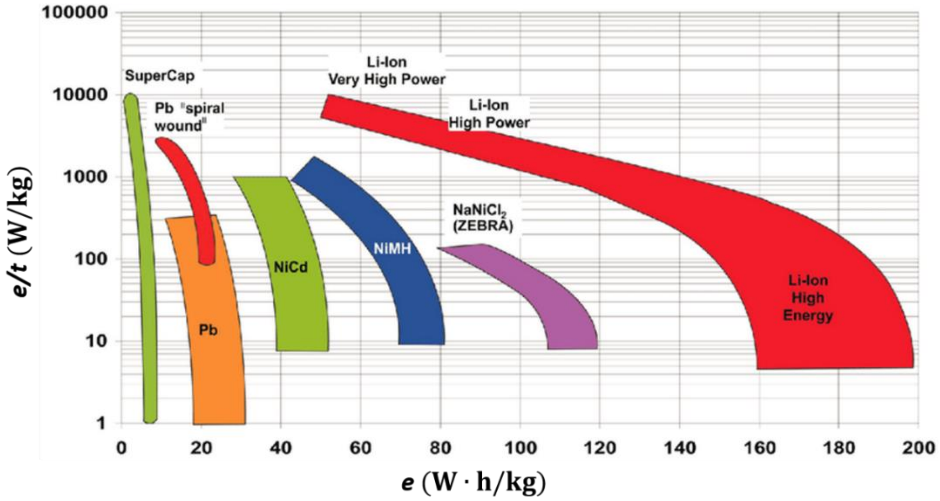

Fig. 1.1. Comparison of specific energy and specific power between different battery types. Modified based on [25].

The combined benefits of high energy density, long cyclic performance, along with quick discharge capabilities, the most important parameters for electronic devices, have contributed LIB to become ideal for portable electronics applications such as laptops, digital cameras, and smart phones. In addition, the accelerating development of information and electronic technology tours the electronic gadgets towards miniaturization [26]. Scientists recently have successfully developed micro-sized rechargeable LIBs [27], [28]. Micro-LIBs are suitable devices for self-powered microelectronics such as sensors, miniature transmitters, and actuators in energy storages [29]. They are also ideal for medical and biological devices such as in vivo imaging, hearing aids, and pacemakers [30]. The application summary of LIB is briefly shown in Fig 1.2. People expect LIB to continue expanding its applications in a wide range of aspects in the foreseeable future [31].

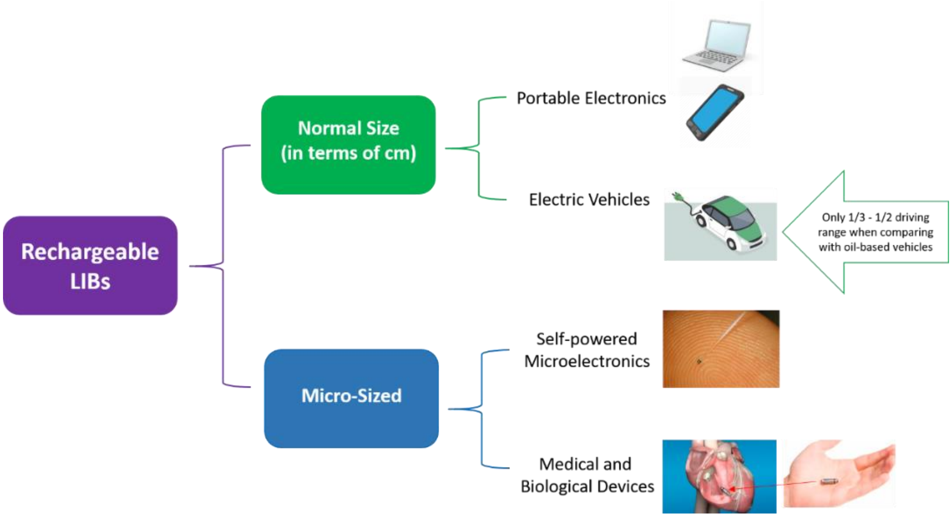

Fig. 1.2. The application summary of LIBs.

Although we gain significant progress on portable electronics advancements using LIBs, implementing LBBs in high power systems such as pure electric vehicles (PEVs) on a large scale is still challenging [32]. Recently, LIB-powered PEVs are commercialized by different companies such as Nissan and Tesla. The Nissan Leaf, launched in 2010, is the best-selling PEV with total sales of more than 130,000 units [33]. It has employed a LIB pack with e =140 W·h/kg to achieve a driving range of 160 km on one charge [34]. Even though the research on LIBs and their electrode materials are still ongoing, the practical limit in specific energy with $e \approx 190$ W·h/kg implies the technical saturation of the driving range of LIB-powered PEVs at around 224 km on one charge. This driving range is only ~35-45% of the compact to middle-sized oilbased vehicles (OBVs) of 480–640 km on one refuel [34]. Therefore, further advancements in LBB devices and systems are essential.

For overcoming the practical *e* limit of LIBs, new mechanisms of energy storage are introduced to utilize similar concepts with LIBs to enhance its *e* reaching to that of gasoline [35]. This concept based on a lithium-ion conversion reaction with oxygen gas gives rise to a new type of lithium-based devices named LOBs [36]. Ultrahigh theoretical *e* of ~3,500 W·h/kg and practical *e* of 500–900 W·h/kg for LOBs can be achieved considering a complete conversion reaction if we consider the masses of current collectors, gas diffusion channels, packaging [37]. This practical *e* is 3–5 times larger than the commercial LIBs. Thus, it potentially allows PEVs to drive more than 560 km on one charge and directly compete with OBVs. Fig. 1.3 compares the *e* and *u* between different battery systems. The direct use of Li metal, the lightest solid element, as the anode; and unlimited oxygen gas, the fourth lightest gaseous element, from the air in the cathode to form a solid-gas system brings the strong advantages for high *e* and *u* so as to fabricate smaller and lighter LOBs for the use of PEVs after the challenges of LOB are solved.

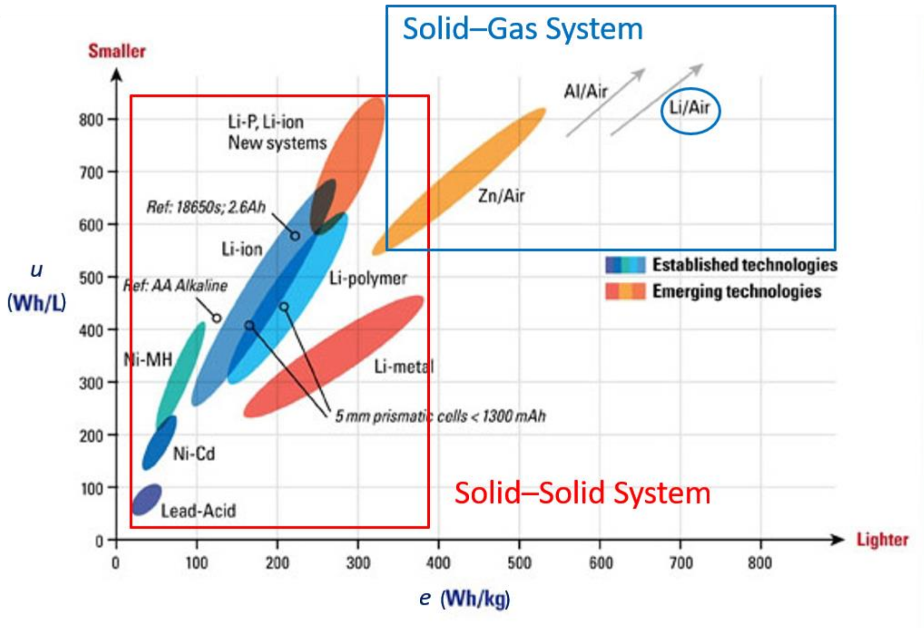

Fig. 1.3. Comparison of specific energy and specific power between different battery types. Modified based on [38].

1.2 Rechargeable Lithium-Ion Batteries

1.2.1 Structure

The success in commercializing the graphite–$LiCoO_2$ LIBs in 1991 resulted in numerous research activities on developing different types of LIBs with various features and performances in terms of energy density, cell voltage, current capacity, cycle life [34], [39]. Fig. 1.4 shows the shape and components of different configurations of LIBs, including cylindrical, coin, and prismatic shape. They all include cathode, anode, separator, and liquid electrolyte even with various shape.

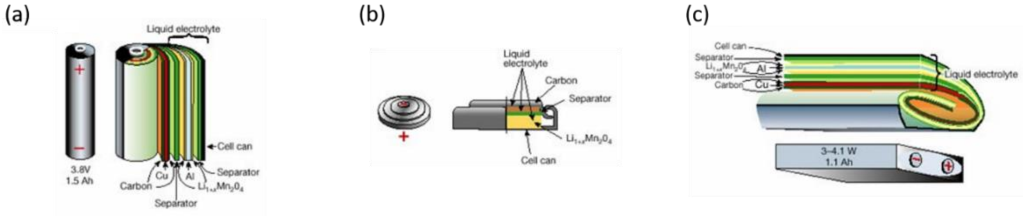

Fig. 1.4. Schematics illustrating (a) cylindrical; (b) coin; and (c) prismatic shape of LIBs. Modified based on [40].

Briefly, a LIB consists of a positive electrode (cathode during discharge), a negative electrode (anode during discharge), and a separator that soaked with electrolyte to ensure there is the transfer of charges within the LIB. The separator acts as an electrical insulator, which avoids short circuit happened between anode and cathode. At the same time, the separator allows ionic charge carriers to transport rapidly for the aim of circuit completion during the current passage within the LIB cell. The cathode and anode materials are coated on current collectors, while aluminum is used for the positive electrode and copper is used for the negative electrode.

As the key components of LIBs, new anode and cathode materials with specific microstructural and electrochemical properties were the main research focus [39], [41], [42]. For the anode, promising candidates of materials include $Li_4Ti_5O_{12}$, transition metal oxides such as CuO, NiO, and Co_3O_4, and Li alloyable Si and Sn. For the cathode, material candidates involve layered $LiMO_2$ (M= Mn, Ni), spinel $LiMn_2O_4$, and olivine $LiMPO_4$ (M= Mn, Fe, Ni, Co). Commercial LIBs mainly employ $Li_4Ti_5O_{12}$ or graphite as the anode and $LiMn_2O_4$, $LiFePO_4$ or $LiCoO_2$ as the cathode [43].

1.2.2 Operating Principles

The operating principles during charge and discharge in a LIB are shown in Fig. 1.5 [43]:

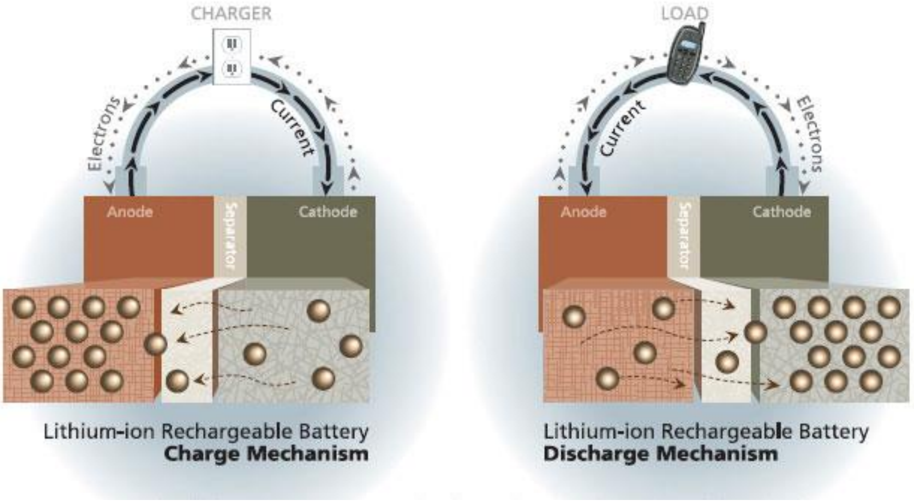

Fig. 1.5. Schematic of the operating principle of Li-ion cell during charge and discharge [43]

During charging, lithium ions will flow from the positive electrode to the negative electrode through the electrolyte. Electrons also flow from the positive electrode to the negative electrode but take a longer path around the outer circuit. The electrons and ions combine at the negative electrode and deposit lithium at the same electrode. When no more ions flow, the battery is fully charged and ready to use. During discharging, the ions flow back through the electrolyte from the negative electrode to the positive electrode. Electrons flow from the negative electrode to the positive electrode through the outer circuit to power the device. When the ions and electrons combine at the positive electrode, lithium is deposited at the same electrode. When all the ions have moved back, the battery is fully discharged and needs charging up again [44].

Taking the typical graphite–$LiCoO_2$ LIB as an example, the chemical equations of the cathode and anode during discharge are presented in Eq. (1.4)–(1.6). For the lithium graphite anode, lithium is oxidized from Li to Li^+ by the following reaction:

$$C_nLi_x \rightarrow C_n + xLi^+ + xe^- \tag{1.4}$$

This reaction oxidized lithium from a 0 to a +1 oxidation state. The lithium ions are then passing through the electrolyte medium towards the cathode, where these ions are incorporated into the material of lithium cobalt oxide by the following reaction:

$$Li_{1-x}CoO_2 + xLi^+ + xe^- \rightarrow LiCoO_2 \tag{1.5}$$

This reaction reduces cobalt from a +4 to a +3 oxidation state. Overall, the LIB processes the following reaction during discharge:

$$C_nLi_x + Li_{1-x}CoO_2 \rightarrow LiCoO_2 + C_n \tag{1.6}$$

For a reversible LIB, the reactions mentioned above can be run in reverse order so as to recharge the cell. In this situation, the lithium ions leave the lithium cobalt oxide and pass back to the anode, where they are reduced back to non-ionized lithium and then reincorporated into the graphite network.

1.2.3 Literature Reviews

LIBs were invented by Asahi Kasei in 1985 [45] and commercialized by Sony in 1991 [46]. The earliest LIBs used graphite as the anode material and layered $LiCoO_2$ as the cathode, separated by a nonaqueous Li-ion-conducting organic electrolyte with LiPF6 salt dissolved in EC-DMC solvent [47]. The graphite used in anode, a carbonaceous material, was a layered intercalation compound, one of the most widely used materials as lithium anodes. Lithium can be readily inserted and extracted into the structure. The lithiated compounds have stable phases up to the LiC_6 stoichiometry, delivering a theoretical specific capacity of 372 mAh/g [47].

In 1994, Aurbach et al. discovered that a stable, passivating solid-electrolyte interphase (SEI) was formed at the carbon particle surfaces after discharge in the LIBs. Thus, it prevents graphite exfoliation and inter alia solvent co-intercalation [48]. The SEI has both positive and negative impacts on LIBs. For the advantage, the newly formed interphase avoided further decomposition of electrolyte and also solvent molecules co-intercalation. Therefore, this enhanced the rechargeability of LIBs. However, the SEI formation is mainly related to the decrease of the initial irreversible capacity. Moreover, it was found that the SEI subsequently passivated the anode and increased the undesired electrochemical resistance [49].

After six years since the commercialization of LIBs, a new type of anode material, tin-based oxide materials, were firstly introduced in 1997 as a promising anode material by the Fuji amorphous tin-based composite oxide with the reversible capacity of 650 mAh/g with a coulombic efficiency near 100% after initial charge [50]. For the reaction process of tin oxide materials, the tin oxide was first reduced to metallic tin, which may be partially irreversible. Then, the next process is the reaction of tin alloying/de-alloying with lithium. In most cases, this process is very reversible.

In 2005, Sony's Nexelion battery adopted amorphous Sn–Co–C material as the electrocatalytic anode. This material has provided positive electrocatalytic influences on tin-based (also called stannide) intermetallic alloys for LIBs as the first breakthrough. It also significantly navigated the research direction in terms of exploring tin-based intermetallic alloys for commercial use as electrocatalytic anodes for LIBs [51]. There are serval key advantages of adopting this stannide material. First, this material could minimize the particle shape change during discharge and charge, solving the cycling characteristics problem. Next, the enhanced lithium-ion density unit per volume ratio compared with the traditional graphite anode resulted in a dramatic enhancement in the density. Finally, the amorphous tin-based anode has a better affinity for lithium ions. Hence, the charging efficiency has increased [52].

Since then, many tin-based intermetallic materials have been developed as anode materials for LIBs, including SnCo, $CoSn_3$, and $FeSn_2$ [53], [54]. $FeSn_2$ nanospheres show a high capacity of around 500 mAh/g with the cyclic performance of more than 15 cycles among the stannide materials. The high electrochemical performance of the $FeSn_2$ anode may be attributed to its crystal structure. The open channels located inside the crystal lattice of $FeSn_2$ facilitate the alloying and penetration of lithium-ion within the tin host [53]. In 2013, $FeSn_2$ that prepared by poly vinyl pyrrolidone surfactant-assisted solvothermal method, could discharge to an excellent capacity of 1268 mAh/g, but its cyclability rapidly decreased after the 20th cycle [54]. Besides, the nanoparticles morphology and size control both require complicated steps and huge quantities of waste solvent recycling.

On the other hand, researchers discovered the beneficial effect of carbon addition as coating or matrix in LIB anode materials. For the tin oxide anode materials, attempts of carbon coating were made for carbon acting as conductor or structural buffer since 2008 [55]. Moreover, carbon additives or coating can provide good electric conductivity. Furthermore, the addition of carbon provides buffers against particle volume expansion during lithiation. Therefore, this limited the pulverization of the particles and enhanced mechanical stress tolerances of the composite, leading to greater capacity and better cyclic performances [56], [57].

Fig. 1.6 summarized the development history of some important LIB anode materials:

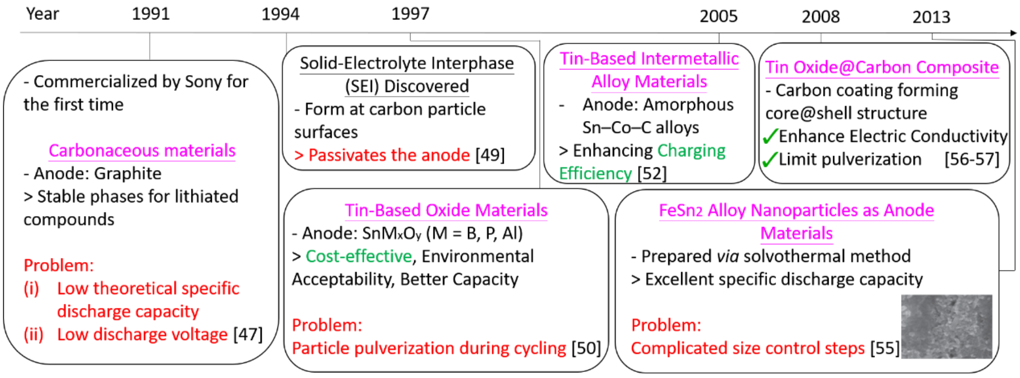

Fig. 1.6. A brief timeline summary of LIB anode materials development.

1.2.4 Challenges and Possible Solutions

Although graphite is one of the most widely adopted materials for LIB anodes, it suffers from serval major drawbacks. Graphite yields a low theoretical specific discharge capacity (372 mAh/g), low discharge voltage (<0.2 V), sluggish reaction kinetics, and ease of formation of dendritic side products because the lithium ions stored in the 2D carbon planes can only form a maximum stoichiometry of LiC_6 [51]. Therefore, adopting tin has shown the ability to form a reversible and electrochemical alloying reaction with Li up to $Li_{4.4}Sn$, thus providing higher lithium storage capacity and consequently higher theoretical specific discharge capacity of 993 mAh/g. The comparisons between stannide-based materials and traditional carbonaceous materials are shown in Table 1.2 :

Table 1.2. Comparisons between stannide-based materials and traditional carbonaceous materials as anode for LIB.

Anode Materials	Stannide-based Materials	Traditional Carbonaceous Materials
Theoretical Discharge Capacity	993 mAh/g	372 mAh/g
Discharge Voltage	High (>0.5V)	Low (<0.2V)
Reaction Reversibility	High	Low
Electrical Conductivity	High	High
Dendritic Side Products	Comparatively less	Dominant

After few decades, stannide-based oxides and stannide-based intermetallic materials have been widely adopted as LIB anodes. Among them, $FeSn_2$ has shown favorable electrocatalytic properties. However, the specific discharge capacity and cyclability of $FeSn_2$ can still be further improved. From previous papers, we can identify three major drawbacks. First, the electrical conductivity of the stannide-alloys is not comparable to the state-of-the-art LIB anode materials [58], [59]. Second, the inner-stress-induced is increased because $FeSn_2$ nanoparticle suffers from a big change of volume during the lithiation/delithiation process. The extra stress causes the active electrocatalyst to pulverize. Thus, this would induce loss of electrical connection with the current collectors [49], [58]. Though stannide alloy anodes with Fe as electrocatalytic inactive acting as a buffering agent are capable of improving the cyclability of the LIBs by redistributing the volume change-induced fragmentation, yet the minimization of pulverization of the nanoparticles is still a major concern that needs to be addressed [60]. Third, the new surfaces formed by the pulverized active electrocatalyst consume a higher amount of Li, forming SEI that subsequently passivates the anode and increases the undesired electrochemical resistance [49].

In order to address the challenges of $FeSn_2$ mentioned above, it is necessary to design an improved electrocatalytic LIB anode and synthesize precisely controlled crystalline $FeSn_2$ with sub-50 nm size. Previous results suggested that the lack of intrinsic and extrinsic defects in highly crystalline $FeSn_2$ alloy nanoparticles prevents the irreversible trapping of Li^+ ions, resulting in better cyclability and lower initial discharge capacity than their bulk counterparts [60]. In addition, the sub-50 nm size crystalline $FeSn_2$ would also possibly alleviate the absolute strain at the nanoscale and reduce the charge-diffusion pathways. On the other hand, the conductivity of these stannide alloy anodes can be improved by compositing them with carbon based on the experience of tin oxide@carbon composite. Adopting core@shell-structured nanomaterials (CSNs) has also been proven beneficial in accommodating strains during the lithiation-induced volume change and minimizing core $FeSn_2$ nanoparticles pulverization [59].

1.3 Rechargeable Lithium–Oxygen Batteries

1.3.1 Structure

Similar to LIBs, a typical non-aqueous LOB consists of an anode, a cathode, and a separator with electrolyte, as shown in Fig. 1.7. The anodes in most of the reported LOBs are directly made of lithium metal, as it is expected to achieve the highest energy and capacity. For the cathode, which is also named air electrode, the material choices are more diversified and wide-ranged. As the reaction of the LOBs mostly takes place in the cathode, the major technology challenges come from the cathode design. Therefore, the structure of air cathodes in different types of lithium-air batteries need to be designed and optimized accordingly. Nevertheless, the goals of using those specific designs are to reach high capacity, a long cycling life, and high round-trip efficiency [61]. Moreover, a great amount of cathode designs introduces catalysts to improve the transport kinetics of LOBs so as to facilitate the electrochemical reaction during the charge/discharge process. Last but not least, the coin cells cases used in LOBs consists of lots of small holes in the bottom case for the air to pass through the case for the reaction when comparing with the entirely enclosed LIB coin cell cases.

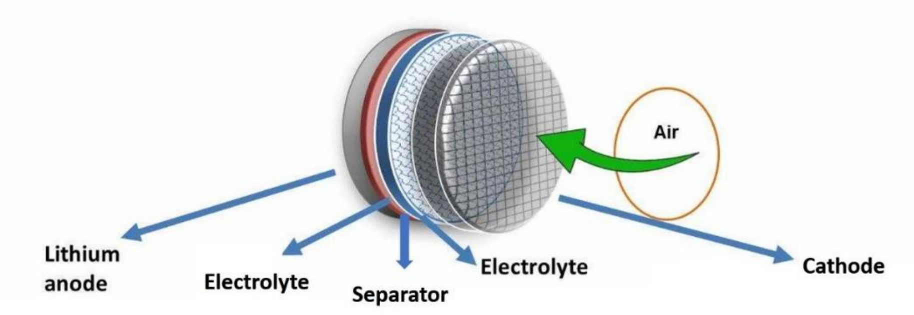

Fig. 1.7. A schematic illustrating the basic structure of a LOB coin cell. Modified based on [62].

In terms of electrolyte, four types of LOBs have been proposed and developed, as shown in Fig. 1.8. They are non-aqueous, aqueous, hybrid non-aqueous/aqueous, and solid-state LOBs [15]. For non-aqueous LOBs, the electrolyte composed of a lithium salt dissolved in a non-aqueous solvent, such as LiTFSI dissolved in a TEGDME solution [63]. For aqueous LOBs, an aqueous electrolyte is used instead. For lithium anode protection against the water as the solvent, a solid-state lithium-ion conducting membrane is placed on the anode [64], as shown in Fig. 1.8 (b). Soon after aqueous LOBs, a hybrid non-aqueous/aqueous system has then been proposed [65], with a non-aqueous electrolyte filled in between, with the aim of avoiding direct contact between the solid electrolyte membrane and lithium, so as to increase the conductivity of lithium-ion. In order to address the possibility of leakage and safety issues for the liquid electrolyte mentioned above, solid-state LOBs are developed without using any liquid electrolytes, such as adopting single-crystalline, glass-ceramics, and silicon polymers, as shown in Fig. 1.8 (d) [66].

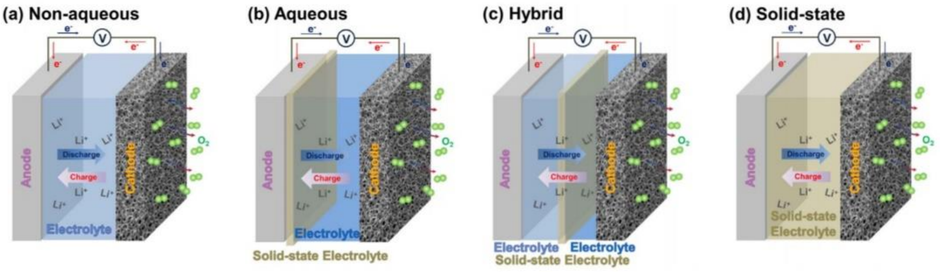

Fig. 1.8. Schematic configurations of (a) non-aqueous, (b) aqueous, (c) hybrid, and (d) solid-state LOBs. Modified based on [61].

1.3.2 Operating Principles

For a typical non-aqueous LOB, the operating principles during charge and discharge in a LOB are shown in Fig. 1.9 [67]. During discharge and charge, the anode with lithium undergoes stripping and plating reactions. During discharge, the metal anode is oxidized, releasing Li^+ ions into the electrolyte solution. During charge, the process is reversed, and the Li^+ ions are reduced and re-plating on the lithium anode. At the cathode, oxygen from the atmosphere enters the porous electrode and dissolves into the electrolyte. During discharge, the dissolved oxygen is reduced at the electrode surface and reacts with Li^+ ions forming lithium-based oxides on the air electrode surface. This process is also called oxygen reduction reaction (ORR). During charge, the lithium-based oxides are reduced, and the gases are regenerated, releasing them into the atmosphere, which is also called oxygen evolution reaction (OER).

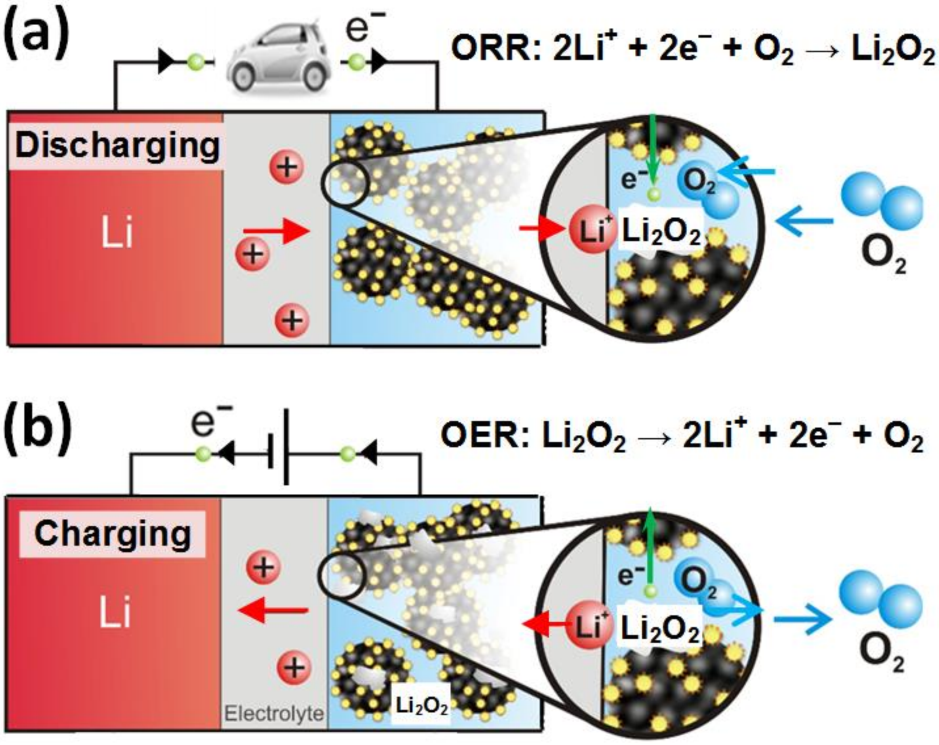

Fig. 1.9. Schematic of the operating principle of LOBs during (a) discharge, and (b) charge [67].

The typical chemical reaction routes in electrolytes were proposed by Abraham [68]. This reaction involves the reduction of oxygen to lithium superoxide (LiO_2) through a single electron transfer and followed by a disproportionation reaction, as shown in Eq. (1.7)–(1.8):

$$Li^{+} + O_2 + e^{-} \rightarrow LiO_2 \tag{1.7}$$

$$2LiO_2 \rightarrow Li_2O_2 + O_2 \tag{1.8}$$

Another possible route of electrochemical process from lithium superoxide by one-electron-transfer is shown in Eq. (1.9):

$$LiO_2 + Li^{+} + e^{-} \rightarrow Li_2O_2 \tag{1.9}$$

No matter which route is chosen for further oxidation of lithium superoxide, the major discharge product of the reactions is lithium peroxide (Li_2O_2). This discharge product is insoluble in the non-aqueous electrolyte. It covers the surface of the porous cathode and fills up the void spaces, which could passivate further reactions. To ensure the LOB is rechargeable after discharge, Li_2O_2 decomposition back to lithium and oxygen is necessary by OER, as shown in Eq. (1.10):

$$Li_2O_2 \rightarrow 2Li^{+} + O_2 + 2e^{-} \tag{1.10}$$

As the anode is simply Li, the key enabler for practical LOBs is to obtain an energetically stable cathode and cathode material for enhancing and stabilizing ORR–OER against Li_2O_2 passivation.

1.3.3 Literature Reviews

The 1^{st} LOB was prototyped in 1996 at EIC Laboratories by combining a porous carbon cathode and a lithium anode with a nonaqueous electrolyte possessing Li-ion-conducting gel polymers such as EC, PC, $LiPF_6$, and PAN [69]. However, this discovery could not gain much attention beyond the community because the LIBs applications and developments had a rapid rise between 1990 and 2010 [15], [70]. After a decade, the urgent demands of high-energy-density rechargeable batteries for improving the driving range of PEVs have led LOBs to recapture worldwide attention as the “holy grail” since 2009 [15]. In the first few years, porous carbon nanomaterials, such as porous carbon powders, mesoporous carbon, carbon nanotubes, and carbon nanofibers, were evaluated as the first type of potential cathode materials for LOBs because they are technically known and commercially available with large surface areas for accommodating O_2 and enhancing ORR–OER in addition to high electronic conductivities for improving lithium-ion and electron transports [71], [72]. Although comparatively high specific capacities between 600 mAh/g and 1,500 mAh/g were often observed, these values were only valid for the first few discharge–charge cycles, and they faded out quickly after that.

Later studies in 2011 revealed the precipitation of reversible LiO_2 on cathode surfaces, and the subsequent reduction of some LiO_2 into dense, pore-free, and insulating Li_2O_2, during ORR on discharge [73], [74]. The corresponding chemical equations were mentioned in Section 1.2.2. At some time, scientists majorly believed that a higher pore volume could always deliver a better capacity with the same material as there are more spaces for the reaction to occur. However, in later years, scientist discovered that both too small or too large pore size would not benefit the oxygen reduction process because the former will be easily blocked by Li_2O_2 deposition on the pore entrance, which preventing further oxygen diffusion while the latter is usually flooded by the electrolyte forming two-phase instead of three-phase regions [74]. Hence, if the cathode's porous structure does not have a sufficiently large pore size and number, which refers to the active surface area, the accumulation of Li_2O_2 on the cathode surface during ORR can easily fill up the pores and electrically passivate or clog the cathode, giving rise to poor ORR–OER and cycle life in LOBs.

In order to amend the serious problems of Li_2O_2 passivation in "porous cathodes" mentioned above, catalysts were either mixed with porous carbon nanomaterials or prepared as porous nanostructures to form electrocatalytic cathodes more recently [75]. The introduction of electrocatalysis by electrocatalytic cathodes could make Li_2O_2 looser and porous, thereby allowing O_2 and Li ions to diffuse into the Li_2O_2-occupied pores, lowering the reaction over-potentials and making ORR–OER more stable [76]. Noble metals and transition metal oxides (TMOs) are the two main groups of cathode catalysts explored so far. On the side of catalyst-mixed porous carbon nanomaterials, noble metal catalysts, such as Au, Pt, Pd, and Ru, exhibit very good electrocatalytic stability [77], [78]. For example, the nanoporous Au cathode delivered a specific capacity of ~300 mAh/g over 100 cycles with 95% retention at 2.6 V voltage [79]. Au-

Pt core-shell nanoparticle (NPs) chains also showed a great catalytic activity with a specific capacity of ~1000 mAh/g over above 20 cycles at 2.6 V [80]. However, those catalysts are very expensive, which is not practical for industrial applications.

On the other hand, TMO catalysts, such as MnO_2, Co_3O_4, Cr_2O_3, and RuO_2, are also beneficial from good electrocatalytic stability. Moreover, they are easy to synthesis with a wide range of material types. The costs of them are also low. Binary and ternary TMO catalysts have drawn much attention and been investigated. The reduced graphene oxide/α-MnO_2 composite exhibited a specific capacity of 558.4 mAh/g at a current density of 100 mA/g [81]. Carbon-sphere/Co_3O_4 delivered a specific capacity of ~1000 mAh/g for about 20 cycles [82]. $CoMn_2O_4$ with oxygen deficiency delivered an initial capacity of ~5860 mAh/g upon 40 cycles with almost 100% coulombic efficiency [83]. Multiporous $CoMn_2O_4$ microspheres exhibited a specific capacity of 4861 mAh/g with capacity reversibility over 50 cycles [84].

Among TMOs, manganese oxides (MnO, Mn_3O_4, Mn_2O_3, MnO_2) with abundant electrocatalytic sites have demonstrated high specific capacity as catalysts in LOB cathodes [85]–[87]. A study on more than 60 types of MnO_2 with different crystalline phases and related composites for LOB applications showed that the MnO_2 composites with noble metals or carbon nanotubes are highly stable over more than 100 cycles at the upper limit capacity of 500 mAh/g [88]. Unlike MnO_2-based catalysts, limited attempts have been made to investigate the application of Mn_3O_4 catalysts for LOB. Mn_3O_4 NPs/carbon nanofibers composite was applied as an electrocatalyst, which improved the cycling performance of LOBs of more than 50 cycles [89]. High surface area Mn_3O_4 hollow nanocages, 90.65 m^2/g, were fabricated *via* a heat treatment process using carbon spheres as a sacrificial template. The hollow Mn_3O_4 nanocages were applied as an oxygen electrode exhibiting a high initial capacity of 3380 mAh/g and cyclic stability over 50 cycles [90]. Oxygen vacancies produced in heat-treated Mn_3O_4 hollow nanocages facilitated $Li^+/O_2/e^-$ transportations [91]. Moreover, the inter-particle pores resulted in a shorter diffusion pathway and improved catalytic activity [85].

Fig. 1.10 summarized the development history of some important LOB cathode materials:

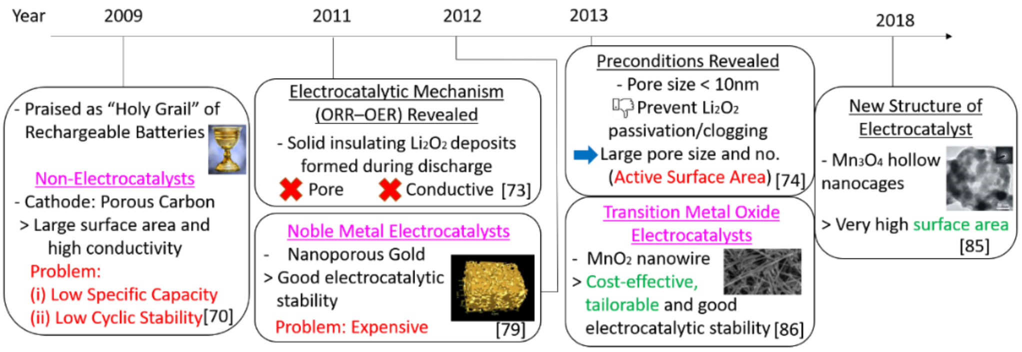

Fig. 1.10. A brief timeline summary of LOB cathode materials development.

1.3.4 Challenges and Possible Solutions

As detailly explained in Section 1.3.3, the major challenge of LOBs comes from the cathode change in pore structure and surface area because of solid discharge product Li_2O_2 formation, causing the electrical passivation of cathode and hence low cyclic life. Adding TMOs as the catalyst for the cathode is one of the possible solutions. State-of-the-art TMO hollow Mn_3O_4 nanocages synthesized by sacrificial templates show excellent characteristics for enhancing the LOB catalytic activities. However, in terms of material properties, one major drawback of using Mn_3O_4 nanocages as electrocatalysts is their low electronic conductivity, restricting ORR–OER kinetics [92]. Moreover, detachment and pulverization of nanostructured catalysts may occur during cyclic [93], resulting in electrode material loss. On the other hand, in terms of synthesizing procedures, the preparation time of sacrificial carbon templates is long and requires extra washing of materials, leading to a high percentage of material loss. Therefore, it is desirable to have an electronically conductive catalyst for oxygen cathode with chemical and physical stability during electrochemical performance synthesized by high yield simplified procedures [61], [94]. To achieve the desirable catalyst properties by material engineering, CSNs can be developed to generate thin carbon shells onto the surface of the current state-of-the-art materials as cathode materials for LOBs for greater capacity and better cyclic performances, similar to LIB anode materials.

1.4 Aim and Objectives

The current study aims to develop promising novel catalytic materials named core@shell-structured nanomaterials (CSNs). These CSNs are then developed as electrode materials for enabling rechargeable lithium-based batteries (LBBs), including lithium-ion batteries (LIBs) and lithium–oxygen batteries (LOBs), to achieve outstanding electrochemical performances. Following objectives are included:

(1) To design, synthesize, and physiochemically evaluate various interesting CSNs.

(2) To prepare and implement CSNs as catalytic electrodes and corresponding lithium-based battery cells for operando, in-situ, and ex-situ studies of their electrocatalytic activities and stabilities.

(3) To establish an electrochemical discharge–charge voltage–capacity model for analyzing the observations and revealing the underlying reaction mechanisms.

(4) To demonstrate and validate the LBB prototypes with optimized/characteristic electrode/cell designs.

1.5 Thesis Outline

In this thesis, the work of CSNs developed for LBBs will be presented by following sequences:

Chapter 1 introduces LBBs, including the background of LBBs, development milestones for rechargeable batteries, and key parameters concerned, followed by the impact of nanomaterials on LBB. Then, the development and applications of two types of LBBs, LIBs and LOBs, are discussed, indicating some handicaps faced by LIBs and the reasons for the desperate research demand of LOBs. The second and the third part of chapter 1 reviews the structure, operating principles, important development events, challenges faced, and possible solutions for LIBs and LOBs, respectively. Finally, the aim and objectives of this work are stated by applying CSNs for LBBs.

Chapter 2 starts with the introduction of $FeSn_2$@C nanocapsules and their benefits towards the anode of LIBs. Next, synthesis procedures of the new material and the control for comparison are described, and their physicochemical properties are evaluated and compared. After that, the fabrication method of their LIB cells and corresponding electrochemical characterizations are discussed and compared. Finally, the chemical reaction mechanisms inside the LIB are proposed based on the experimental results.

Chapter 3 introduces mixed-phase MnO_2/Mn_2O_3 material and its benefits towards the cathode of LOBs. Next, synthesis procedures of the new material and the control for comparison are described, and their physicochemical properties are evaluated and compared. After that, the fabrication method of their LOB cells and corresponding electrochemical characterizations are discussed and compared. Finally, the chemical reaction mechanisms inside the LOB is proposed based on the experimental results.

Chapter 4 introduces core-shell-structured Mn_3O_4@C material and its benefits towards the cathode of LOBs. Next, synthesis procedures of the new material are described, and its physicochemical properties are evaluated and compared with that of MnO_2/Mn_2O_3 materials in Chapter 3. After that, the fabrication method of their LOB cells and corresponding electrochemical characterizations are discussed and compared. Finally, the chemical reaction mechanisms inside the LOB are proposed based on the experimental results, including the investigation of dead LOB cells.

Chapter 5 introduces the density functional theory (DFT) calculations with surface slab models to further support the experimental results of LOBs in Chapter 3 and 4 on the atomic scale.

Chapter 6 concludes the major finding of the work and discusses the future direction of LBBs.

Chapter 2 $FeSn_2$@C Nanocapsules as Anode for Lithium-Ion Batteries

2.1 Introduction

As reviewed in Chapter 1, among different types of LBBs, LIBs had a more mature and rapid development and applications in the past three decades. Thus, it is easier to kick off the project by investigating and applying the electrocatalysts on LIBs than LOBs. Compared with traditional carbonaceous materials, stannide intermetallic alloys show a much higher potential as effective catalytic materials for the anode in LIBs, especially for $FeSn_2$. However, three major drawbacks are faced as mentioned in Section 1.2.4: (1) pulverization of the active electrocatalyst caused by inducing increasing inner stress from large volume change during the lithiation/delithiation process, (2) SEI formation by the pulverized active electrocatalyst consume a higher amount of lithium passivates the anode and increases the undesired electrochemical resistance, and (3) comparatively low electrical conductivity with other state-of-the-art materials.

To alleviate the disadvantages mentioned above of $FeSn_2$ alloy nanoparticles and design them as improved electrocatalytic LIB anodes, precisely size control of sub-50 nm $FeSn_2$ could result in better cyclability. First, crystalline $FeSn_2$ with a diameter smaller than 50 nm could have a chance to alleviate the absolute strain in nanoscale.

Second, it could also reduce the charge-diffusion pathways. Third, the composition of carbon with stannide alloy anodes can improve the conductivity of the material. Nevertheless, the $FeSn_2$ syntheses as electrocatalytic LIB anodes currently result in poor electrochemical performance because those syntheses are inadequate for efficiently introducing all three features.

Serval synthesis methods for Fe-Sn compounds have been reported previously [54], [95], [96]. Table 2.1 summarizes various synthesis procedures currently adopted to incorporate the three features mentioned above in electrocatalytic stannide-based intermetallic alloys with corresponding specific discharge capacity and cycles.

Table 2.1 Summary of current synthesis procedures adopting size control for improving LIB performances.

Method	Specific Discharge Capacity (mAh/g)	Charge-Discharge Cycles
Mechanically milled $FeSn_2$@C [97]	400	50
Mechanochemical synthesized Sn-Fe/C nanocomposites [98]	380	100
Precursors with thermal treating $FeSn_2$ [54]	1268	20
Arc-discharge synthesized multiphase FeSn/C [99]	818	50
Reduction processed $FeSn_2$ nanocrystals [100]	600	500

Among the procedures in the table, $FeSn_2$ nanocrystals synthesized *via* successive reduction processes delivered an excellent specific discharge capacity of ~600 mAh/g with high stability till 500 charge-discharge cycles. However, during the processes, a great deal of hazardous toluene and chloroform are used, which could have a negative impact on the environment. Moreover, some expensive reagents such as lithium di-isopropylamide [100] are required, which debilitates its commercialization potential. Other than this method which required multiple synthesis procedures, other $FeSn_2$ alloys show poor electrochemical performance in LIBs. The poor performances may be caused by electrochemical instability of LIB during the process of lithiation-delithiation, active sites-controlled morphology, and non-sufficient places for discharge products accommodation.

Moreover, the previous works adopted a conventional carbon matrix for electro-catalytic $FeSn_2$@carbon composite. However, nowadays studies on onion-like carbon shell have shown the advantages comparing with conventional carbon matrix for applications in microwave absorption devices and supercapacitors [101], [102]. Onion-like carbons are nanoparticles with diameters between 5–10 nm. They are in quasi-spherical shape and consist of enclosed defective carbon shells that look like fullerene [103]. Taking advantage of their defective surface, onion-like carbon exhibits excellent structural flexibility, electrical conductivity, and ion desorption/adsorption accessibility on the onion-like carbon surface [104].

In order to tackle the issue of uncontrolled and non-environment friendly synthesis process in previous works, stannide-based intermetallic alloys as LIB electrocatalytic anodes are designed strategically. In this work, an effective one-step in-situ arc-discharge process is used for $FeSn_2$@C nanocapsules synthesis in pure-phase. The materials feature a restricted crystal size smaller than 50 nm with its interesting core@shell-structured Sn-based stannide alloys exhibiting electrochemical properties. The arc-discharge method used is highly controllable. This enables the Fe usage as the buffering metal that can successfully develop $FeSn_2$ intermetallic alloys in sub-50 nm size with features of defective surface contributing by the onion-like carbon shells. In addition, the onion-like carbons and crystalline $FeSn_2$ nanoparticles combination tactfully ameliorates the nanocapsules stability during the electrochemical process and validate a reversible lithiation process during LIB charge/discharge with excellent specific discharge capacity of 835 mAh/g and high stability sustaining a hundred cycles.

2.2 Synthesis

2.2.1 Materials

- Iron powder (99.9% purity, 5 μm average size)
- Tin powder (99.9% purity, 5 μm average size)
- Graphite needle
- Absolute ethanol
- Lithium foils

2.2.2 Synthesis of $FeSn_2$@C Nanocapsules

First, mix the iron and tin powders evenly to form a powder mixture with an iron: tin ratio of 95:5. Next, cylindrical compacts with 20 mm length were formed by subjecting pressure of 20 MPa.

Then, the prepared cylindrical compacts were used in the arc discharge process. In the process, a graphite needle was used as the cathode. A FeSn cylindrical compact was served as an anode in the arc-discharge chamber.

The chamber was further evacuated to maintain a vacuum pressure with 6×10^{-3} Pa. Then, injected 30 mL of ethanol into the chamber as well as hydrogen at 1×10^{4} Pa pressure and pure argon at 2.0×10^{4} Pa pressure. Here, the ethanol acted as the carbon source that would make up the defective onion carbon shell. Ethanol (C_2H_5OH) would be dissociated to O, H and C during the high-temperature process in the arc discharge chamber. The argon under high temperature would produce argon plasma. Hydrogen helped the evaporation of the FeSn power ingot, forming Sn and Fe.

After 10-15 minutes, the ingot was evaporated at ~20 A and ~40 V conditions by arc discharge. During the process, the voltage and current were adjusted automatically via the electrodes distance. For avoiding any explosion caused by the high reactive products, passivated the products for 12 hours with argon. Finally, we collected the product from the top of the chamber.

The proposed formation mechanism of $FeSn_2$@C nanocapsules will be explained in Section 2.3.2.3. The schematic diagram of the arc-discharge process is summarized in Fig. 2.1:

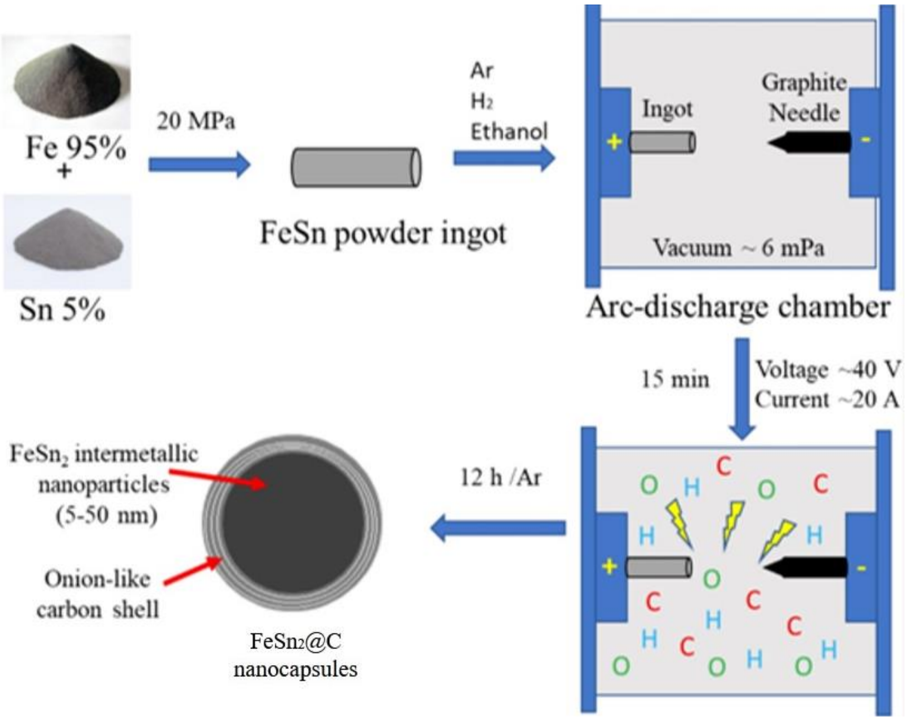

Fig. 2.1. Schematic of $FeSn_2$@C nanocapsules synthesis via the in-situ arc-discharge process.

2.3 Physicochemical Evaluations

2.3.1 Evaluation Methods

2.3.1.1 X-ray Diffraction

X-ray Diffraction (XRD) is a non-destructive testing method for analyzing crystalline material structures. For the preparation before testing, the sample was ground by using a pestle and mortar. The sample was then put onto the sample holder evenly before transferring to the XRD machine.

The phase constituent of the sample of interest was identified using an X-ray diractometer with model Bruker, D8 Advance (XRD, Karlsruhe 76187, Germany). In this test, monochromatized Cu-Kα radiation was used. The operating voltage was 30 kV with a 30 mA operating current. The scan step was set at the value of 0.2 °.

2.3.1.2 Transmission Electron Microscopy

Transmission electron microscopy (TEM) is a technique to examine the surface morphology and structure in nanoscale. To prepare the TEM analysis sample, dissolve the sample using ethanol as solvent and shake the sample evenly by sample shaker. Then, we dropped the solution onto a carbon filmed grid and wait to leave the ethanol to evaporate at room temperature.

The surface morphology and internal structure of the sample of interest were evaluated by using a JEOL 2010 transmission electron microscope (TEM, Tokyo 196-8558, Japan) with 200 kV accelerating voltage.

2.3.2 Result and Discussion

2.3.2.1 Crystal Structure Analysis

In Fig. 2.2 (a), the XRD pattern of the $FeSn_2$@C nanocapsules shows a tetragonal unit cell (JCPDS no. 25-0415) with a C16 type structure of the core $FeSn_2$ nanoparticles that corroborate with the stannide structure [105], [106]. The characteristic peaks exist at 33.7°, 35.1°, 39.1°, 43.8°, 61.1°, and 70.8°. The peaks correspond to (002), (211), (112), (202), (213), and (004) millers indices, respectively [107]. Two types of building blocks form the $FeSn_2$ stannide structure. 6^3 net-like interpenetrating structure is formed due to the homo-atomic interactions in the tin atoms along with $d1$ and $d2$. Additionally, the Fe atoms form chains along the (001) plane because covalent interactions between exist. The heteroatomic Fe–Sn–Fe bonds connect these building blocks. This gives rise to a 3D network eventually, as shown in Fig. 2.2 (b) [100]. The XRD implies a $FeSn_2$@C with high purity was synthesized by the arc-discharge method because we cannot observe any other peaks. No prominent peaks of carbon could be observed because there is only a small amount of carbon present. The previous article shows a chance for carbon shells periodic boundary condition breaking down along the radial direction in translation symmetry. This could make the XRD patterns undetectable [108]. There is a slightly left shift of the characteristic peaks of $FeSn_2$@C nanocapsules when comparing with pure $FeSn_2$ nanoparticles. This shifting could be attributed to atoms doping.

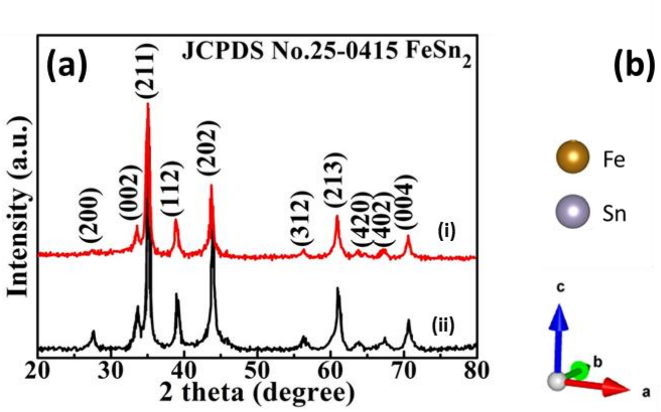

Fig. 2.2. (a) XRD patterns of (i) $FeSn_2$/onion-like carbon ($FeSn_2$@C) nanocapsules and (ii) $FeSn_2$ nanoparticles. (b) Crystal structure of $FeSn_2$.

By using Scherrer's equation, the crystal size is calculated by considering (211) direction as this is the preferred orientation of $FeSn_2$ [100], [106], [107]. The average crystal size of $FeSn_2$ nanoparticles was estimated to be 27.3 nm. Furthermore, the $FeSn_2$ core inside $FeSn_2$@C nanocapsules has a 23.6 nm estimated average crystal size. The broadness of the (211) peak of $FeSn_2$@C nanocapsules could be another evidence for this crystal size reduction. Thus, we could conclude that the suppression of $FeSn_2$ nanoparticles growth to sub-50 nm is contributed by the extra C shells, improving the electrochemical properties.

2.3.2.2 Morphology Analysis

Fig. 2.3 (a) shows the HR-TEM images of $FeSn_2$ nanoparticles are shaped spherically with a 5–120 nm diameter range. The $FeSn_2$ phase formation could be confirmed from the $d = 0.256$ nm characteristic lattice fringe, as shown in Fig. 2.3 (c). This lattice fringe corresponds to the (211) lattice plane.

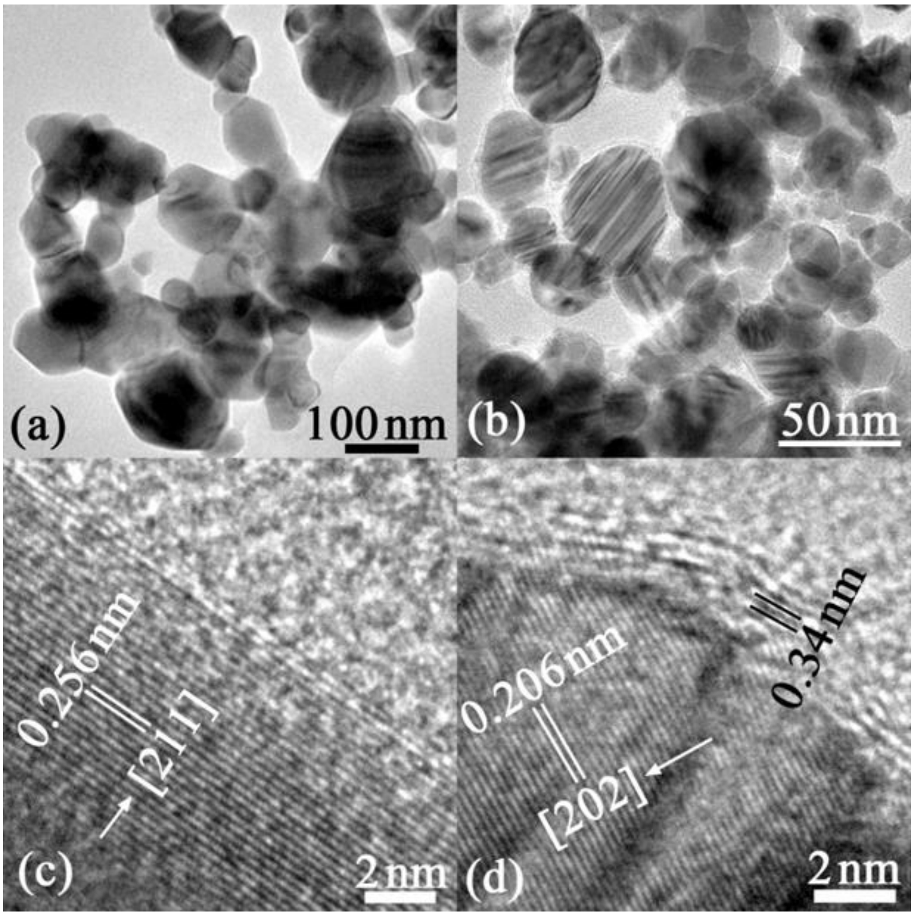

Fig. 2.3. Transmission Electron Microscope (TEM) images of (a) $FeSn_2$ nanoparticles and (b) $FeSn_2$@C nanocapsules. HR-TEM images of (c) $FeSn_2$ nanoparticles and (d) $FeSn_2$@C nanocapsules.

On the other hand, Fig. 2.3 (b) and Fig. 2.4 (a) reveals core@shell-structured $FeSn_2$@C nanocapsules synthesized via in-situ arc-discharge synthesis. Comparing with the TEM image of $FeSn_2$ nanoparticles shown in Fig. 2.3 (a), Fig. 2.4 (a) shows additional layering appearances noticeably between the nanoparticles and background. One of the layering appearances is marked by the red square in Fig. 2.4 (a). These extra layering contrasts reflect the success of carbon coating onto the surface of $FeSn_2$ nanoparticles, forming $FeSn_2$@C nanocapsules. The $FeSn_2$@C nanocapsules maintain their spherical shapes with extra distinct thin shells with around 1 nm thickness outside the nanoparticles. A narrow 5–50 nm ranged size distribution of $FeSn_2$@C is achieved because $FeSn_2$@C nanocapsules crystal growth was suppressed. The onion-like shells show a lattice fringe with $d = 0.34$ nm. This corresponds to the graphitic carbon (002) lattice plane. Moreover, Fig. 2.3 (d) reveals that the $FeSn_2$ core exhibits a $d = 0.206$ nm lattice fringe. This corresponds to the $FeSn_2$ (202) lattice plane. From the image, we could observe the existence of C shells lattice defects, such as the blending of homocentric sphere layers and carbon layer breakage. Additionally, structural defects could also be observed, such as stacking faults, C layers dislocation, and interstitial atoms [109]. For example, one of the plane defects is marked by the red square in Fig. 2.4 (b), where the carbon layer discontinues in the middle of the red square and reappears at the two ends. These disordered C shells consist of lattice defects that could facilitate Li^+ ions interaction through them. Thus, this enhances the electrocatalytic $FeSn_2$@C nanocapsules specific discharge capacity and also rate capability in LIB.

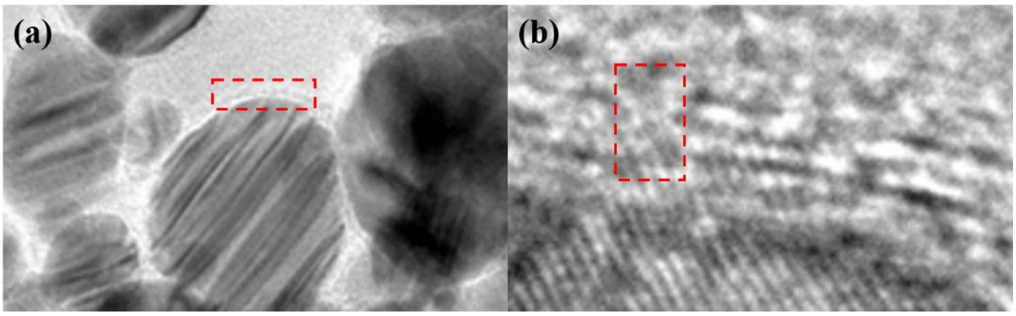

Fig. 2.4. The expanded region of (a) TEM image and (b) HR-TEM image of $FeSn_2$@C nanocapsules in Fig. 2.3 (b) and Fig. 2.3 (d), respectively.

2.3.2.3 Proposed Formation Mechanism

A proposal of a theoretical formation mechanism during the arc-discharge process for $FeSn_2$@C nanocapsules is suggested by adopting the observations of the physicochemical results. The arc-discharge method we proposed outperforms the conventional thermal evaporation method when comparing with the capability of producing atomic hydrogen that is supersaturated. The hydrogen in this arc-discharge method simultaneously provided both heats required and tiny bubbles forming in the Fe-Sn molten alloy. We could approximately consider tiny bubbles as an evaporating source in the vacuum as those bubbles have low inner pressure. These bubbles are assumed in an oversaturated state during the melting and evaporations of surrounding bulk from the bubble boundary. These over-saturated vapors finally escape from the molten Fe-Sn alloy surface, forming intermetallic nanoparticles. The Sn content inside the nanoparticles is greater than Fe, as Sn and Fe have evaporation rates of 47.69 and 1.61 g/cm^{2}h at 1873 K, respectively [96].

Fig. 2.5 demonstrates the nucleation of gas-phase during $FeSn_2$ nanoparticles formation:

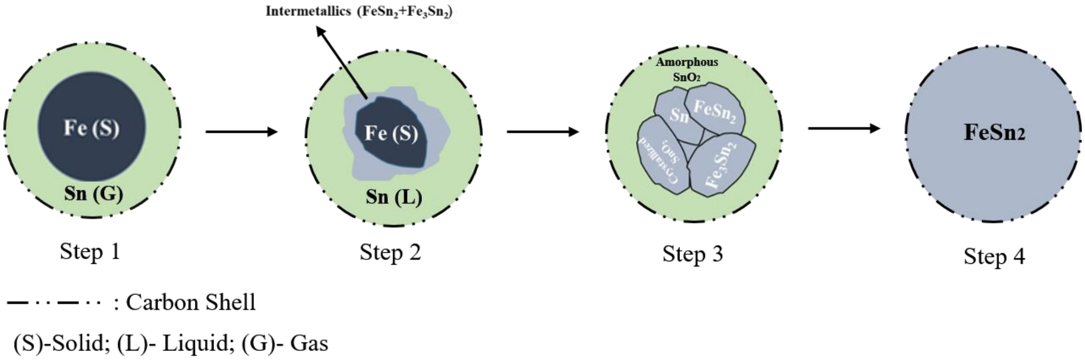

Fig. 2.5. Schematic representation of the formation of $FeSn_2$@C nanocapsules during the in-situ arc-discharge process.

We can be generally classified the formation into four major steps. In the first step, super cooling provides nucleation energy and driving force during the process. Through random collisions, this drives the atoms progress to clusters to nuclei [110]. As hydrogen gas provides an extremely high thermal energy, the Sn (with a boiling point of 2876 K) will evaporate first and form a gas state around the Fe nuclei (with a boiling point of 3153 K) during arc-discharge [96]. In the second step, the core Fe nuclei adsorb Sn clusters on their surfaces. They coagulate nanoparticles progressively. Meanwhile, the intermetallic Fe-Sn compound phases are formed *via* the interdiffusion of boundaries and interface reactions [110]. In the third step, diffusion consumes the Fe in the maternal phase. The excess content of $FeSn_2$ nanoparticles and Sn as the dominant phase is left behind [96]. The trimers of intermetallic $FeSn_2$ stannide formation are favored over Fe_3 and Fe_2Sn because of the excess Sn content composed in FeSn powder ingot [96]. Moreover, the effective heat of formation ($\Delta H'$) shows encouragement for the formation of $FeSn_2$, as that value in $FeSn_2$ phase (-0.087 kJ·(mol·atom)$^{-1}$) is lower than that of FeSn (-0.082 kJ·(mol·atom)$^{-1}$) [99]. Finally in the fourth step, only $FeSn_2$ stannide left, forming the pure $FeSn_2$ core of $FeSn_2$@C nanocapsules.

In the view of ethanol, it vaporizes to form carbon C2-clusters during the high-temperature arc discharge. Those clusters nucleate and form polycyclic aromatic structures. The structures tend to form five-membered rings, which create a curvature so that bonds could be saturated. After plenty of carbon units added into the ring structures, it expands to onion-like cages. The plasma zone is confined by super cooling during the arc-discharge process. The confined zone allows the existing cages to act as centers of nucleation. By forming multiple shells, the onion-like cages grow. These inner layers growth is often incomplete before the next cluster adds to the original. The incomplete onion carbon-shell layers are attributed to the defects in the material as we observed in the HRTEM. The number of defects and size proportion varies with different curvature degrees [111].

2.4 Nanocapsules as Anode and their Lithium-Ion Battery Cells

2.4.1 Materials

- $FeSn_2$@C and $FeSn_2$ prepared in Section 2.2.2
- Carbon black
- Polyvinylidene fluoride (PVDF)
- N-methyl pyrrolidinone (NMP)
- Copper foils
- Polypropylene (PP) film
- Lithium hexafluorophosphate ($LiPF_6$)
- Ethylene carbonate (EC)
- Diethyl carbonate (DEC)

2.4.2 Preparation of $FeSn_2$@C Nanocapsules as Anode

The $FeSn_2$@C nanocapsule based electrocatalytic anodes for LIB were prepared by forming a homogeneous slurry. The slurry consists of 80 wt.% $FeSn_2$@C nanocapsules, 10 wt.% PVDF binder that dissolved in NMP, and 10 wt.% carbon black used as a conducting agent. The slurry was coated onto copper foils. Finally, the coated copper foils were heated at 120 °C under vacuum for 24 h. As a control measurement, pure $FeSn_2$ nanoparticle anodes were also prepared in a similar way for comparison.

2.4.3 Fabrication of Lithium-Ion Battery Cells

We assembled the LIB cells in an argon-filled glovebox to avoid water and oxygen contamination. Briefly, the prepared copper foils coated with slurry as the anode, 1 M $LiPF_6$ in EC/ DEC (1:1 in volume) as the electrolyte, PP film as the separator, and lithium foils as the cathode were assembled into a coin cell 2025 for electrochemical characterizations.

The schematic diagram of the LIB cell construction is demonstrated in Fig. 2.6:

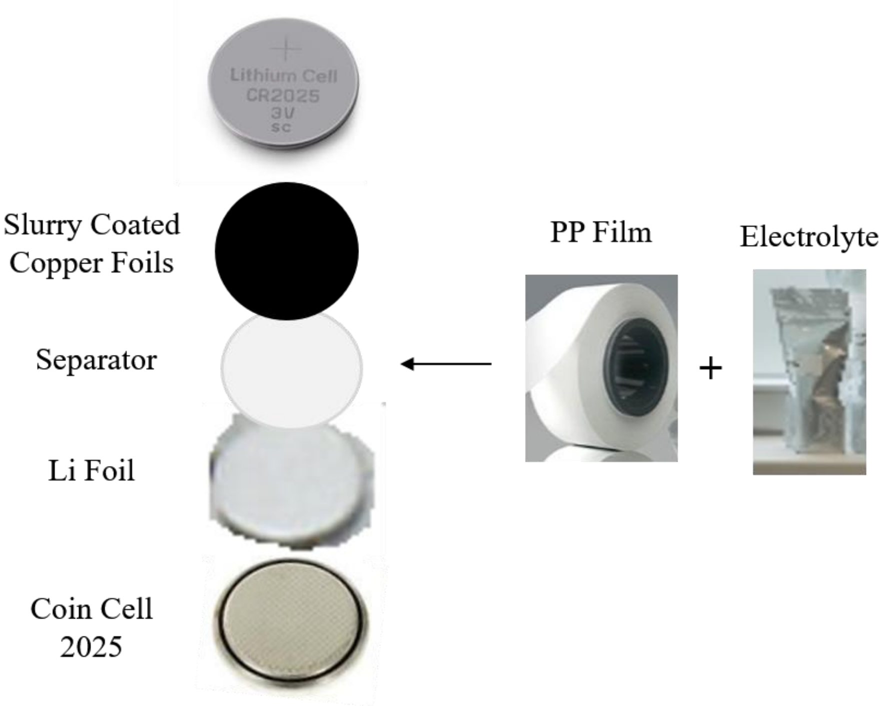

Fig. 2.6. Schematic of LIB cell construction.

2.5 Electrochemical Characterizations

2.5.1 Characterization Methods

2.5.1.1 Galvanostatic Measurements

We carried out the galvanostatic measurements in a battery testing system (Lanhe CT 2001, Wuhan 430014, China) with a specific current density of 50 mA/g and within the voltage range between 0.05 and 2.0 V (vs. Li/Li^+). The rate capabilities of the electrodes were measured by LIB cells cycling in the voltage range between 0.05 and 2.0 V at different specific current densities, first from 50 to 4000 mA/g and then back to 50 mA/g. Five cycles were recorded for each of the tested specific current density.

2.5.1.2 Electrochemical Impedance Spectroscopy

The LIB cells were electrochemically tested using an electrochemical impedance spectroscope (CHI 660E, Shanghai 201500, China), also called EIS. The cyclic voltammetry (CV) and also Nyquist measurements were examined before and after the first cycles. We conducted the CV measurements at a frequency range between 10 mHz and 100 kHz with a 0.1 mV/s voltage sweep rate. The impedance measurements were recorded with a 5-mV perturbation amplitude.

2.5.2 Result and Discussion

Generally, $FeSn_2$@C nanocapsule-based anodes show improvements in both electrocatalytic performance and stability compared with pure $FeSn_2$ nanoparticle anodes. The following three factors could cause this:

(1) The confined cores size with sub-50 nm crystalline $FeSn_2$ nanoparticle in pure phase could provide excellent specific discharge capacity and energy storage when combined with Li^+ ions;

(2) The onion-like carbon shell provides enhanced electric conductivity. It also suppresses the crystal size of $FeSn_2$ and helps for strains accommodations during the volume change induced during lithiation. Furthermore, it protects direct contact the $FeSn_2$ and electrolyte so as to prevent subsequent SEI formation;

(3) Iron successfully acts as buffering agents facilitating the internal stress redistribution evenly during lithiation/delithiation. Thus, it prevents or delays the aggregation and pulverization of tin.

In the sections below, we will verify the three factors proposed above *via* galvanostatic measurements in Section 2.5.2.1–2.5.2.3 and electrochemical impedance spectroscopy in Section 2.6, where Section 2.6 would also reveal some lithium-ion intercalation and deintercalation mechanisms.

2.5.2.1 Discharge–Charge Characterization

In Fig. 2.7 (a), we could observe that there is a slight bump at around 0.6 V in the first discharge curve from the galvanostatic charge-discharge profile of $FeSn_2$@C anodes. The slight bump could be caused by the irreversible formation of the SEI layer on the anode surface [112]. However, it disappears in the next second and third cycles. The lithiation of the anode could be reflected from the plateau between 0.3 and 0.0 V. In the second and third cycles, this plateau is heavily overlapped, which signifies the good electrochemical stability and reversibility of $FeSn_2$@C anodes. By comparing Fig. 2.7(a) and 2.7(b), it is shown that both $FeSn_2$@C nanocapsule-based anodes and $FeSn_2$ nanoparticle-based anodes have a high specific discharge capacity of 835 and 464 mAh/g, respectively.

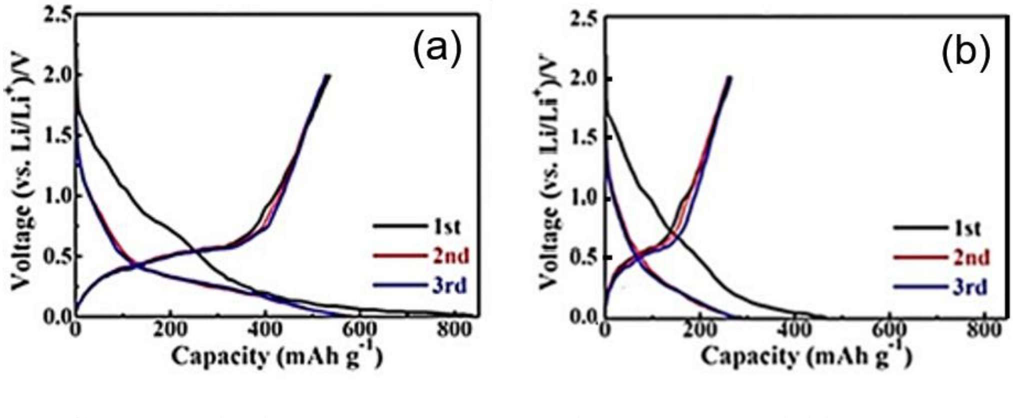

Fig. 2.7. Galvanostatic discharge-charge curves of LIB cells at the initial three cycles with (a) $FeSn_2$@C nanocapsules anode; and (b) $FeSn_2$ nanoparticles anode.

We could notice that the first specific discharge capacity of the $FeSn_2$@C anodes (835 mAh/g) was greater than the theoretical specific discharge capacity of the

$FeSn_2$ nanoparticle-based anodes (~804 mAh/g) [105]. The following four possibilities could attribute the greater capacity:

(1) The reduction reaction of $FeSn_2$ is assumed to be irreversible as the $FeSn_2$ theoretical capacity is based on the conventional alloying mechanism [113];

(2) The hollow-structured C shells with high surface area allow the Li^+ ions storage at the pores and interfaces of $FeSn_2$@C anodes [49], [103];

(3) The C shells have a high electric conductivity which facilitated the transfer of electrons during the lithiation/delithiation process [104], [114];

(4) Formation of organic polymeric/gel-like film could occur at the core/shell-structured anode interface. The film could enhance the capacity because of "pseudo-capacitance" [115].

In contrast, $FeSn_2$ nanoparticle-based anodes exhibit poor electrocatalytic performance because of their electrochemical instability caused by the exfoliation and pulverization of $FeSn_2$ nanoparticles during the lithiation/delithiation process [49], [58], [99]. The initial coulombic efficiency of $FeSn_2$ nanoparticle-based anodes was only 57.1% while comparing with ~64.2% of $FeSn_2$@C nanocapsule-based anodes. We can conclude that improved electrocatalytic properties of $FeSn_2$@C nanocapsules endow the excellent specific discharge capacity, maximized the voltage of cell at a low reaction potential, cyclic stability, and relatively minimal hysteresis loss with flat plateaus. Therefore, this makes $FeSn_2$@C as promising anodes for LIBs. Moreover, $FeSn_2$@C nanocapsule-based anodes have a low reaction potential to provide a degree of safety related to lithium plating [116].

2.5.2.2 Cyclic Characterization

Fig. 2.8 reveals the cycling performance of $FeSn_2$@C nanocapsule-based LIB and $FeSn_2$ nanoparticle-based anodes at a specific current density of 50 mA/g. The LIBs cycling performance is proportional to the electrochemical stability of anodes directly. After 100 charge-discharge cycles, the $FeSn_2$@C nanocapsule-based anodes show a specific discharge capacity of ~519 mAh/g with ~62.1% initial specific discharge capacity retention, while $FeSn_2$ nanoparticle-based anodes only show ~178 mAh/g with ~38.6% initial specific discharge capacity retention. The instability of cycling for the $FeSn_2$ nanoparticle-based anodes can be caused by the active retention of Li-Sn compounds, Li_2O matrix formation irreversibly, and Li^+ ions consumption continuously during SEI films formation and decomposition [60], [112]. In contrast, the $FeSn_2$@C nanocapsule-based anodes demonstrate a capacity reduction lower as 0.3% per each cycle. The major reasons for the improved performance are attributed to the surface area improvement, more efficient transfer of electrons across the conductive carbon shells, and the carbon shells protections for the $FeSn_2$ cores [117]. The carbon shells protect the core of the $FeSn_2$ nanoparticle to avoid direct contact between $FeSn_2$ and the electrolyte. This prevents the SEI formation on them, which delays the deactivation eventually. Thus, the specific capacity of the $FeSn_2$@C nanocapsule-based

LIB cells decreases gradually till the 70th cycle.

After the 70th cycle, we could observe a slight rise in capacity, as circled in Fig. 2.8. This capacity elevation could be ascribed to the anode activation delay [118]. We could not find such an activation period in $FeSn_2$-based LIB. The initial coulombic efficiency of the $FeSn_2$@C nanocapsule-based anode is only 64.2%, but it jumps to 92.5% in the 3rd cycle. The coulombic efficiency maintains till 100 cycles, indicating its high electrochemical stability and a highly reversible process of lithium insertion/extraction during the fast transportation of electrons within the electrodes. The initial low coulombic efficiency could be caused by the irreversible processes that caused some of the electrocatalytic active sites to become not active [115].

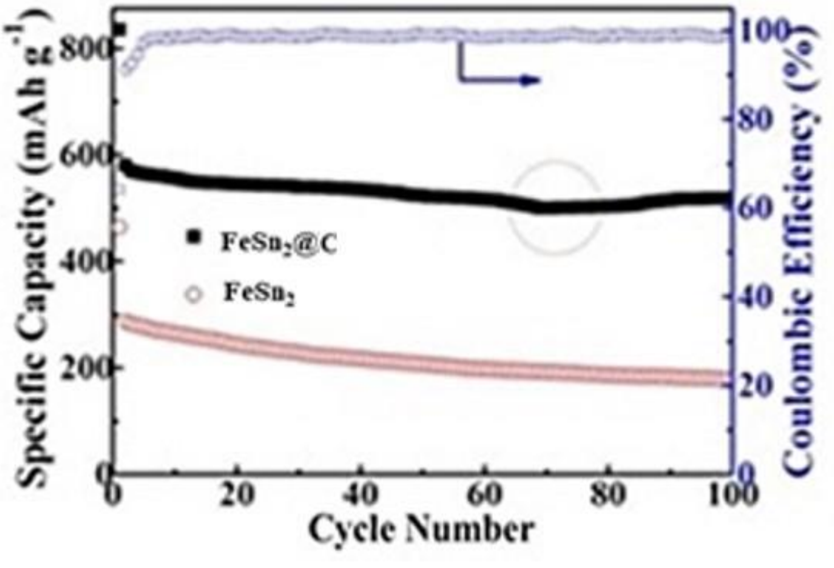

Fig. 2.8. The cyclic stability of LIBs with the $FeSn_2$@C nanocapsules anode and $FeSn_2$ nanoparticles anode at a current of 50 mA/g.

2.5.2.3 Rate Capability Characterization

$FeSn_2$@C nanocapsule-based LIB cells exhibit an improved rate capability than that of $FeSn_2$. From Fig. 2.9, we could observe that the $FeSn_2$ nanoparticle-based anodes at a specific current density of 50 mA/g show an initial specific discharge capacity of 464 mAh/g. However, the specific discharge capacity is reduced to 22 mAh/g with ~4.7% specific discharge capacity retention at a higher specific current density of 4000 mAh/g. When we return the specific current density to 50 mA/g, the specific discharge capacity recovers to only 232 mAh/g. The reason for this high loss is because $FeSn_2$ nanoparticles suffered huge volume changes during lithium insertion and removal. This leads to electrical contacts loss, particle fragmentation, and fading of capacity. By contrast, the $FeSn_2$@C nanocapsule-based anodes show 836 and 340 mAh/g specific discharge capacities at 50 and 4000 mA/g specific current density, respectively. When we return the specific current density to 50 mA/g, the specific discharge capacity can still remain at 564 mAh/g. This indicates a 67.5% specific discharge capacity retention compared with only 50% for the $FeSn_2$ nanoparticle-based anodes.

Moreover, the specific discharge capacity retention in the $FeSn_2$@C nanocapsule-based anodes in the second cycle can still remain for ~97.2% at 50 mA/g. This enhanced rate performance and electrochemical stability of the $FeSn_2$@C could be attributed to its smaller particle size that allows mass transfer rapidly between electrolytes and the electrode [49], [58]. Furthermore, the carbon shells provide the space needed for volume expansion during the lithiation/delithiation process [99], [103].

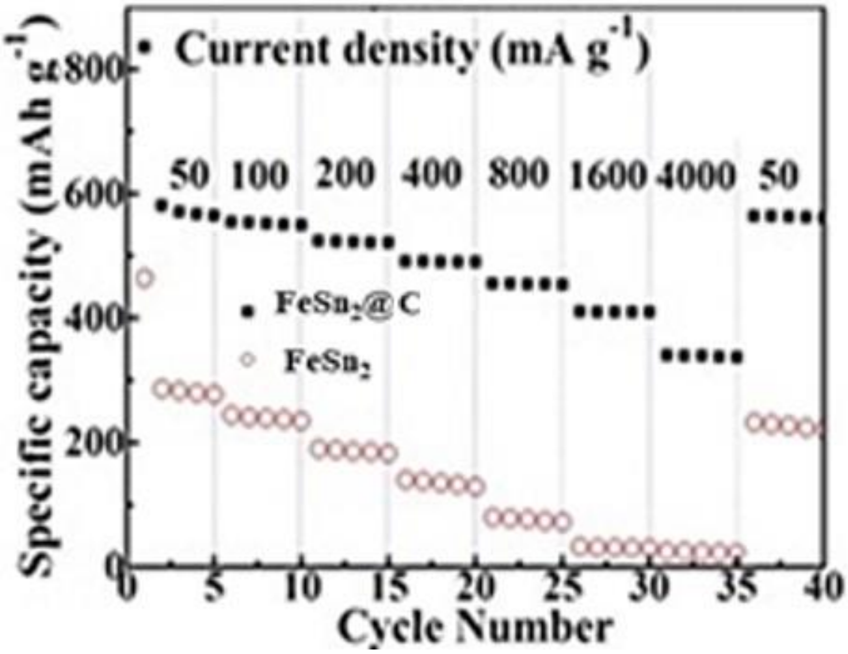

Fig. 2.9. Rate performance of FeSn$_2$@C nanocapsules anode and FeSn$_2$ nanoparticles anode.

2.6 Proposed Lithium-Ion Intercalation and Deintercalation Mechanisms

2.6.1 Cyclic Voltammetry

The curves for the first three cycles with voltage vs capacity for $FeSn_2$@C LIB are shown in Fig. 2.10 (a):

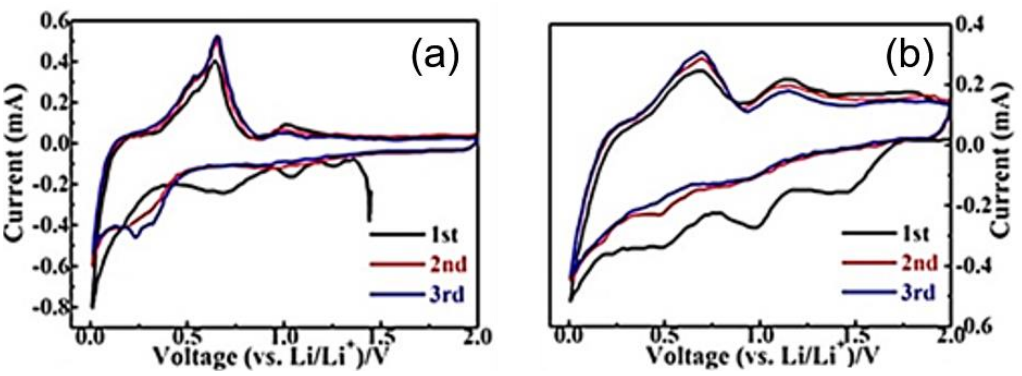

Fig. 2.10. CV curves of LIBs at the initial three cycles with (a) $FeSn_2$@C nanocapsules anode; (b) $FeSn_2$ nanoparticles anode.

When comparing with the paper investigating similar materials, the electrocatalytic reactions take place during the charge-discharge cycles are shown in Eq. (2.1)–(2.2) [112]. Eq. (2.1) illustrates the chemical reaction during lithiation, while Eq. (2.2) illustrates the chemical reaction during delithiation.

$$FeSn_2 + 8.8Li^+ + 8.8e^- \rightarrow 2Li_{4.4}Sn + Fe \tag{2.1}$$

$$2Li_{4.4}Sn + Fe \rightarrow FeSn_2 + 8.8Li^+ + 8.8e^- \tag{2.2}$$

At 0.7 V, the 1st cycle shows a comparatively broad cathodic peak. In the 2nd and 3rd cycles, multiple cathodic peaks exist. These peaks locate in between the operating voltage window. They are caused by the tin lithiation when the discharge process was taking place. In the 1st discharge process, the $FeSn_2$@C lithiation reaction potential and solid-electrolyte interface (SEI) formation potential is near to each other. Therefore, instead of forming multiple peaks, these potentials overlap each other and form a cathodic peak with a broader range [105]. During the anodic scan, the peak at 0.65 V represents the Li_xSn (LiSn and Li_5Sn_2) delithiation [99]. At about 1.0 V, the small peak is caused by the high reactivity of the surface for the small size controlled $FeSn_2$ stannide intermetallic alloy inside $FeSn_2$@C nanocapsules. At 0.7 V for all three cycles, the similar large cathodic peaks confirm excellent electrochemical stability caused by the deformation resistance from the robust $FeSn_2$@C nanocapsule-based anodes and reaction reversibility [112]. Nevertheless, there is a shift towards high voltages for the anodic peaks by the end of the 3rd cycle because the SEI layer increases the impedance, resulting in small polarization [54]. Comparing with the $FeSn_2$ CV curves shown in Fig. 2.10. (b), we could observe that the $FeSn_2$@C oxidation peaks are sharper than the $FeSn_2$ oxidation peaks. The sharper peak shows that $FeSn_2$@C nanocapsules provide better electrochemical kinetics resulted from their high conductive carbon shells. In the following cycles, the irreversible capacity attenuation causes the integrated peaks areas and intensity to reduce.

2.6.2 Nyquist Measurements

In order to examine the electrochemical properties of the active materials, electrochemical impedance spectroscopy (EIS) was carried out for both $FeSn_2$ nanoparticle-based anodes and $FeSn_2$@C nanocapsule-based anodes and in LIB cells, as shown in Fig. 2.11. In addition, we fitted the Nyquist plots by using ZView software. R_{ct}, R_s, Z_w, and CPE inside the equivalent circuit model represents the parameters of interface charge transfer resistance, ohmic resistance, Warburg impedance, and constant phase element, respectively. R_{ct} is representing the resistance from the electrode to the electrolyte during electrons transferring. R_s is represented by the intercept in the high-frequency region on the real axis, which arises from the electrode and electrolyte resistances. Z_w corresponds to electrons finite diffusion while passing through the anode. CPE is caused by the SEI layer that imparting the double layer capacitance [120], [121]. Gaining the benefits from the reduction of volume expansion and electrical conductivity enhancement for $FeSn_2$@C nanocapsule-based anodes, $FeSn_2$@C owes the characteristics of a lowered R_s both before and after cycling when comparing with that of $FeSn_2$ nanoparticle-based anodes [117]. Moreover, the reduced R_{ct} of $FeSn_2$@C can facilitate a quicker electron transfer and faster diffusion of Li^+ ions, thus improving the cycling performance at both low and high current densities.

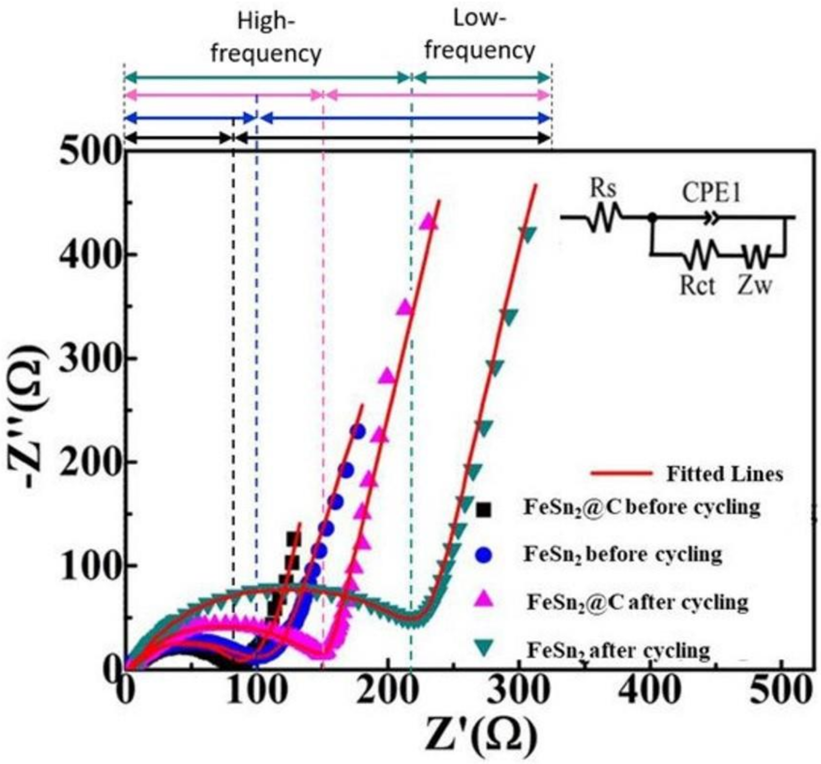

Fig. 2.11. Electrochemical impedance spectra (EIS) of LIB cells using $FeSn_2$@C nanocapsule-based anodes and $FeSn_2$ nanoparticle-based anodes. The inset shows the equivalent circuit used for fitting the experimental EIS data.

2.7 Summary

In this section, we have successfully adopted a facile in-situ one-pot arc-discharge method for synthesizing $FeSn_2$@C nanocapsules with core@shell structure. This material has successfully acted as a high-performance and stable electrocatalytic anode stannide based material for LIBs. By adopting an in-situ technique, the process of arc-discharge has enabled $FeSn_2$@C nanocapsules assembling. The technique novels simultaneously adopting intermetallic alloy, confining the crystal size to smaller than 50 nm, and combining core material with an onion-like conductive carbon shell. The corresponding LIBs have exhibited improved electrocatalytic performances. They have demonstrated enhanced cyclability, excellent reversible capacity, and high rate capability while they are compared by using nanoparticle $FeSn_2$ based anodes as comparisons. The core@shell structure is the major reason for improved electrocatalytic performances mentioned above. This structure can simultaneously enable lithiation processes reversibly during the charge and discharge process of the LIB cells provided by the $FeSn_2$ nanoparticle cores, and electro-stability is increased by the carbon shell that provides core protections from passivation induced by solid/electrolyte interphase and pulverization induced by volume change. The carbon shell has provided a good electro-conductivity, while it also confines the growth of the $FeSn_2$ nanoparticles to the size range between 5 nm and 50 nm. Therefore, the area of electrolyte/electrodes surface contact and electrochemical kinetics could be improved, and thus $FeSn_2$@C nanocapsule-based anodes had offered a comparatively lower resistance when we compared that with that of $FeSn_2$ nanoparticle. On the other hand, adopting carbon shells has overcome the deterioration of the electrocatalytic anode caused by lithiation/delithiation-induced volume changes, which are the most difficult issues in LIBs. They have also buffered the stress-induced for material expansion by providing space during lithiation. Thus, even after the 100th cycles, the $FeSn_2$@C nanocapsule-based anodes have demonstrated high retention of specific discharge capacity, showing their excellent electrochemical stability. Comparing this method with other reported methods, we can conclude that the arc-discharge method stands out for synthesizing electrocatalytic $FeSn_2$@C nanocapsule-based anodes with excellent performance. The comparison is summarized in Table 2.2

Table 2.2 Comparisons between arc-discharge method and traditional methods reported for synthesizing $FeSn_2$.

Method	Disadvantage of the corresponding method	Advantage of arc-discharge method
Solvothermal [54]	Complicated steps with huge solvent waste	One-pot with practically zero-waste
Chemical Reduction [95]	Nanoparticles aggregation	No aggregation
Ball-milling [96]	Lack of phase and structure control	Controllable phase and structure

While the arc-discharge method successfully alleviates the problems mentioned in the above table, it also provides a facile, environmentally friendly, economic, and scalable process practically without any waste [49], [58], [122]. We can extend this method for developing other core@shell-structured electrocatalytic materials that requiring morphology control for applications in LIBs, LOBs, and supercapacitors.

Chapter 3 MnO_2/Mn_2O_3 Hollow-Microcages as Cathode for Lithium–Oxygen Batteries

3.1 Introduction

After successfully developing core@shell-structured electrocatalysts for LIBs, the skills and knowledge learnt could now be applied to LOBs as promising electrocatalysts used in LIBs and LOBs share some similar properties such as high electro-conductivity and high resistance against detachment and pulverization during cyclic. In Section 1.3.3, we reviewed that transition metal oxides (TMOs) have drawn plenty of attentions as cathode materials for LOB fabrication while state-of-the-art hollow Mn_3O_4 nanocages bring lots of advantages among the similar types of TMOs. However, there are still some downsides that can be improved by enhancing the synthesis procedures and electrochemical performance for that specific method, as mentioned in Chapter 1.3.4: (1) long preparation time of manipulating sacrificial carbon templates; (2) high percentage of material loss due to multiple washing of materials; (3) low electronic conductivity that restricting ORR–OER kinetics; and (4) possibility of detachment and pulverization of nanostructured catalysts causing electrode material loss during cyclic. Downsides (1) and (2) are related to synthesis procedures issue, while (3) and (4) are related to material structure.

In chapter 3, we will focus on the discussion of modifying synthesis procedures of the manganese TMO hollow cages and verify the physicochemical characteristics and electrochemical performances of the modified materials correspondingly.

In order to minimize the material loss due to multiple washing of materials, vacuum filtration was used instead of centrifuge during washing to synthesize Mn_3O_4 carbon template derived manganese oxide nanoparticle hollow microcage (CTDMONpHMc). Vacuum filtration is a technique that separates solid products from solution or liquid. Compared with the centrifuge method, which uses a pipette to remove the unwanted liquid on top, vacuum filtration uses pressure to force the solution to pass through the filter paper quickly. Using the centrifuge method for washing requires the removal of unwanted liquid manually, and the target solid could also be removed as some solid could still be mixed with the liquid on the top of the tube. These affect the yield and experiment time negatively. In contrast, vacuum filtration removes the liquid by pressure. Also, most solid will stay on the surface of filter paper as the holes are too small for the solid to pass through. These characteristics improve both the yield and the experiment time required.

On the other hand, to minimize both the material loss and preparation time for sacrificial carbon templates, a facile two-steps templateless synthesis of MnO_2/Mn_2O_3 hybrid manganese oxide nanoparticle hollow microcage (HMONpHMc) is synthesized *via* a solvothermal method, forming a similar structure as CTDMONpHMc. This method has provided a time-saving alternative as it does not require to synthesize sacrificial carbon templates before forming the hollow microcages. Instead, the

HMONpHMc is formed during a single solvothermal procedure with the assisting of oxalic acid. The electrochemical performance of oxygen electrodes made of HMONpHMc is compared with CTDMONpHMc, and HMONpHMc shows an increase of both initial discharge capacity and capacity reversibility. In addition, the study of cyclic voltammetry and Nyquist measurements reveal the underneath ORR–OER mechanisms.

3.2 Synthesis

3.2.1 Materials

- Manganese(II) chloride tetrahydrate ($MnCl_2 \cdot 4H_2O$)
- Oxalic acid ($C_2H_2O_4$)
- Dimethylformamide (DMF)
- Glucose
- Deionized (DI) water
- Ethanol

3.2.2 Synthesis of MnO_2/Mn_2O_3 Hollow-Microcages

The HMONpHMc was synthesized *via* a solvothermal method followed by heat treatment. Briefly, a solution made of 4 mmole manganese(II) chloride tetrahydrate, 12 mmoles oxalic acid, and 35 mL of DMF was heated up in a 50 mL Teflon-lined autoclave at 200 °C for 24 hours. Next, the product was washed with DI water and ethanol five times by vacuum filtration. Then it was dried at 60 °C for 12 hours. Finally, the product was calcinated at 450 °C for two hours in the air to form brownish manganese oxides, named as HMONpHMc.

3.2.3 Synthesis of Mn_3O_4 Hollow-Microcages

The procedures of synthesizing CTDMONpHMc were modified base on a published article [85]. In the beginning, carbon templates needed to be prepared first.

4 g of glucose was dissolved in 35 mL of DI water. After stirring for 20 minutes, they formed a clear solution. The solution was then heated in a 50 mL Teflon-lined autoclave for 22 hours at 160 °C. The product obtained washed with DI water and ethanol five times each by vacuum filtration. Finally, the carbon nanospheres were isolated and dried at 60 °C for 12 hours.

To synthesize CTDMONpHMc from the carbon templates, dropped 50 mL of 1 M $MnCl_2$ solution into 2 g of carbon templates. Next, ultrasonicated the slurry for 50 min and aged under room temperature for 12 hours. Then, isolated the product and washed it with DI water by vacuum filtration. We finally heated the washed product in the presence of air at 450 °C for one hour.

3.3 Physicochemical Evaluations

3.3.1 Evaluation Methods

3.3.1.1 X-ray Diffraction

The preparations and setups are the same as mentioned in Section 2.3.1.1.

3.3.1.2 Transmission Electron Microscopy

The preparations and setups are the same as mentioned in Section 2.3.1.2.

3.3.1.3 Accelerated Surface Area and Porosimetry System

The Micromeritics Accelerated Surface Area and Porosimetry (ASAP) system is applied to measure the surface area and pore size of the sample of interest. It internally applies the physical or chemical adsorption principle to obtain corresponding adsorption information and isotherms.

For the preparation of samples, the sample should be cleaned to remove contaminants absorbed while the samples were exposed to the surrounding atmosphere. Therefore, degassing processes were proceeded by is heating the samples and placing them under vacuum, so that remove contaminants and moisture were removed *via* the SmartVac degassing system.

After degassing the samples at 150 °C for 6 hours under vacuum, the specific surface area was measured using the N_2 adsorption/desorption isotherm curves. These curves were obtained from Micromeritics ASAP 2020 accelerated surface area and porosimetry system based on the Brunauer-Emmett-Teller (BET) method at $0.15 < P/P_0 < 0.45$ and temperature of 77 K, while the pore volume was calculated using the adsorption Barrett–Joyner–Halenda (BJH) method.

3.3.2 Result and Discussion

Fig. 3.1 (a) and Fig. 3.1 (b) show the synthesis procedures of CTDMONpHMc and HMONpHMc, respectively:

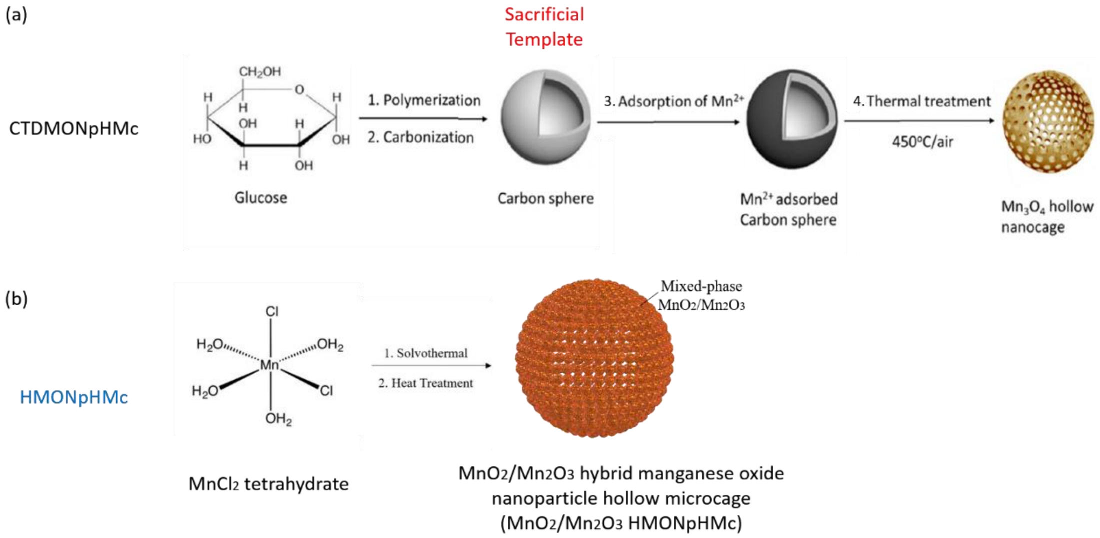

Fig. 3.1. Schematic illustration of (a) CTDMONpHMc; and (b) HMONpHMc formation. Modified based on [85].

The HMONpHMc synthesized *via* solvothermal method shows two distinct advantages when comparing with CTDMONpHMc. First, the preparation time of HMONpHMc is much shorter than that of CTDMONpHMc. Referring to Fig. 3.1 (a), synthesizing CTDMONpHMc requires four steps. The first two steps are required for the preparation of sacrificial template. The template will be burnt out during the thermal treatment in step 4. The whole process mentioned in the published article [85] requires one consecutive week, while preparing the sacrificial template takes 4 days and ultrasonicating followed with thermal treatment takes another 3 days. If we use vacuum filtration instead of centrifuge during the washing process, 2 days can be saved due to the ease of washing. In comparison, synthesizing HMONpHMc requires two steps only and takes only 3 days. The new method this work introduced successfully simplifies the synthesis procedures and saves more than 60% preparation time. Second, the product yield of the HMONpHMc is increased hugely. For comparison purpose, 5 sets of CTDMONpHMc by centrifuge washing, 5 other sets of CTDMONpHMc by vacuum filtration washing, and 5 other sets of HMONpHMc were synthesized, respectively. The same amount of manganese sources (manganese(II) chloride tetrahydrate) were weighted and used before the experiment and the final product were weighted after all the processes completed. The percentage yield was then calculated by the equation shown in Eq (3.1):

$$\text{Percentage Yield} = \frac{\text{Actual Yield}}{\text{Theoretical Yield}} \tag{3.1}$$

, where the actual yield refers to the final measured weight of CTDMONpHMc or HMONpHMc; and theoretical yield refers to the measurement for the intended pure product that based on chemical equations. The calculated product yield of CTDMONpHMc by centrifuge washing and vacuum filtration washing is in the range between 5-10% and 10-15%, respectively. In contrast, HMONpHMc gives product yields between 30-40%. The significant improvement of product yield of HMONpHMc could be contributed by reducing the frequency of material washing so that the material loss could be decreased.

In the sections below, we will reveal the physiochemical properties of HMONpHMc and CTDMONpHMc in Section 3.3.2.1–3.3.2.3 and corresponding electrochemical performances for LOBs in Section 3.5 to show that this simplified HMONpHMc method can synthesize material with similar morphology and also deliver satisfactory electrochemical performances for LOBs when comparing with that of CTDMONpHMc.

3.3.2.1 Crystal Structure Analysis

Manganese oxides phase highly depends on the annealing time. From the XRD results, CTDMONpHMc with thermal treatment of 450 °C for 2 hours shows a pure hausmannite Mn_3O_4 material with JCPDS 24-0734, as shown in Fig. 3.2 (a). It shows that all the characteristic peaks correspond to (112), (103), (211), (004), (321), and (224) millers indices. The lack of any other peaks implies the material is highly phase pure.

XRD of HMONpHMc in Fig. 3.2 (b) shows characteristic peaks at $2\theta = 33°$ and 37°, which is a signal of multiple phases existence. The phases represent on the graph refers to β-MnO_2 with 24-0735 JCPDS number and bixbyite Mn_2O_3 with 41-1442 JCPDS number. Both β-MnO_2 and Mn_2O_3 shows peaks with sharp and high intensities. Besides those sharp peaks, no other peaks could be observed, implying that both materials are highly pure.

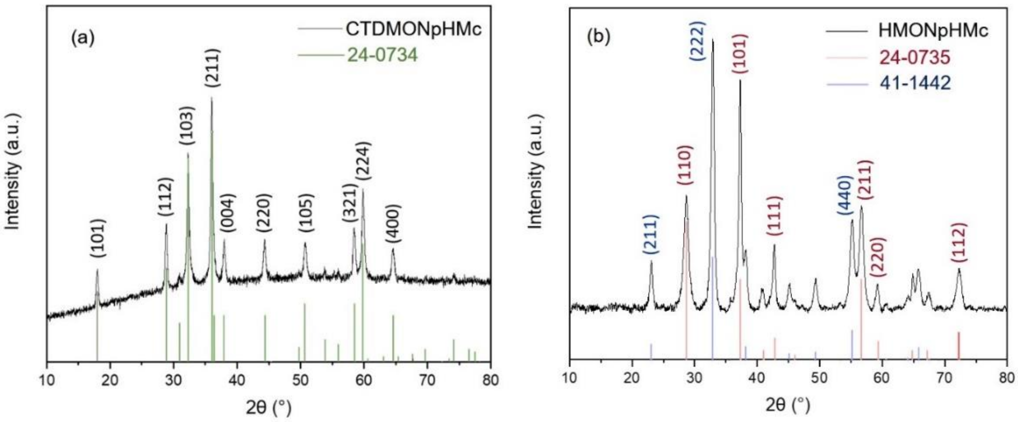

Fig. 3.2. The XRD patterns of (a) CTDMONpHMc; and (b) HMONpHMc.

3.3.2.2 Morphology Analysis

The images of CTDMONpHMc and HMONpHMc in TEM and HRTEM are shown in Fig. 3.3. CTDMONpHMc in Fig. 3.3 (a) and HMONpHMc in Fig. 3.3 (b) both represent hollow microspheres that are highly mesoporous. CTDMONpHMc has an average diameter of about 1 μm, while HMONpHMc has an average diameter of around 0.6 μm. Furthermore, HRTEM investigation in Fig. 3.3 (c) and Fig. 3.3 (d) reveal that both CTDMONpHMc and HMONpHMc contain nanoparticles of manganese oxide in round shape with about 10 to 20 nm diameter as building blocks. The nanoparticles are aggregated and inter-connected to each other to build NpHMcs. These connected nanoparticles provide paths for mass transport of oxygen and lithium-ion [123] and firmer structure to resist the pulverization of materials during discharge/charge reaction.

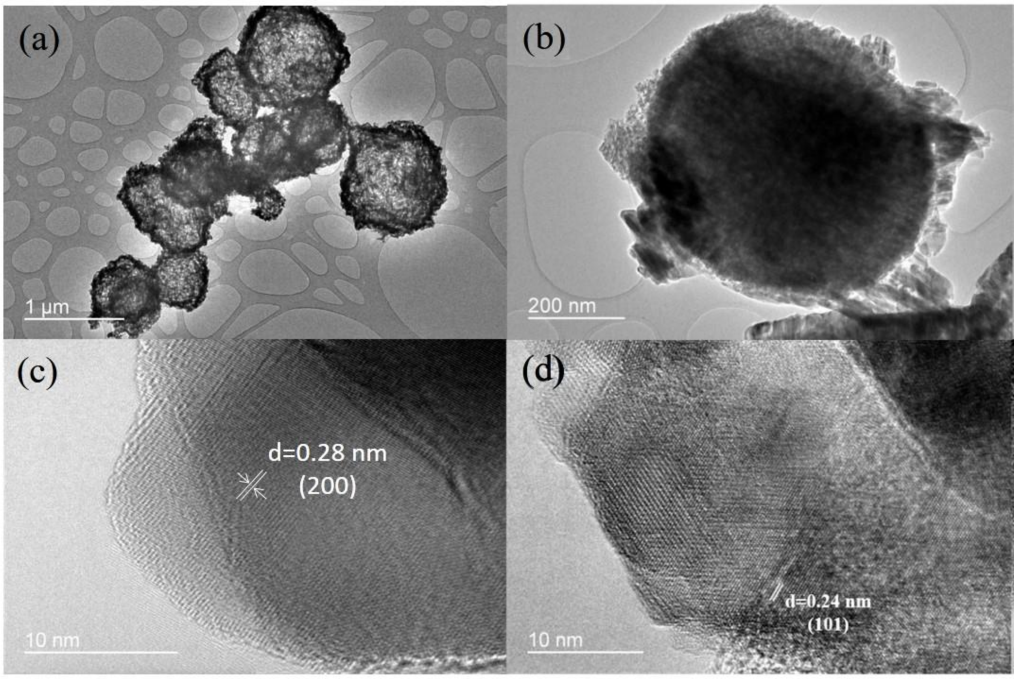

Fig. 3.3. TEM and HRTEM images of (a) and (c) CTDMONpHMc and (b) and (d) HMONpHMc, respectively.

3.3.2.3 Surface Area and Porosimetry Analysis

In Fig. 3.4, the BET surface area of HMONpHMc is calculated using nitrogen adsorption and desorption isotherms and compared with that of CTDMONpHMc suggested in the published article [85]. From the specification of IUPAC nomenclature, the hysteresis loops of both HMONpHMc and CTDMONpHMc correspond to type IV that shows indications of mesoporous structures [124]. The BET surface areas of HMONpHMc and CTDMONpHMc are about 54.81 and 90.65 m^2/g, respectively. While both materials have a high BET surface area compared with similar nanoparticles, CTDMONpHMc has a comparatively high surface area. However, HMONpHMc possesses a larger pore volume (0.185 m^3/g) than CTDMONpHMc (7.7×10^{-8} m^3/g). The larger pore volume implicit a relatively high impact on initial discharge and cycling performance [125].

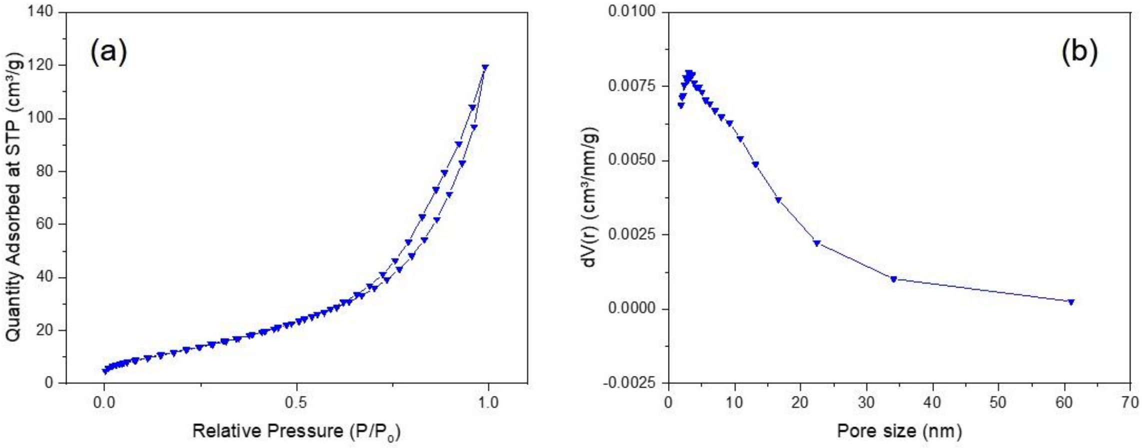

Fig. 3.4. (a) N_2 adsorption/desorption isotherm; and (b) pore size distribution of HMONpHMc.

3.4 Hollow-Microcages as Cathode and their Lithium–Oxygen Battery Cells

3.4.1 Materials

- HMONpHMc and CTDMONpHMc prepared in Section 3.2.2
- Carbon black, Super P® (SP)
- Carboxymethyl cellulose (CMC)
- Lithium foil
- Glass fiber separator
- Carbon Paper (CP), cut in a circle shape with 16mm diameter
- Lithium bis(trifluoromethanesulfonimide) in tetra(ethylene glycol) dimethyl ether (LiTFSI in TEGDME)
- DI water

3.4.2 Preparation of MnO_2/Mn_2O_3 Hollow-Microcages as Cathode

A homogeneous slurry made of HMONpHMc, SP, and CMC with a 50:40:10 weight percentage ratio dissolved in DI water was cast onto CP. The coated CPs were dried at 80 °C for 12 hours in a vacuum oven. The average mass loading of the HMONpHMc and SP was 0.5 ± 0.05 mg/cm^2. For a comparison, cathodes made of CTDMONpHMc was prepared following the same technique.

3.4.3 Fabrication of Lithium–Oxygen Battery Cells

LOB cells were fabricated using an EQ-STC-Li-air split cell (KJ Group, STC-ZINCAIR) in an argon filled glove box with H_2O and O_2 content less than 0.1 ppm. Briefly, the cells were constructed using the lithium foil as the anode, glass fiber separator soaked in 60 μL 1M LiTFSI in TEGDME electrolyte, and the cathode. Cells were sealed, purged with 99.7% pure O_2 for 30 minutes, and kept for 3 hours under open-circuit voltage before performing electrochemical measurements.

The schematic diagram of the LOB cell construction is demonstrated in Fig. 3.5:

Fig. 3.5. Schematic of LOB cell construction.

3.5 Electrochemical Characterizations

3.5.1 Characterization Methods

3.5.1.1 Galvanostatic Measurements

The LOB cells discharge-charge galvanostatic profiles were examined from the model "LANDT 2001 CT battery tester" within the voltage window at various currents between 2 V to 4.5 V. We evaluated the cyclability at upper limit specific capacity of 500 mAh/g and specific current of 200 mA/g. Based on the mass loading of HMONpHMc and CTDMONpHMc as the active material in the cathode, the current densities and specific capacities were calculated, respectively.

3.5.1.2 Electrochemical Impedance Spectroscopy

We used the Electrochemical Workstation to conduct the cyclic voltammetry plot with model CHI 660E at 2 - 4.5 V voltage range and 5 mV/s voltage sweep rate. Before the first cycle, we recorded the impedance spectrum for LOB cells Nyquist plots at 1 Hz to 105 Hz frequency range and 5 mV perturbation amplitude. After that, we used ZView software to fit the EISs with equivalent circuits.

3.5.2 Result and Discussion

3.5.2.1 Discharge–Charge Characterization

By comparing their first discharge–charge curves, electrochemical performances of HMONpHMc and CTDMONpHMc cathodes for LOBs are examined, as shown in Fig. 3.6. HMONpHMc shows a 1070 mAh/g first discharge specific capacity at 200 mA/g current density, higher than 712 mAh/g for CTDMONpHMc. On the other hand, the HMONpHMc voltage discharge plateau is higher for about 80 mV than CTDMONpHMc. At the same time, the voltage charge plateau of HMONpHMc is nearly the same when compared with CTDMONpHMc. These evaluations imply HMONpHMc has improved electrochemical performance compared with CTDMONpHMc during discharge.

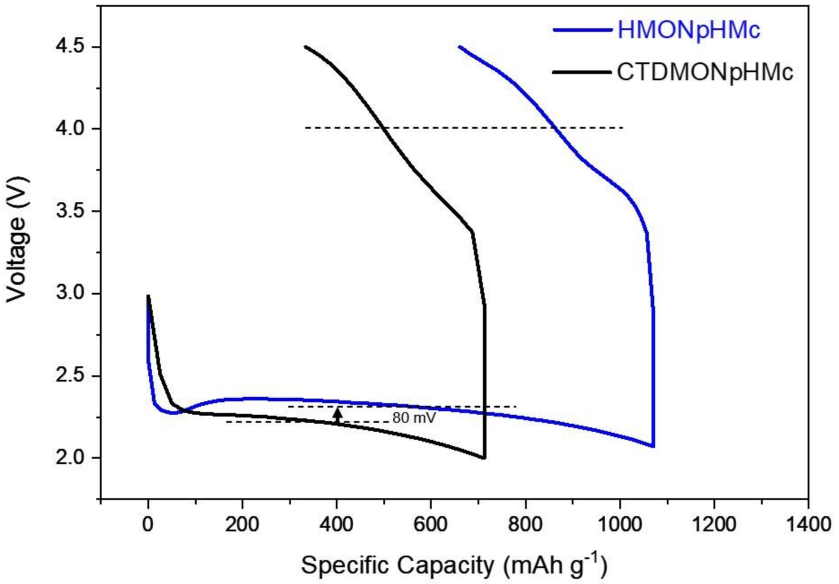

Fig. 3.6. The first discharge/charge curves for HMONpHMc and CTDMONpHMc cathodes with full capacity at a 200 mA/g current density.

3.5.2.2 Cyclic Characterization

For the cyclic performance evaluation for LOBs, the discharge capacity is limited to 500 mAh/g so as to avoid decomposition of electrolyte [126]. Fig. 3.7 (a)–(d) reveals that 31 reversible cycles can be sustained for the HMONpHMc cathode while only can last 18 cycles for CTDMONpHMc cathode at the upper limit capacity. The reason for HMONpHMc cathode demonstrating a longer number of cycles could be attributed to their higher pore volume, which enables the accommodation of discharge products [127]. This allows the maintenance of cyclic stability as Li_2O_2 side product produced can be decomposed and not able to block the larger pores. After 32 cycles, the Li_2O_2 side product in HMONpHMc cathode is getting more difficult to decompose as the active sites of material are blocked and cannot accommodate the great amount of Li_2O_2 side product. Thus, the capacity decreases, and the LOB becomes non-functional.

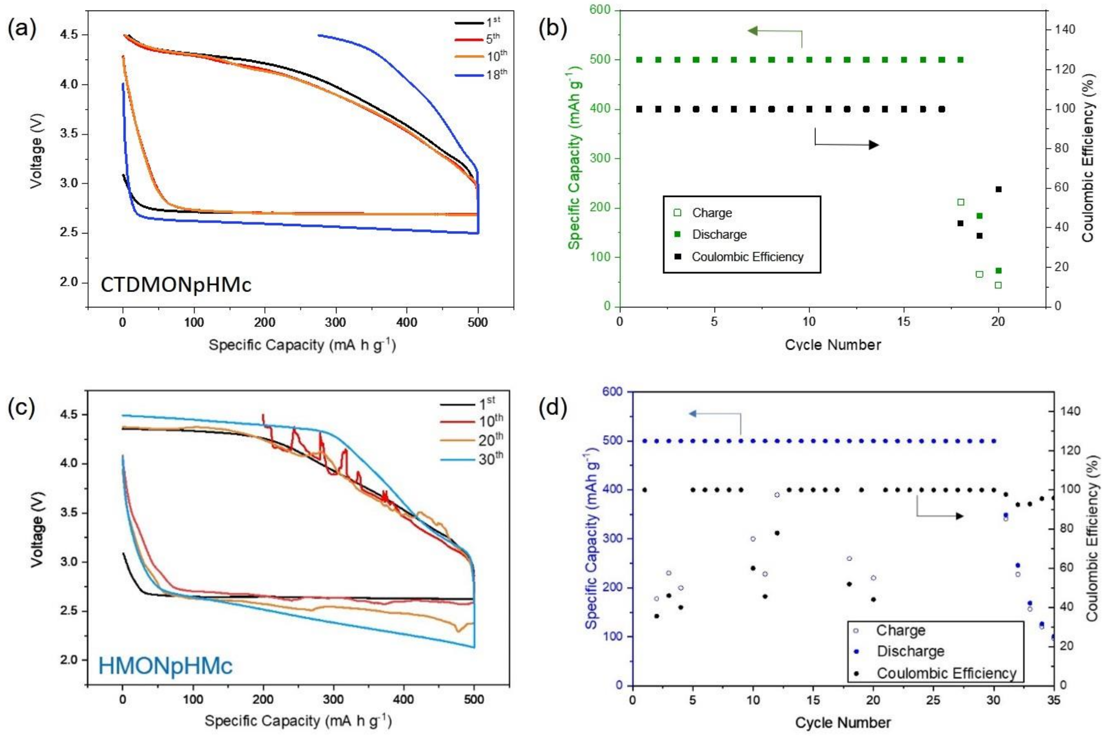

Fig. 3.7. Discharge–charge curves at different cycles (a) and (c). Cyclic performance and coulombic efficiencies of (b) CTDMONpHMc and (d) HMONpHMc cathode-based LOBs. All LOBs discharge/charge were subjected to an upper limit capacity of 500 mAh/g at 200 mA/g current.

3.6 Proposed Oxygen Reduction Reaction/Oxygen Evolution Reaction Mechanisms

3.6.1 Cyclic Voltammetry

ORR/OER kinetics during discharge/charge is observed *via* conducting cyclic voltammetry measurements. The first CV cycles of CTDMONpHMc and HMONpHMc are shown in Fig. 3.8 (a) and Fig. 3.8 (b), respectively. Both CTDMONpHMc and HMONpHMc show one distinct peak during the potential scanning in the negative direction. CTDMONpHMc shows an ORR peak at 2.35 V while HMONpHMc shows an ORR peak at 2.25 V. This reflects the formation of lithium peroxide [128]. The corresponding chemical equation is shown in Eq. (3.2):

$$2Li^{+} + 2e^{-} + O_2 \rightarrow Li_2O_2 \qquad (3.2)$$

Similarly, CTDMONpHMc and HMONpHMc both show one distinct peak during positive scanning. However, CTDMONpHMc shows an OER peak at 3.25 V while HMONpHMc shows an OER peak at 3.5 V. This reflects the decomposition of lithium peroxide [128]. The corresponding chemical equation is shown in Eq. (3.3):

$$Li_2O_2 \rightarrow 2Li^{+} + O_2 + 2e^{-} \qquad (3.3)$$

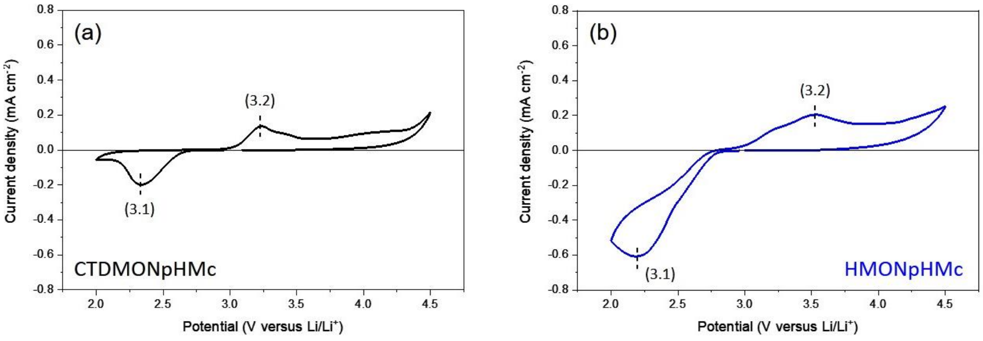

Fig. 3.8. The first CV cycles of (a) CTDMONpHMc; and (b) HMONpHMc.

We can observe that the HMONpHMc current density is three times as high as CTDMONpHMc for scanning in the negative direction. For a complete scanning cycle, the larger area of HMONpHMc when compared with CTDMONpHMc implies a higher electrochemical active surface area could be provided by HMONpHMc [129].

3.6.2 Nyquist Measurements

Before cycles, we obtained the EIS spectra for CTDMONpHMc and HMONpHMc electrodes, as shown in Fig. 3.9. The impedance spectrum is fitted by using Zview software. We obtain an equivalent circuit model, which is also shown in Fig. 3.9.

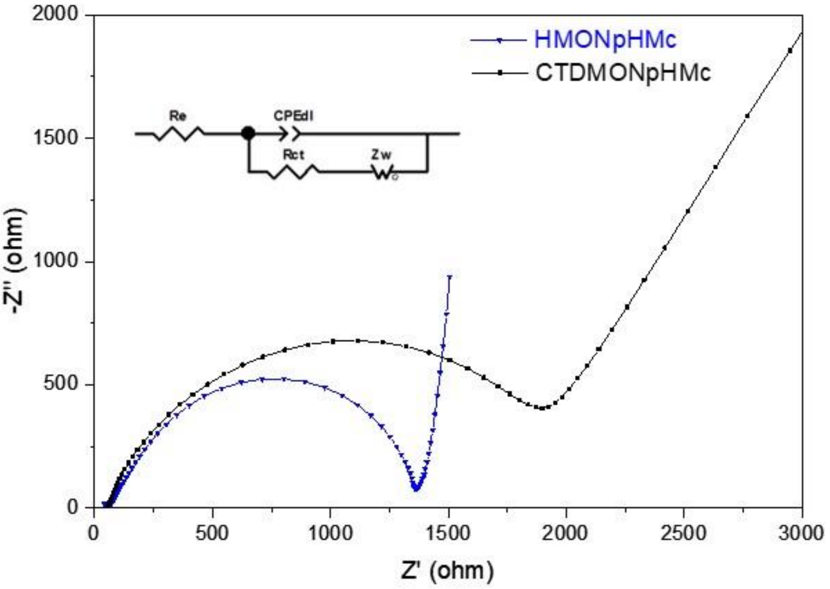

Fig. 3.9. EIS spectra of HMONpHMc and CTDMONpHMc electrodes obtained before cycles. The equivalent circuit model is shown as an inset.

R_e, R_{ct}, Z_w, and CPE_{dl} refer to electrolyte ionic resistance, charge transfer resistance, diffusion resistance, and double-layer constant phase element in the equivalent circuit model, respectively. Table 3.1 lists the impedance values.

Table 3.1. Impedance parameters calculated from the equivalent circuit for HMONpHMc and CTDMONpHMc.

	HMONpHMc	**CTDMONpHMc**
R_s/ Ω	86.6	54.0
R_{ct}/ Ω	1280	2023
CPE_{dl}/ μF	45.1	1.2
Z_w/ Ω	140	180

From the table, HMONpHMc demonstrates a noticeably lower R_{ct}. This represents the kinetic resistance at the electrode/electrolyte interface [83], affecting the LOB cyclic. The possible reason for lower R_{ct} could be caused by the improved electric conductivity provided by MnO_2/Mn_2O_3 hybrid instead of low conductivity Mn_3O_4 as it is reported that the specific balance of mixed phases in MnO_2/Mn_2O_3 hybrid results from enhanced surface conductivity [130]–[132].

3.7 Summary

In this work, mixed-phase MnO_2/Mn_2O_3 hybrid manganese oxide nanoparticle hollow microcages (HMONpHMc) have been prepared by oxalic acid-assisted solvothermal synthesis. Comparing to the state-of-the-art sacrificial template method, the synthesis method introduced in this work is a simplified template-free method that has provided a time-saving alternative with low material loss by reducing the frequency of material washing. Table 3.2 summarizes some of the experimental measurements and results for CTDMONpHMc suggested by a published article [85], CTDMONpHMc by modified vacuum filtration method, and HMONpHMc.

Table 3.2 Summary of experimental measurements and results for CTDMONpHMc and HMONpHMc.

	CTDMONpHMc (Centrifuge)	**CTDMONpHMc (Vacuum Filtration)**	**HMONpHMc**
Carbon Template Diameter	150–250 nm	350–450nm	-
Manganese particle diameter	~30nm	~30nm	~10-20 nm
Hollowcages Diameter	250–300nm	500–1000nm	~600nm
Material Constitutions	Mn_3O_4	Mn_3O_4	Mixed phase MnO_2/Mn_2O_3
Product Yield	5-10%	10-15%	30-40%
Preparation Time	7 days	5 days	3 days

HMONpHMc has been adopted as electrocatalytic cathodes material for LOB. It is then compared with CTDMONpHMc by modified vacuum filtration method physiochemically and electrochemically. HMONpHMc shows a similar structure compared with CTDMONpHMc, except it constitutes MnO_2/Mn_2O_3 hybrid instead of pure Mn_3O_4. HMONpHMc-based cathodes have also demonstrated increased electrochemical performances in both first discharge capacity and cyclability compared with CTDMONpHMc. The result could be contributed by its comparatively larger pore volume and lower kinetic resistance at the electrode/electrolyte interface caused by the improved electric conductivity.

Chapter 4 Mn_3O_4@C Microspheres as Cathode for Lithium–Oxygen Batteries

4.1 Introduction

In chapter 3, we successfully synthesize hybrid manganese oxide nanoparticle hollow microcages (HMONpHMc), which consists of mix-phase MnO_2/Mn_2O_3, by simplified and time-saving procedures. Not only the product yield of synthesizing HMONpHMc was increased, but the HMONpHMc-based LOB also demonstrated enhanced electrochemical performances when comparing with the traditional sacrificial carbon template method. However, there are still serval problems faced for the HMONpHMc. First, the surface area of HMONpHMc is comparatively lower when comparing with CTDMONpHMc, as described in Section 3.2.3.3. The area difference could somehow affect the formation of solid discharge product Li_2O_2 that caused the cathode passivation. Thus, the cyclic life is lowered. Second, the electrical conductivity of manganese oxide is low ($\sigma \approx 10^{-7}$–10^{-8} S/cm) that restricts ORR–OER kinetics, as mentioned in Section 1.3. Even we adopted hybrid materials, the conductivity still could be improved by using some techniques in material engineering.

In this chapter, core@shell-structured Mn_3O_4@C mesoporous multi-hollow microsphere (MpMhMs) is synthesized via facile templateless synthesis of HMONpHMc mentioned in chapter 3, followed by glucose coated-HMONpHMc carbonization in a single step. The MpMhMs combines the substantial benefits of nanoparticle catalysts innovatively as the building block forming NpHMc for the core, with defective carbon layers as the shell, to form multicore–shell-structured microspheres. This novel structure features enhanced ionic and electronic conductivity enhancing and stabilizing ORR–OER against Li_2O_2 passivation, protective carbon surface to minimize the loss of electrode material, large pore volume for the accommodation of discharge products, and high specific surface area that is favorable for catalytical reactions. Hence, these unique structures have enabled the carbon and HMONpHMc to act as complementary roles compared with Mn_3O_4 nanoparticles or porous carbon individually.

4.2 Synthesis

4.2.1 Materials

- HMONpHMc prepared in Section 3.2.2
- Glucose
- Deionized (DI) water
- Ethanol
- Tetra(ethylene glycol) dimethyl ether (TEGDME)

4.2.2 Synthesis of Mn_3O_4@C Microspheres

The carbon shell of HMONpHMc was prepared by using glucose. First, 0.01 g of glucose was added to a solution consisting of 35 mL DI water and 0.02 g HMONpHMc. Next, we heated the solution in a 50 mL Teflon-lined autoclave for ten hours at 180 °C. After that, the product was washed using DI water and ethanol five times each by vacuum filtration. The product was dried for 12 hours at 60 °C. Finally, annealed the as-prepared powder for carbonization under argon gas for four hours at 450 °C to obtain MpMhMs.

4.3 Physicochemical Evaluations

4.3.1 Evaluation Methods

4.3.1.1 X-ray Diffraction

The preparations and setups are the same as mentioned in Section 2.3.1.1.

4.3.1.2 Transmission Electron Microscopy

The preparations and setups are the same as mentioned in Section 2.3.1.2.

4.3.1.3 Carbon Content Analysis

Raman Spectroscopy is a non-destructive analyzing technique that uses scattered light to measure a sample’s vibrational energy modes. Chemical structure, crystallinity, phase, and molecular interactions could be provided by using this technique. The corresponding principle is based on the interactions of light with a material’s chemical bonding.

In this experiment, Raman spectroscopy was conducted at 514 nm laser excitation wavelength. The model used is Renishaw Micro-Raman Spectroscopy, which also equipped with a confocal microscope and a multichannel CCD detector.

4.3.1.4 Accelerated Surface Area and Porosimetry System

The preparations and setups are the same as mentioned in Section 3.3.1.3.

4.3.1.5 Thermogravimetric Analysis

Thermogravimetric analysis (TGA) is a technique that could discover the thermal stability of a material. During the testing, a sample of interest is continually heating and weighting between an atmosphere with inert gas passing over it. As plenty of solids will undergo reactions during heating which evolve byproducts in gas form, we can observe the percentage of volatile components by determining weight difference at a constant heating rate. This reaction allows us to identify the amount of gases removed and the occurring temperature simultaneously.

The compositions were investigated by thermogravimetric analysis at a ramping rate of 10 °C per minute from 25 °C to 900 °C in air. The model used for TGA is Mettler Toledo TGA/DSC3+.

4.3.1.6 Scanning Electron Microscopy

A scanning electron microscopy is a technique producing pictures and images of a sample of interest by using a beam of electrons for scanning. By adopting a focused electrons beam, the electrons from the electrons beam will interact with sample atoms. The interaction produces a wide range of signals which relates to sample composition and surface topography information. When comparing with TEM, SEM provides images in micro-scale instead of nanoscale. Hence, SEM is suitable for observing the morphology changes of postmortem in a wider area range.

The cathodes of interest were prepared inside a glove box with less than 0.1 ppm water and oxygen contents. After washing the used cathodes using TEGDME, we dried them in an argon-filled glove box at room temperature. The postmortem characterizations were performed by using SEM (Tescan VEGA3).

4.3.2 Result and Discussion

4.3.2.1 Crystal Structure Analysis

Fig. 4.1 illustrates both synthesis procedures of HMONpHMc and MpMhMs. In step 2 and step 4, high-temperature processing is required that would highly affect the manganese oxides phase (such as Mn_2O_3, Mn_3O_4, and MnO) formation because the phase of manganese oxides is greatly dependent on the annealing time [133].

Fig. 4.1. Schematic illustration of HMONpHMc and MpMhMs formation.

After two hours of heat treatment in step 2 at the temperature of 450 °C, XRD of HMONpHMc in Fig. 4.2 (a). shows characteristic peaks at 33° and 37°. These peaks imply the formation of multiple phases, including a mixed phased oxide hybrid of bixbyite Mn_2O_3 with JCPDS number of 41-1442 and rutile β-MnO_2 with JCPDS number of 24-0735. In step 4, the carbonization procedure forms carbon coating for MpMhMs under argon for 4 hours at 450 °C. This results in the formation of core material in pure hausmannite Mn_3O_4 with JCPDS 24-0734, as shown in Fig. 4.2. (b). The average crystalline size of MpMhMs has estimated with the value of ~12.6 nm by using the Scherrer formula [134], as shown in Eq (4.1):

$$\tau = \frac{K\lambda}{\beta cos\theta} \tag{4.1}$$

, where β corresponds to the full width at half maximum; λ refers to the X-ray wavelength; K stands for the shape factor, which depends on the shape of crystallite; and θ refers to the Bragg's angle. We cannot observe any carbon peaks in XRD spectra because the coated carbon amount is very little compared with the amount of oxides.

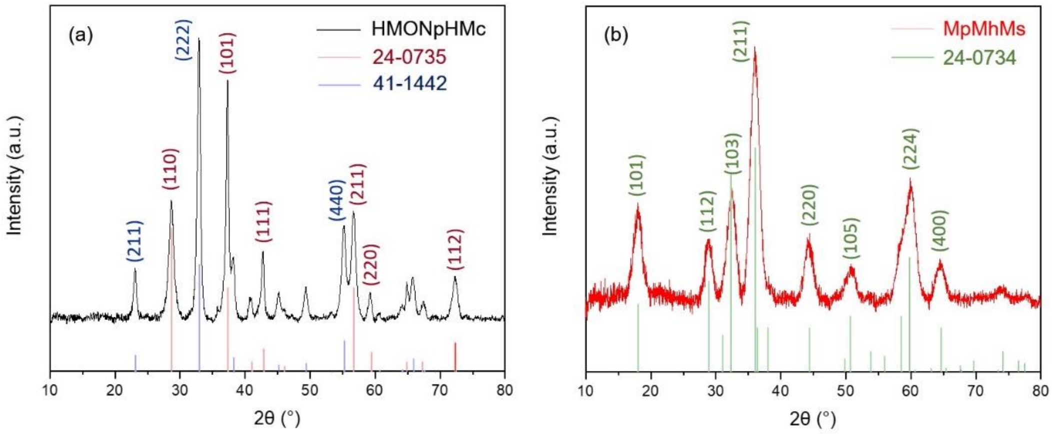

Fig. 4.2. The XRD patterns of (a) HMONpHMc; and (b) MpMhMs.

4.3.2.2 Morphology Analysis

Fig. 4.3 (a)–(d) show HMONpHMc and MpMhMs images in the TEM and HRTEM. In Fig. 4.3 (a) and 4.3 (b), HMONpHMc and MpMhMs both demonstrate hollow microspheres that are highly mesoporous with about 0.6 μm average diameter. In Fig. 4.3 (c), the HMONpHMc in HRTEM shows a lattice distance of 0.24 nm. This plane represents to (101) lattice planes of MnO_2 with JCPDS number 24-0735. On the other hand, MpMhMs in Fig. 4.3 (d) shows the 0.31 nm lattice spacing. The spacing corresponds to (112) lattice planes in Mn_3O_4 with JCPDS number 24-0734. These HRTEM crystallographic planes match with XRD results well shown in Fig. 4.2.

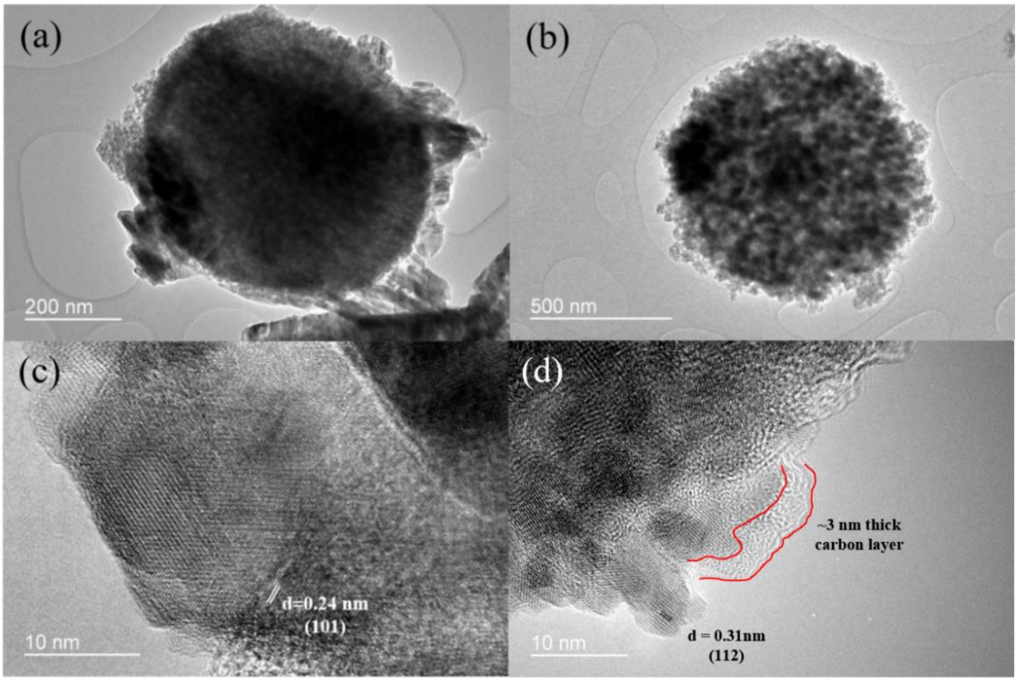

Fig. 4.3. Images of TEM and HRTEM for (a) and (c) HMONpHMc; and (b) and (d) MpMhMs.

Moreover, the HRTEM images of HMONpHMc and MpMhMs in Fig. 4.3 (c) and 4.3 (d) shows that HMONpHMc and MpMhMs contain a great deal of round-shaped manganese oxide nanoparticles which act as building blocks with a diameter around 10 nm to 20 nm. These nanoparticles size matches the Scherrer formula evaluation for the size of crystallites from section 4.3.2.1. The size proves the formation of single crystalline in Mn_3O_4 nanoparticles inside powder of MpMhMs. These connected nanoparticles could give more open paths for mass transport of Li^+ ion and oxygen [123]. Also, they could offer a more durable structure for volume changes buffering caused by Li_2O_2 deposition storage in between discharge and charge. Fig. 4.3 (d) shows that some amorphous spongy-like porous carbon layers with around 3 nm thick were formed. They posited on the outer layer of the interconnecting building blocks. The layers could enhance the resistivity of catalyst for avoiding pulverization during the cyclic.

Similar carbon shell synthesis procedures were also applied for CTDMONpHMc mentioned in chapter 3 as core material. However, we did not obtain a satisfactory result. In Fig. 4.4, we can observe that the NpHMc structure of CTDMONpHMc deforms and crystallizes after a 450 °C annealing of the carbonization procedure. The result shows the importance of adopting HMONpHMc as an intermediary core during the synthesis between so as to avoid the structural deformation of core materials during the high-temperature synthesis of MpMhMs.

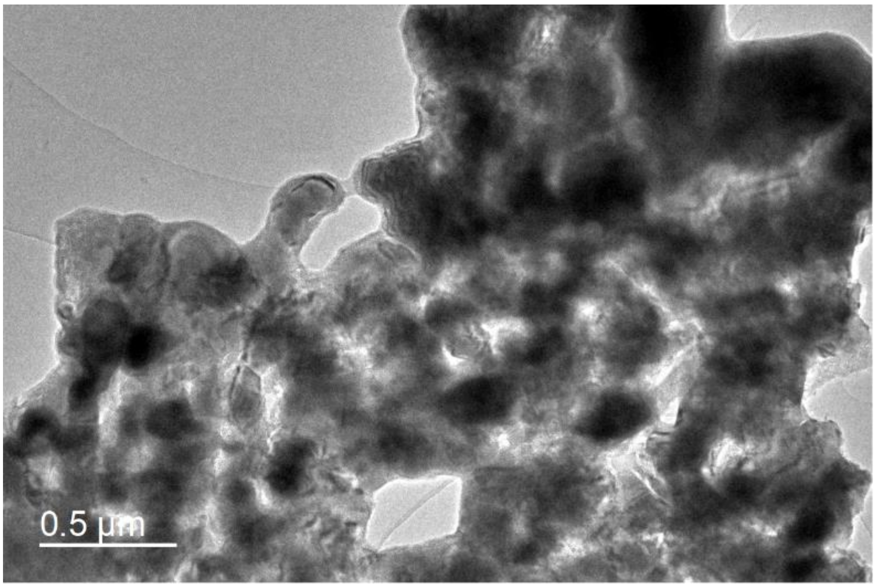

Fig. 4.4. Image of TEM for structural-deformed CTDMONpHMc after high-temperature carbonization.

4.3.2.3 Carbon Content Analysis

In Fig. 4.5, the MpMhMs Raman spectrum confirms the carbon formation. The peaks located at 1347 cm^{-1} and 1584 cm^{-1} corresponds to the disordered (D) band and graphitic (G) band, respectively [135]. While the D band is attributed to the structural defects, the G band is related to aromatic carbons in-plane vibrations in graphitic structure [136].

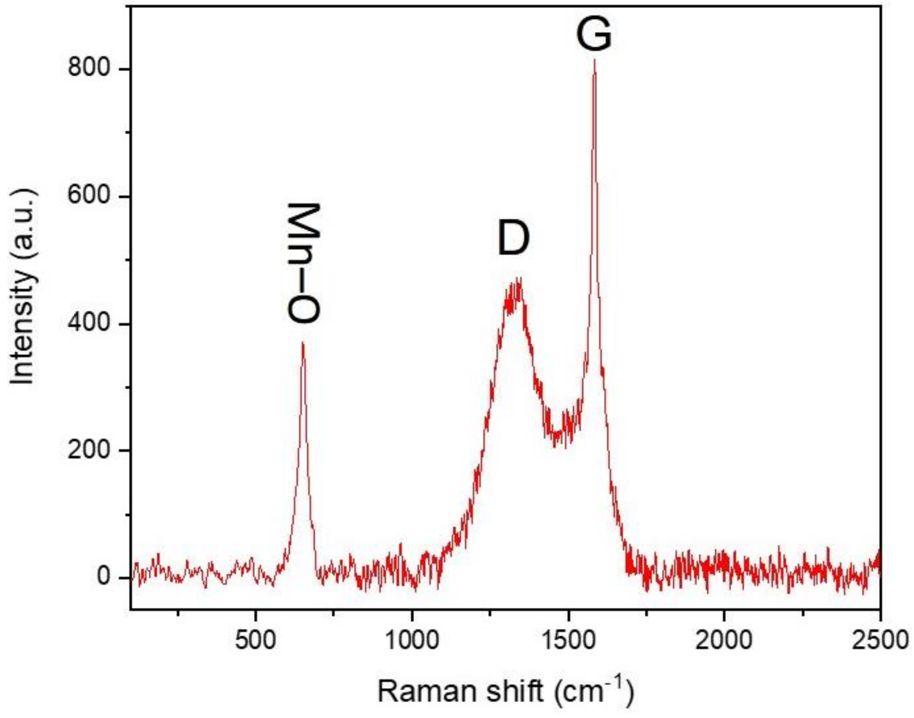

Fig. 4.5. Raman spectra of MpMhMs.

A way to investigate the graphitization degree is using the intensity ratio (I_D/I_G) as an indicator. A higher degree of disordered will show a higher ratio. The value of intensity ratio of MpMhMs is 0.58, which is comparatively lower than that of amorphous carbon black shown in Fig. 4.6 with the value of 1.19. The comparison implies that there are fewer defects with a higher graphitization degree, and there is a domination of sp^{2-} [137]. The carbon with higher graphitization corresponds to higher electrical conductivity [137], [138], which raises the electrochemical performance. Besides, there is a Raman shift at 650 cm^{-1} related to the Mn_3O_4 A_{1g} active mode. This active mode corresponds to the vibration of Mn–O bond stretching shared by edges or corners in the MnO_6 octahedral units [139], confirming the MpMhMs XRD results shown in Fig. 4.2 (b).

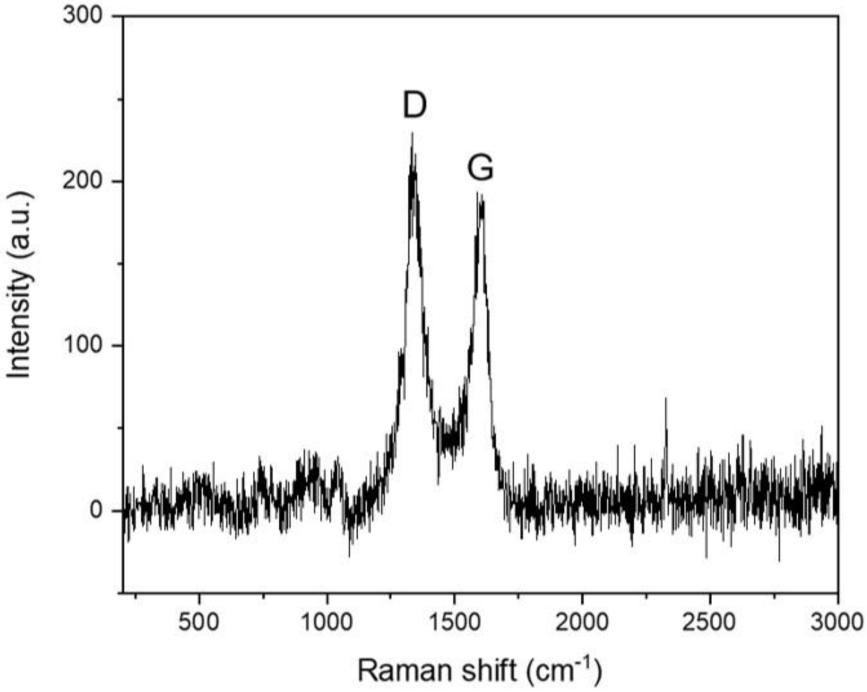

Fig. 4.6. Raman spectra of carbon black.

4.3.2.4 Surface Area and Porosimetry Analysis

In Fig. 4.7 (a), the HMONpHMc and MpMhMs BET surface areas are calculated from nitrogen adsorption and desorption isotherms. Using specification from IUPAC nomenclature, both HMONpHMc and MpMhMs show hysteresis loops following type IV, indicating both give a mesoporous structure [124]. The value of HMONpHMc and MpMhMs BET surface area are about 54.81 and 164.30 m^2/g, respectively. The higher BET surface area of MpMhMs suggests an enhancement of active surface sites by three times order after coating of carbon. Moreover, MpMhMs shows a higher pore volume with 0.308 m^3/g when comparing with 0.185 m^3/g of HMONpHMc. Fig. 4.7 (b) shows that the MpMhMs BJH pore size distribution shows a higher pore diameter than that of HMONpHMc in the 4 nm to10 nm range. The averagely smaller size of pores and larger volume of pores imply a comparatively higher impact on electrochemical performances, including initial discharge performance and cycling performance [125].

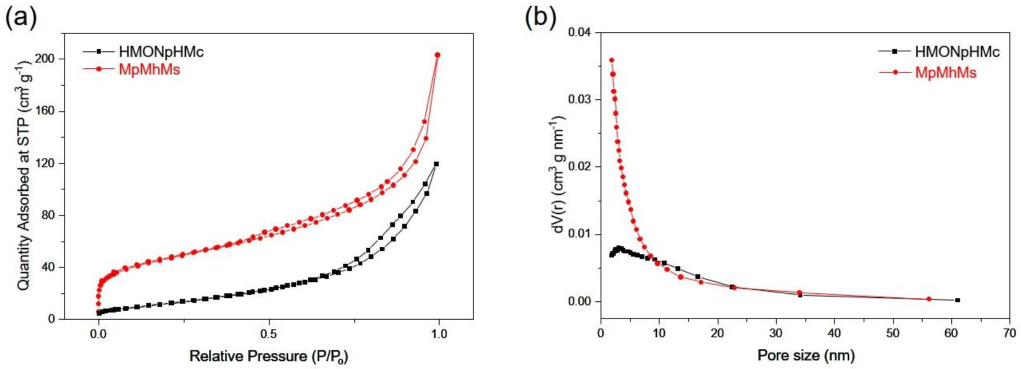

Fig. 4.7. (a) The N_2 adsorption/desorption isotherm; and (b) the pore size distribution for HMONpHMc and MpMhMs.

4.3.2.5 Thermogravimetric Analysis

In order to determine the content percentage of manganese oxide and carbon inside MpMhMs, thermogravimetric analysis (TGA) is used to approximate the mass loss of carbon by heating the MpMhMs sample [140] , [141].

Fig. 4.8 shows the TGA graph of MpMhMs. It shows that the weight of MpMhMs decreases greatly at the temperature range between 200 °C to 400 °C from 95.5 weight percentage to 75.4 weight percentage. The graph shows that MpMhMs contains about 75.4 weight percentage of manganese oxide and 20.1 weight percentage of carbon. The loss of 4.5 weight percentage gradual is caused by the moisture by pores and gas absorption [142].

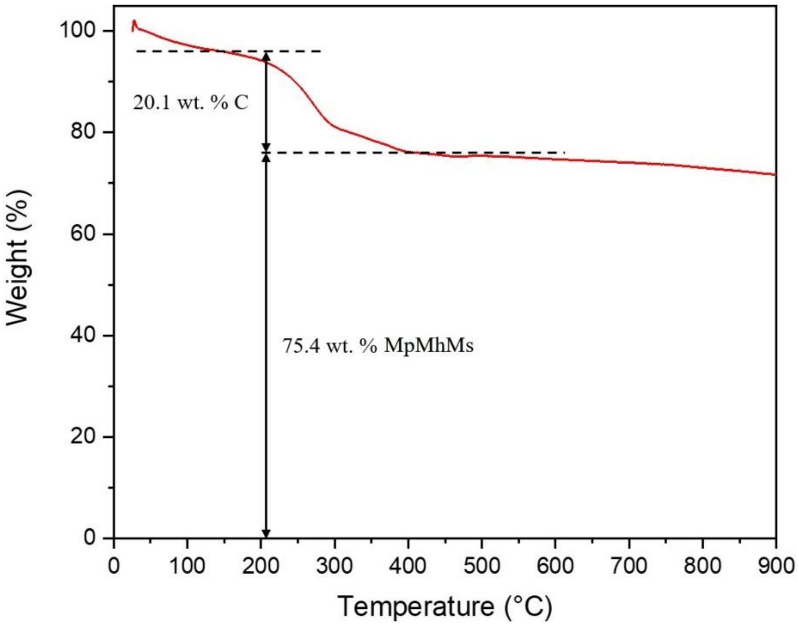

Fig. 4.8. TGA graph of MpMhMs.

4.4 Microspheres as Cathode and their Lithium–Oxygen Battery Cells

4.4.1 Materials

- MpMhMs and HMONpHMc prepared in Section 4.2.2 and Section 3.2.2, respectively
- Carbon black, Super P® (SP)
- Carboxymethyl cellulose (CMC)
- Lithium foil
- Glass fiber separator
- Carbon Paper (CP), cut in a circle shape with 16mm diameter
- Lithium bis(trifluoromethanesulfonimide) in tetra(ethylene glycol) dimethyl ether (LiTFSI in TEGDME)
- DI water

4.4.2 Preparation of Mn_3O_4@C Microspheres as Cathode

The preparations and procedures are the same as mentioned in Section 3.4.2. This time cathodes made of HMONpHMc was prepared as a comparison.

4.4.3 Fabrication of Lithium–Oxygen Battery Cells

The preparations and procedures are the same as mentioned in Section 3.4.4.

4.5 Electrochemical Characterizations

4.5.1 Characterization Methods

4.5.1.1 Galvanostatic Measurements

The characterization is the same as mentioned in Section 3.5.1.1.

4.5.1.2 Electrochemical Impedance Spectroscopy

The characterization is the same as mentioned in Section 3.5.1.2.

4.5.2 Result and Discussion

4.5.2.1 Discharge–Charge Characterization

Fig. 4.9 (a) shows the first discharge–charge curves of MpMhMs and HMONpHMc based cathodes for LOBs. MpMhMs demonstrates 3677 mAh/g first discharge specific capacity at 200 mA/g current density, which is much higher than that of 1070 mAh/g for HMONpHMc. Furthermore, the MpMhMs voltage discharge plateau is about 180 mV greater than the HMONpHMc voltage discharge plateau. Also, the MpMhMs voltage charge plateau is 170 mV lower when comparing with HMONpHMc. We can also observe that the voltage discharge plateau delivered by MpMhMs is flatter than that of HMONpHMc. Fig. 4.9 (b) reveals that the coating of carbon reduces the HMONpHMc overpotential throughout the potential range. At half of the upper-limit capacity, there is a reduction of OER overpotential from 1.15 V to 0.56 V at 250 mAh/g. Also, there is an ORR overpotential reduction from 0.34 to 0.28

V. From these evaluations, MpMhMs shows a higher capability for oxygen reduction during discharge and an enhanced Li_2O_2 decomposition efficiency during charge. It is proposed that the lower overpotential of MpMhMs is attributed to the excellent electric conductivity compared with HMONpHMc, which reduces the polarization [143].

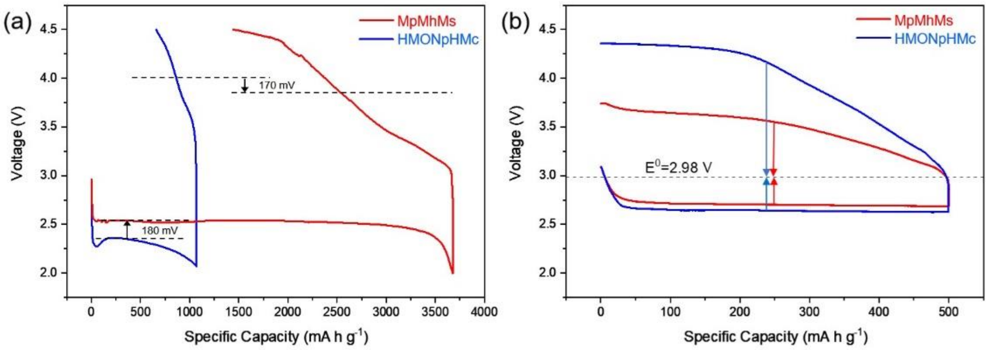

Fig. 4.9. The first discharge–charge curves of HMONpHMc and MpMhMs cathodes at a current density of 200 mA/g with (a) full capacity; and (b) an upper-limit capacity of 500 mAh/g.

4.5.2.2 Cyclic Characterization

For cyclic performance evaluation for LOBs, the discharge capacity is limited to 500 mAh/g so that decomposition of electrolyte could be avoided [126]. From Fig. 4.10 (a)–(d), we can observe that 66 cycles can be reversibly sustained at the upper limit capacity for the MpMhMs cathode while only 31 cycles can last for HMONpHMc cathode. From Fig. 4.10 (b), we can observe that there is some unstable charge potential during the first 20 cycles of HMONpHMc. The unstable potential can be caused by unstable electrolytes and not sufficient catalytic activity. Both cases result in an insulating side product accumulation on the surface of the cathode [83], [143]. By contrast, the improved MpMhMs cyclic stability can be provided by the material structure properties. First, the three times higher surface area contributes to higher electrocatalytic active sites. This can allow the Li_2O_2 side products to reduce faster and do not block the mesoporous structure. Second, MpMhMs possess a larger pore volume which enables the discharge products accommodation. Third, the carbon surface coating of MpMhMs protects the particles. The protection avoids material detachments from the cathode and also suppress the decomposition of electrolyte, resulting in enhanced stability for LOBs [125], [127], [144].

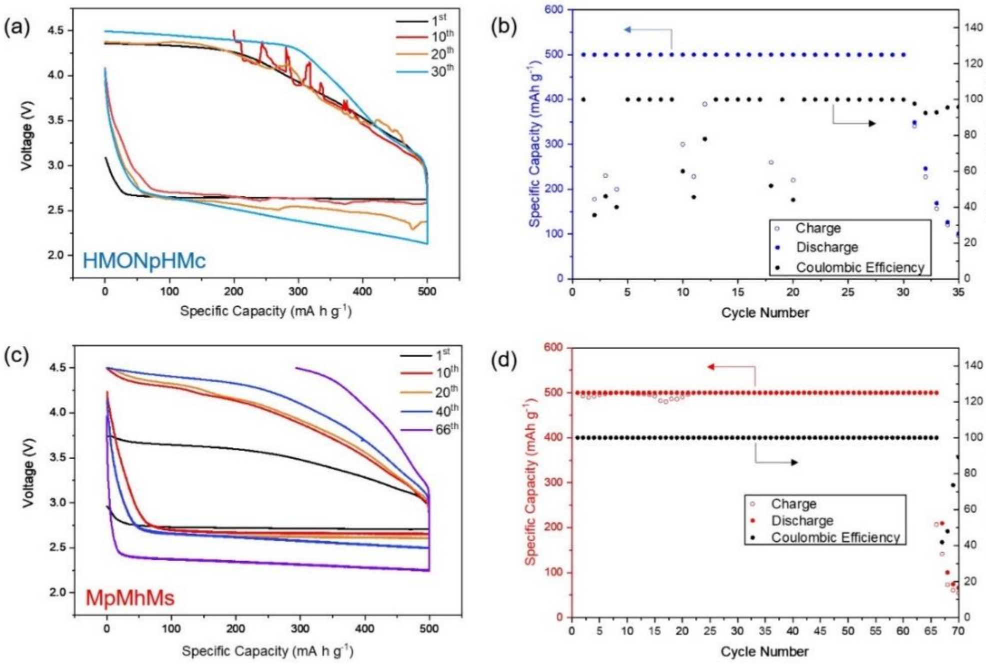

Fig. 4.10. The discharge/charge curves at different cycles for (a) HMONpHMc and (c) MpMhMs cathode-based LOBs. Cyclic performance with coulombic efficiencies for (b) HMONpHMc and (d) MpMhMs cathode-based LOBs. All LOBs discharge/charge data were obtained under the condition at 200 mA/g current with a 500 mAh/g upper limit capacity.

4.6 Proposed Oxygen Reduction Reaction/Oxygen Evolution Reaction Mechanisms

4.6.1 Cyclic Voltammetry

In order to observe the kinetics of ORR/OER during LOB discharge/charge, measurements of cyclic voltammetry are conducted. The CV curves of HMONpHMc and MpMhMs for the first cycle are shown in Fig. 4.11 (a) and Fig. 4.11 (b), respectively.

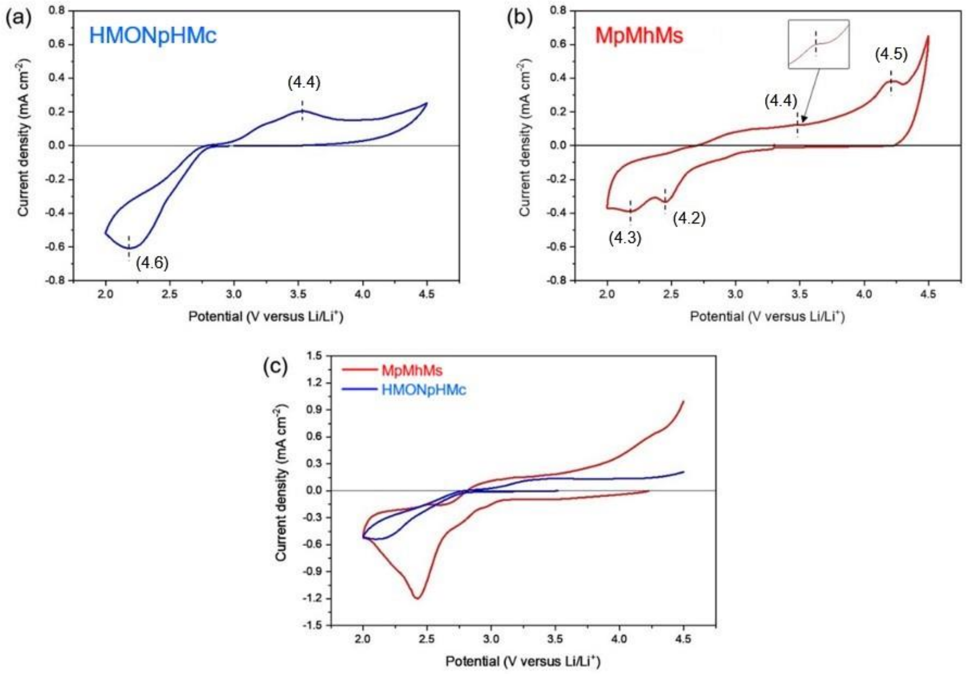

Fig. 4.11. The first cyclic voltammetry cycles for (a) HMONpHMc; and (b) MpMhMs; and (c) The third cyclic voltammetry cycles for HMONpHMc and MpMhMs.

In the negative direction potential scanning, we can indicate two ORR peaks located at 2.5 V and 2.2 V for MpMhMs. The initial peak is proposed to be the oxygen reduction process to superoxide [145]. Eq. (4.2) shows the corresponding chemical equations:

$$O_2 + e^- + Li^+ \rightarrow O_2^{-\bullet} + Li^+ \rightarrow LiO_2 \tag{4.2}$$

The second peak is attributed to the reduction further from superoxide to peroxide [146]. Eq. (4.3) shows the corresponding chemical equations:

$$LiO_2 + Li^+ + e^- \rightarrow Li_2O_2 \tag{4.3}$$

During the anodic scan, we can observe another two OER peaks located at 3.5 V and 4.2 V for MpMhMs. A magnified graph near the 3.5 V peak is enlarged in Fig. 4.11 (b) inset and Fig. 4.12. This peak shows the oxidation of lithium peroxide that decomposing into oxygen and lithium-ion, as shown in Eq. (4.4) [145]:

$$Li_2O_2 \rightarrow 2Li^+ + O_2 + 2e^- \tag{4.4}$$

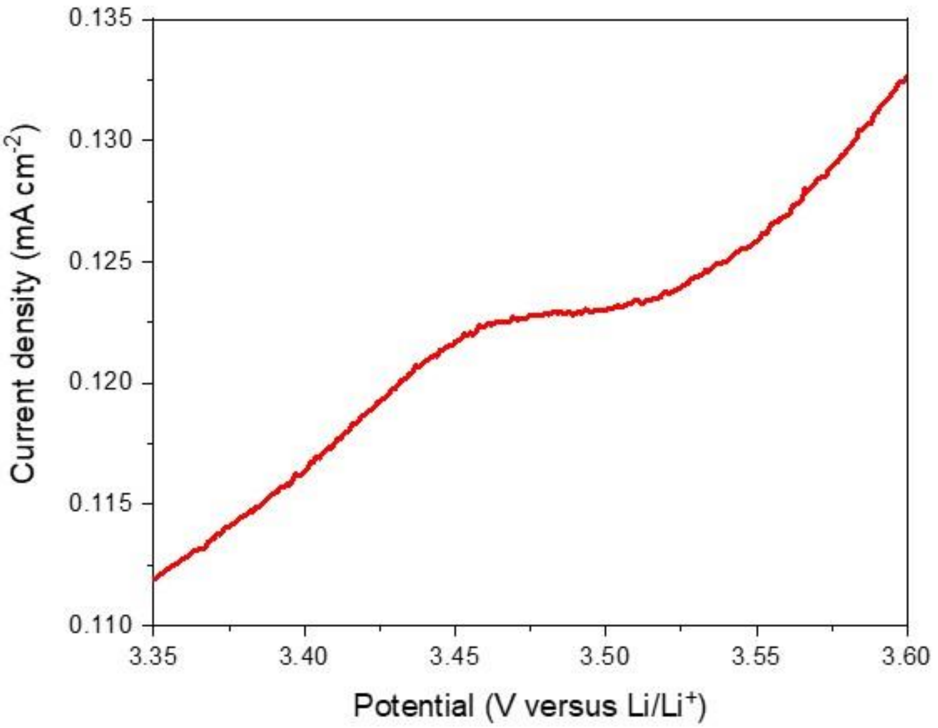

Fig. 4.12. The expanded region from 3.35 to 3.6 V of Fig. 4.11 (b) that showing the prominent peak corresponding to the lithium superoxide decomposition.

The peak at around 4.2 V is considered to be the reaction of lithium carbonate decomposition to carbon dioxide, according to Eq. (4.5) [128], [147]. A previous study suggested that the reaction of Eq. (4.5) initiates at above 3.8 V potentials. Furthermore, it was reported that an interesting catalytic activity of manganese oxide is shown for this lithium carbonate decomposition [148].

$$2Li_2O_3 \rightarrow 4Li^+ + 2CO_2 + 4e^- \; + O_2 \qquad (4.5)$$

For HMONpHMc, the distinct peaks at 2.25 V reflect the formation of lithium peroxide in Eq. (4.6), while the distinct peaks at 3.5 V reflect the decomposition in Eq. (4.4) of lithium peroxide, respectively [128]. All the peaks mentioned above are labelled on the related CV curves with corresponding chemical equations, as shown in Fig. 4.11 (a) and Fig. 4.11 (b).

$$2Li^+ + 2e^- + O_2 \rightarrow Li_2O_2 \qquad (4.6)$$

Because electrodes could go under activation for the first few cycles, we compare the electrochemical activities of MpMhMs and HMONpHMc by observing the third CV cycles, which is shown in Fig. 4.11 (c). We can observe that the MpMhMs current density is double of the HMONpHMc current density in the scanning of negative direction. The larger area for MpMhMs during CV comparing with the area of HMONpHMc implicit that the coating of carbon in MpMhMs could provide a higher electrochemical active surface area [129].

4.6.2 Nyquist Measurements

Before cycles, we examined the EIS spectra for both HMONpHMc and MpMhMs electrodes. The corresponding graph is shown in Fig. 4.13.

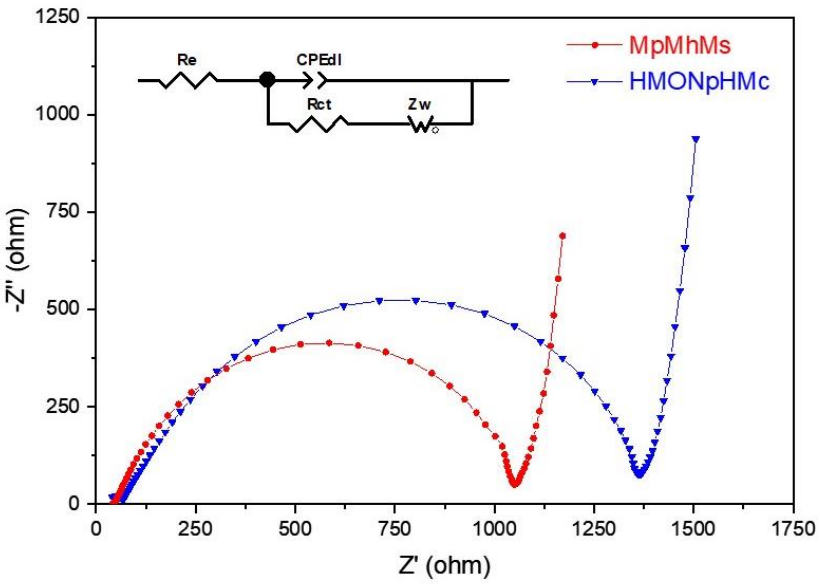

Fig. 4.13. EIS spectra of MpMhMs and HMONpHMc electrodes obtained before cycles. The equivalent circuit model is shown as an inset.

The impedance spectrum is fitted with an equivalent circuit model using Zview software, and the impedance values are listed in Table 4.1. The corresponding circuit is shown in the inset of Fig. 4.13. In the equivalent circuit model, R_e, R_{ct}, Z_w, CPE_{dl} refer to electrolyte ionic resistance, charge transfer resistance, diffusion resistance, and double-layer constant phase element, respectively.

Table 4.1. Impedance parameters calculated from the equivalent circuit for MpMhMs and HMONpHMc.

	MpMhMs	**HMONpHMc**
R_e/ Ω	48.6	86.6
R_{ct}/ Ω	990	1280
CPE_{dl}/ μF	13.0	45.1
Z_w/ Ω	72.3	140

From the fitting curves, we can observe a lower electrolyte ionic resistance (R_e) for MpMhMs when comparing with that of HMONpHMc. Moreover, MpMhMs shows a noticeable decrease in charge transfer resistance (R_{ct}). R_{ct} refers to the kinetic resistance reduction at the electrolyte/electrode interface [83], which is caused by its increased conductivity by the carbon coating [149]. Furthermore, the MpMhMs shows a comparatively lower diffusion resistance (Z_w) than that of HMONpHMc. This result implies faster transportation of Li^+ ions across the interface of MpMhMs and Li_2O_2. This result implies the dominant mass transport given by the MpMhMs electrode that decreases the overpotential and increases the ORR/OER kinetics [76].

4.6.3 Postmortem

To investigate the postmortem of MpMhMs cathodes, XRD and SEM were used to analyze the change of material structure and observe the morphology differences. After the first cycle, we observed the cathodes morphology changes through SEM images, as shown in Fig. 4.14. In Fig. 4.14 (c) and Fig. 4.14 (d), we discover a thick layer of discharge products after the first discharge, which covers the surface of MpMhMs. In Fig. 4.14 (e) and Fig. 4.14 (f), the discharge products disappear after the first charge.

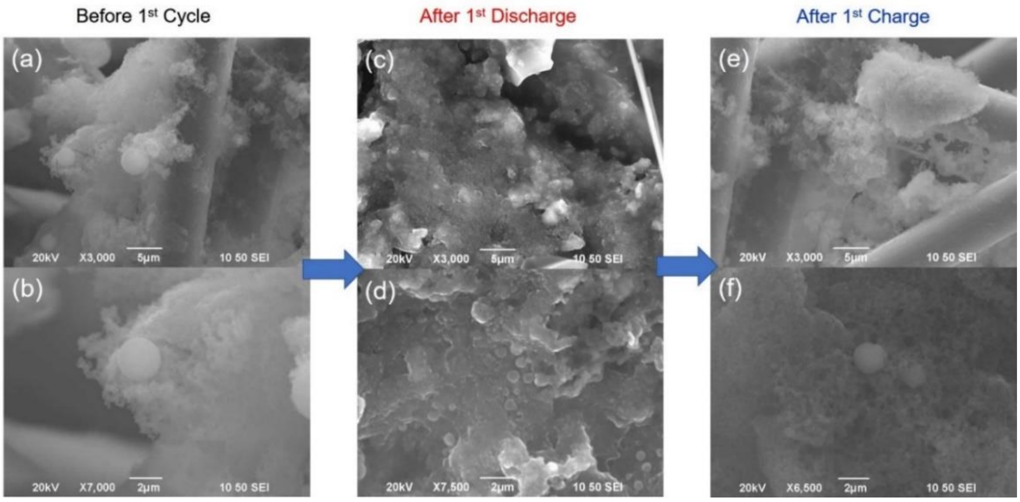

Fig. 4.14. The MpMhMs cathode images in SEM (a), (b) before the first cycle; (c), (d) after the first discharge; and (e), (f) after the first charge.

Fig. 4.15 (a) and Fig. 4.15 (b) reveal the morphology changes of MpMhMs cathodes after the 20th discharge and 20th charge, respectively. In Fig. 4.15 (a), we could observe the discharge products clogged the surface seriously after the 20th discharge. After the 20th charge, the cathode could still be recovered without finding obvious discharge products. This shows that the appearance and disappearance of discharge products typically occurred and the reversibility of MpMhMs cathodes is high.

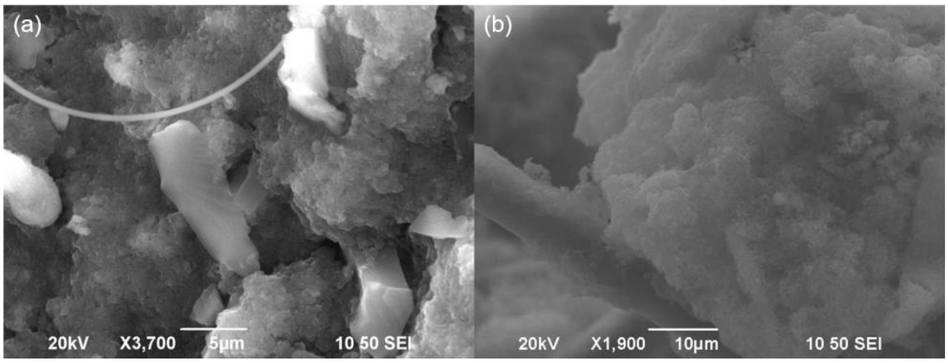

Fig. 4.15. The MpMhMs cathode images in SEM (a) after the 20th discharge; and (b) after the 20th charge.

In order to investigate the discharge products formation, we examined the cathodes by XRD analysis in three different timing, including cathode before the cycle, cathode after the first discharge, and cathode after the first charge. The corresponding XRD graphs are shown in Fig. 4.16 and Fig. 4.17. After the first discharge, we can observe characteristic peaks located at 33°, 35°, 40.5°, and 58.6°. These peaks are related with the (100), (101), (102), and (110) planes of Li_2O_2 with JCPDS number of 09-0335, respectively [150]. The characteristic peaks located at 26°, 44°, and 54° could refer to the (002), (10*l*), and (112) planes of carbon black, where $l = 0$ or 1 [151]. These carbon peaks are contributed by the carbon paper and Super P used during cathode fabrication. The nearly unchanged peaks after discharge/charge show that carbon black did not involve in the reaction. On the other hand, there are no obvious characteristic peaks of Li_2CO_3 with JCPDS number 87-0729 that can be discovered at 23.5° and 29.4° [152]. After the first charge, characteristic peaks of Li_2O_2 peaks vanish. The vanish of peaks indicates the complete decomposition of Li_2O_2 discharge products, which is contributed by the high electrocatalytic activities of MpMhMs cathode with outstanding reversible stability. The results above are consistent with the discharge products appearing and vanishing on the surface of MpMhMs from SEM images shown in Fig. 4.14 and proposed chemical equations suggested in Eq. (4.2)–(4.4) from Section 4.6.1.

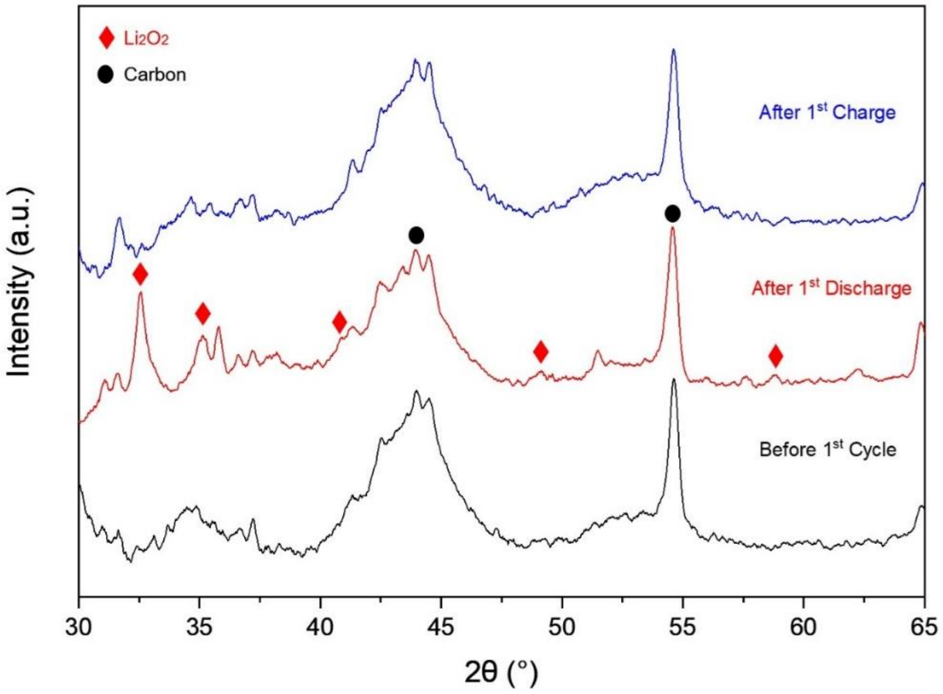

Fig. 4.16. The MpMhMs cathode XRD patterns from 30° to 65° before the cycle, after the first discharge, and after the first charge.

The difference between chemical equation based on CV in Eq. (4.6) and XRD measurement result for Li_2CO_3 could be resulted by the carbon paper interference as it is the source of the carbon peak with extremely high intensity in the range between 23° to 30°, which is shown in Fig. 4.17. This extreme high intensity results in the comparatively unobvious Li_2CO_3 peaks.

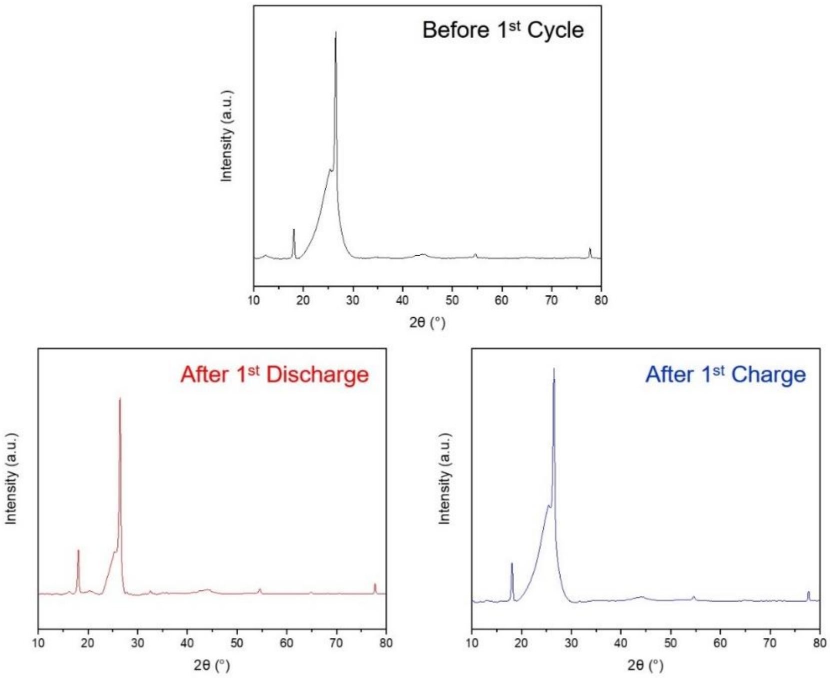

Fig. 4.17. The MpMhMs cathode XRD patterns from 10° to 80° before the cycle, after the first discharge, and after the first charge.

4.7 Summary

In this chapter, thin carbon shells with a thickness of a few nm are generated onto the surface of HMONpHMc mentioned in chapter 3 resulted in multicore@shell Mn_3O_4@C mesoporous multi-hollow microsphere (MpMhMs). In this structure, Mn_3O_4 nanoparticle-assembled hollow sphere acts as the core while spongy carbon layers act as the shell. The facile use of HMONpHMc with MnO_2/Mn_2O_3 hybrid manganese oxide as the intermediary core during the synthesis between instead of directly using Mn_3O_4 avoids structural deformation of core materials during the high-temperature synthesis of MpMhMs. This material with rational designs has then been used as an improved catalytic cathode electrocatalyst for LOBs and compared with HMONpHMc counterpart physically and electrochemically. The MpMhMs-based cathodes have shown increased electrochemical performances. Table 4.2 summarizes and compares the experimental results between MpMhMs, HMONpHMc, and CTDMONpHMc based LOBs.

Table 4.2. Comparison of experimental results for MpMhMs, HMONpHMc, and CTDMONpHMc based LOBs.

	MpMhMs	**HMONpHMc**	**CTDMONpHMc**
Physicochemical Evaluations			
Material Constitutions	Mn_3O_4 and carbon	Mixed phase MnO_2/Mn_2O_3	Mn_3O_4
Diameter of Hollow cages	~600nm	~600nm	500–1000nm
BET Surface Area	164.30 m^2/g	54.81 m^2/g	90.65 m^2/g
Pore Volume	0.308 m^3/g	0.185 m^3/g	7.7×10^{-8} m^3/g
Electrochemical Characterizations			
First Discharge Capacity	3677 mAh/g	1070 mAh/g	712 mAh/g
Discharge Voltage Plateau	2.48 V	2.30 V	2.22 V
Cycle numbers	66	31	18
Charge Transfer Resistance (R_{ct})	990 Ω	1280 Ω	2023 Ω

From the table, MpMhMs based LOB cells demonstrate two times higher first discharge capacity and a longer cyclability when comparing with that of HMONpHMc. The physiochemical characterizations and EIS spectra have both provided the reasons for the enhanced electrochemical performances by introducing the carbon shells, including larger pore volume, higher surface area, higher electrical conductivity, extra protection of surface which resists material pulverization, and reduced charge transfer resistance and diffusion resistance. Furthermore, the postmortem studies have demonstrated the successful discharge products decomposition during charge, which has revealed the excellent catalytic activity and highly reversible stability of MpMhMs. These results have featured the crucial role of adopting carbon shell as supplements. The carbon shell surpasses transition metal-oxide electrocatalysts for a wide range of catalytic applications, including electromagnetic absorption, supercapacitors, and LOBs.

Chapter 5 Density Functional Theory for Lithium–Oxygen Batteries

5.1 Introduction

Nowadays, scientific computation plays a critical role in materials science, experiment, and engineering applications. Taking advantage of enhanced computing power, basic theory advancement, and new algorithms support, materials properties, including physical and chemical, can be directly predicted by adopting quantum mechanics law for electrons now. This successfully provides a great deal of support for solving difficult questions in materials science, chemistry, and physics. For nano-scale materials, theoretical atomistic simulations are often used by theorists and experimentalists to predict specific properties for new materials and explain some phenomena observed during an experiment by using computer stimulations.

In this chapter, we adopt density functional theory (DFT), a powerful theoretical simulation tool, to explain the electrochemical performances of MpMhMs and HMONpHMc based LOBs observed in chapter 4 on atomic scale. DFT has facilitated computational material science. It can be applied to design specific materials with desired properties for a wide range of applications. Moreover, it can be applied to gain a better insight into reaction mechanisms and the materials fundamental properties. Some background information on DFT is described briefly in the following sections.

5.1.1 Density Functional Theory

DFT applies and reformulates Schrödinger equation. It is a method to study the electronic structure of interested molecules or atoms on an atomistic scale. Thomas and Fermi stated that the DFT principle considers any properties from many-body systems by a ground state density function in 1927 [153]. After that, different functions for approximation were proposed based on the many-body Schrödinger equation, including Thomas-Fermi-Dirac approximation [154]. Nevertheless, most of the models proposed at that period were rough. Many essential physics and chemistry parameters were also neglected, such as the binding of molecules and atoms shell structures [155].

After nearly forty years, modern DFT theoretical basics were developed by Hohenberg and Kohn in 1964 [156]. Two basic theorems were proved. The first theorem states that all system properties can be fully determined by only a given ground state particle density. The second theorem state that the value of the global minimum of any particular external potential ($V_{ext}(\mathbf{r})$) function represents the energy of the ground state for that corresponding system. In 1965, a practical approach, called the Kohn-Shan approach, was proposed to calculate the many-body system properties by using simpler independent auxiliary particle problems instead of previously hard-to-solve interacting many-body systems [157]. Two assumptions are proposed for this approach. The first one assumes that the density of the ground state in non-interacting particles auxiliary system can determine the exact ground-state density. The second assumes an effective local potential at point **r** acting on an electron, and the usual kinetic operator is used to choose the auxiliary Hamiltonian. After making these assumptions for the non-interacting system, independent particle equations could become greatly soluble. The corresponding Kohn-Shan equation of a many-electrons system is expressed in Eq. (5.1) for the ground state energy:

$$E_{gs} = E_{11} + \int d\boldsymbol{r} V_{ext}(\boldsymbol{r}) n(\boldsymbol{r}) + T_S[n] + E_H[n] + E_{xc}[n] \tag{5.1}$$

, whereE_{11}refers to the interaction between nuclei. $V_{ext}(\boldsymbol{r})$ refers to the external potential attributed to external fields and nuclei. $n(\boldsymbol{r})$ is the density for the non-interacting system. $T_S[n]$ refers to particle kinetic energy, which can be expressed in terms of a function orbitals. $E_H[n]$ refers to the Hartree or simply Coulomb energy. Finally, $E_{xc}[n]$ refers to the exchange correlation. All the terms in the equation are well defined except for $E_{xc}[n]$, which is the only unknown term with corresponding unknown energy expression. Some reasonable approximations are required for enabling the execution of the whole equation computationally. $E_{xc}[n]$ can be defined by using the expression shown in Eq. (5.2):

$$E_{xc}[n] = \int d\boldsymbol{r}\, n(\boldsymbol{r})\, \varepsilon_{xc}([n], \boldsymbol{r}) \tag{5.2}$$

, where $\varepsilon_{xc}([n], \boldsymbol{r})$ refers to the energy for one electron at point **r**. This value can be determined from the density n (**r**,σ) for some point **r** neighborhood.

Kohn-Sham equation successfully contributes practical approximations for the prediction role of "first principles" for material properties. The corresponding DFT accuracy is highly dependent on the exchange correlation approximations in the equation, which corresponding to $E_{xc}[n]$ mentioned in Eq. (5.1). Therefore, practical approximation of functionals is required for estimation for achieving high accuracy.

5.1.2 Generalized Gradient Approximation

In order to improve the accuracy of DFT calculations, different approximations were made for exchange correlation. The first popular approximation for this is local density approximation (LDA) [158]. In this approach, we simply consider inhomogeneous electron systems as homogeneous electron gas. Nevertheless, this approach over-binds solids and molecules and cannot predict electron-rich system even it can describe lots of homogeneous systems.

To alleviate the drawback of LDA, generalized gradient approximations (GGAs) can be carried out [159], [160]. This approximation deals with the inhomogeneous electron density by considering the magnitude of the electron density gradient. Perdew, Burke and Enzerhof (PBE), Perdew and Wang (PW91) , and Becke (B88) are the 3 forms that are widely used for GGA. These forms correct the over-binding problem of LDA, giving comparatively acceptable results when compared with the actual experiments.

To sum up, we can realize that the DFT accuracy is determined by the functionals of exchange correlation. In reality, it is very hard to calculate the exact value of this correlation, so an approximation should be made. While LDA is the first famous approximation, it is not suggested to use this approximation in chemistry. On the other hand, PBE is the most widely used form for GGA functionals because the calculation speed is fast, and the accuracy is satisfactory. Therefore, we choose this functional in our following analysis.

Based on the first-principles calculations, DFT is applied to support the longer cyclic performance and the higher ORR catalytic activities for the MpMhMs based LOB mentioned in chapter 4 compared to that of HMONpHMc.

5.2 Theoretical Evaluations

5.2.1 Evaluation Methods

We performed all of the first principle calculations by adopting spin-polarized density functional theory (DFT) as previously implemented in Quantum Espresso [161], [162]. We selected the form of Perdew-Burke-Ernzerhof (PBE) functional for generalized gradient approximation (GGA) analysis for describing the interaction of exchange-correlation [163]. We considered Van de Waals (vdW) interactions using Grimme's DFT-D3 method [164]. A 550 Ry density cutoff with a 55 Ry plane-wave cutoff were used. The parameters were based on solid-state pseudopotentials in standard following with projector augmented-wave (PAW) method [165], [166]. We constructed a (0 0 1) Mn_3O_4 slab with five layers and a sufficient 20 Å vacuum slab. We set the Monkhorst-Pack k-point as 3 × 3 × 1 to sample the Brillouin zone. All atoms in the model were relaxed so that the forces on each atom were smaller than 0.02 eV/Å. For the purpose of evaluating the discharge products binding energies for both MpMhMs and HMONpHMc so as to verify the corresponding LOB relative capacities, we determined the Li_2O_2, LiO_2 and Li adsorption energies on the surface by using Eq. (5.3).

$$E_{ad} = E_{Total} - E_{Surface} - xE_{Li} - \frac{y}{2E_{O_2}} \tag{5.3}$$

, where E_{Total} refers to the adsorption system total energy. E_{Surface} refers to surface energy. $E_{\text{O}_2/Li}$ refers to the energy of triple-stated oxygen molecule or lithium in bulk metal state, which is used to eliminate the problem of over-binding. x and y refer to the number of lithium and oxygen atoms in Li_xO_y.

5.2.2 Results and Discussion

5.2.2.1 Binding Energies

For studying the initial ORR mechanism, the binding energies are examined between reactive species (Li_2O_2, $^*LiO_2$, and $^*O_2$) and the electrode materials by using DFT analysis [167]. In the LOB discharge process, ($+O_2 \rightarrow +Li \rightarrow +Li$) is one of the possible paths for the formation of Li_2O_2. Firstly, the reaction starts with the oxygen molecule adsorption on the surface. Secondly, the lithium-ion is absorbed at the cathode surface, forming lithium superoxide. Finally, lithium superoxide transforms to lithium peroxide *via* further disproportionation or electro-reduction [152], [168], [169]. According to our calculations, the (100) plane is discovered to possess the lowest Mn_3O_4 relative surface energy, indicating (100) plane is the most stable plane of surfaces. The corresponding relative surface energies are compared as shown in Table 5.1.

Table 5.1. The Mn_3O_4 slab relative surface energy. This energy was defined by equation $\gamma = (E_{slab} - NE_{bulk})/2A$, in here E_{bulk}, E_{slab}, A, and N represents the bulk energy per atom, the surface slab total energy we obtained by density functional theory, the area of surface, and the atoms number in the surface slab, respectively.

	(001)	**(010)**	**(100)**
γ	-0.07553	-0.13598	-0.13598

Hence, we choose the (100) plane for analyzing the binding energies. Before the stimulation started, we optimize the HMONpHMc with 5.762 Å lattice constant and fourteen atoms per primitive cell. After that, we add carbon atoms onto the surface with (100) plane following with the optimization again for forming MpMhMs.

In Fig. 5.1, different steps for reaction free energies are shown according to the previously mentioned ORR path for HMONpHMc and MpMhMs. In step (1), The greatly higher O_2 adsorption energy of MpMhMs with -3.94 eV compared with that of HMONpHMc with -0.45 eV shows that MpMhMs gives a better surface affinity to oxygen gas, thus resulting in an enhanced ORR catalytic activity. In step (2), the stronger lithium superoxide adsorption energy after lithium is added for MpMhMs with -7.40 eV than that of HMONpHMc with -6.42 eV further evaluates the enhanced ORR catalytic activity for the MpMhMs electrode. Regarding the final step (3), the stronger adsorption energy of lithium peroxide on MpMhMs with -10.0 eV comparing with that of HMONpHMc with -7.27 eV results in increased discharge capacity. The theoretical calculations above can successfully support the experimental results shown in Fig. 4.10 that a longer cyclic performance of MpMhMs can be delivered with an enhanced ORR catalytic activity.

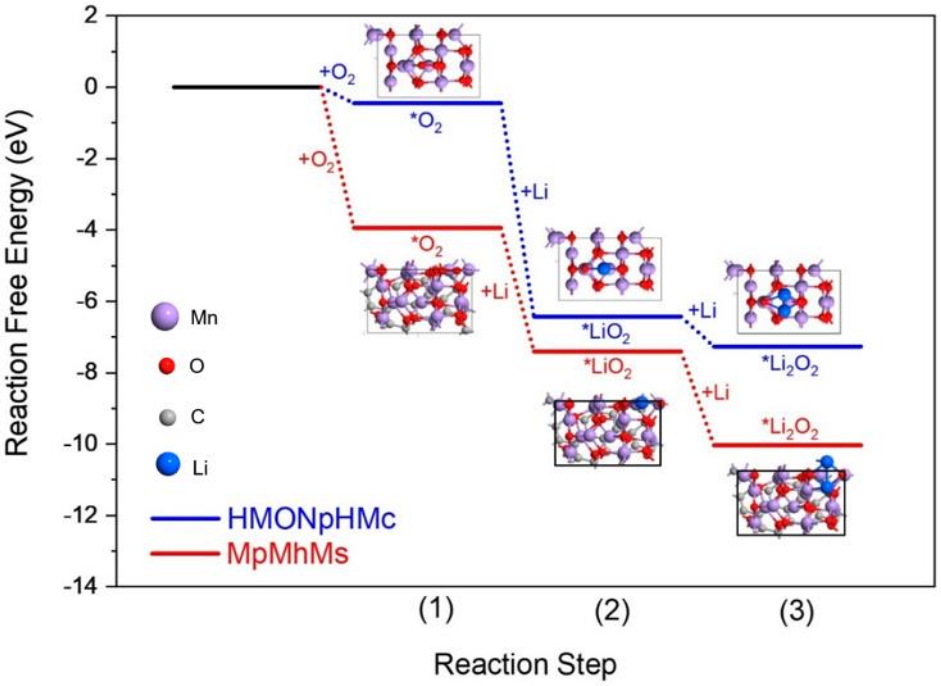

Fig. 5.1. The reaction free energies for the formation of Li_2O_2 on HMONpHMc and MpMhMs surfaces referring to the path of (+O_2→+Li→+Li). The asterisks(*) in the figure stands for the surface adsorbed species.

5.2.2.2 Partial Density of States

Density of states (DOS) refer to the number of states available for electrons to occupy at each energy level in solid state physics while partial electronic densities of states (PDOS) show the relative contribution for a particular atom to the DOS total. DOS and PDOS can be used to describe material characteristics such as electrical properties [152]. Under an external magnetic field, the position of the nuclear spin axis could be parallel or antiparallel with the magnetic field direction, causing spinning states. Scientists describe the spin by using spin quantum number, while spin quantum number equals +1/2 for parallel (spin up) and -1/2 for antiparallel (spin down) case. In a PDOS graph, the PDOS above x-axis refers to the spin up case and the PDOS below x-axis refers to the spin down case. Spin splitting of energy band states, also called spin polarization, gives rise to magnetic moments in an itinerant model of electronic structure [170]. These moments arise because more occupied spin-up states exist when comparing with the spin-down states [170]. In a PDOS graph, we can observe the degree of reflection symmetry along x-axis to know if there are any spin splitting occur. The PDOS curves that are less symmetrical along x-axis refers to a more obvious spin splitting of energy band states.

In order to gain a better insight into the increased ORR catalytic performance for MpMhMs based cathodes in LOB, the PDOS of surface are examined, and the corresponding graphs are shown in Fig. 5.2. We can notice that the Mn atom 3d orbital on MpMhMs surface reveal very obvious spin splitting states near the Fermi level. The result is completely different from that of HMONpHMc, which shows a symmetrical curve along the x-axis near the Fermi level. This higher spinning states is attributed to the redistribution of interfacial electron between the C atom layers and Mn_3O_4. On account of the orbitals near the Fermi level, the MpMhMs surface is more active for accepting or donating electrons from reactive species (Li_2O_2, $*LiO_2$, and $*O_2$) when the catalytic reaction is processing when comparing with that of HMONpHMc [171]. Therefore, the surface of MpMhMs demonstrates a much higher affinity for all reactive species, which could lead to enhancement of catalytic activity for cyclic of the LOB.

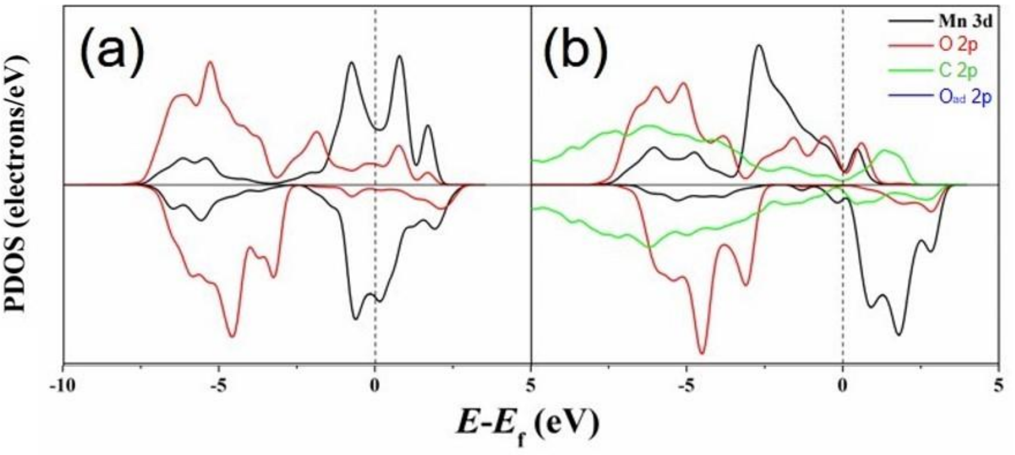

Fig. 5.2. PDOS for (a) HMONpHMc and (b) MpMhMs surface. The Fermi level is indicated by the dashed line.

5.3 Summary

In atomistic scale, we compute the DFT calculations for the purpose of supporting the LOB electrochemical results in chapter 4. GGA functionals with PBE form are applied for this analysis for the functionals of exchange correlation approximation because of speed and accuracy reasons. For studying the initial ORR mechanism, the binding energies between the reactive species and cathode materials are examined. The higher adsorption energy for all reactive species on the (110) surface of MpMhMs than implies a better ORR activity, which matches the experimental results with enhanced discharge capacity. The PDOS of MpMhMs shows an obvious spin-splitting for Mn atom 3d orbital around Fermi-level. The result demonstrates the underlying reason for MpMhMs cathodes having a better catalytic activity for LOB cyclic.

Chapter 6 Conclusions and Suggestions for Future Work

6.1 Conclusions

In this work, facile interesting core@shell-structured nanomaterials (CSNs) has been developed successfully for lithium-based batteries applications, including lithium-ion batteries (LIBs) and lithium–oxygen batteries (LOBs). Corresponding physicochemical evaluations and electrochemical characterizations have been performed to demonstrate and compare the efficiency between CSNs for the batteries. Models have also been established to reveal the underlying reaction mechanisms and compared with the experimental results.

For LIBs, a facile in-situ one-pot arc-discharge method has been adopted for synthesizing $FeSn_2$@C nanocapsules CSNs. This method has confined the crystal size and combined the advantages with onion-like carbon shells, which finally exhibit enhanced electrocatalytic properties. This method stands out from another existing method for synthesizing CSNs with similar material structure and constitution because of two major reasons: the introduction of intermetallic stannide alloy combining with conductive onion-like carbon shell successfully overcome most of the important problem faced in LIBs, such as volume changes during lithiation and delithiation process; and one-step-only synthesis with high freedom to control material phase and structure.

For LOBs, mixed-phase MnO_2/Mn_2O_3 hybrid manganese oxide nanoparticle hollow microcages (HMONpHMc) have been synthesized firstly. In this structure, round-shaped Mn_3O_4 nanoparticles acting as building blocks forms the hollow-microcages with around 0.6 μm diameter. Comparing HMONpHMc with the state-of-the-art sacrificial carbon template method during core synthesis, this method is simplified as a template-free method, providing an alternative that saving synthesis time with the reduction of material loss. The HMONpHMc-based cathodes have also shown enhanced electrochemical performances in both first discharge capacity and cyclability, which contributed to its larger pore volume and comparatively high surface conductivity from the specific balance of mixed-phases. However, the electric conductivity still has rooms for improvement, and the insufficient surface area does not benefit LOB catalytic activities.

Mesoporous multi-hollow core@shell-structured manganese oxide@carbon (Mn_3O_4@C) microspheres, derived from HMONpHMc, have been synthesized. In this rationally designed structure, round-shaped Mn_3O_4 nanoparticles acting as building blocks forms hollow-microcages at the core, while graphitic layers forms outside as the shell. The use of HMONpHMc mixed-phase hybrid core as an intermediary during synthesis has prevented structural deformation of the core during high-temperature synthesis. Physical properties and electrochemical performances have been examined for MpMhMs-based cathode in LOB and compared with that of the HMONpHMc counterpart. The MpMhMs-based LOB have showed increased electrochemical performances such as longer cyclability with higher first discharge capacity. The benefits of introducing the carbon shells have been suggested by EIS spectra and physiochemical characterizations, which includes increased electrical conductivity, larger surface area and pore volume, reduced diffusion resistance, and possessing pulverization resistance provided by extra surface protection. In addition, the investigation of postmortem has demonstrated the excellent catalytic activity and high reversible stability of MpMhMs.

In atomistic scale, theoretical DFT calculations have further supported the ORR catalytic activity enhancement of MpMhMs with better cycling performance. Both the reaction free energies calculation and partial electronic densities of states have shown the higher affinity of MpMhMs to reactive species, implying a better catalytic activity. The results have highlighted the carbon shell role as an important supplement to surpass CSNs electrocatalysts for applications in LIBs and LOBs.

6.2 Suggestions for Future Work

First, further size, constitution, and morphology control can be applied during the synthesis of CSN. The corresponding physical properties and electrochemical performances for LOBs can be evaluated. For example, the annealing time and conditions for HMONpHMc synthesis highly affect the final phase of manganese oxides. The corresponding XRD summary is shown in Table 6.1. Suitable materials can be chosen for further synthesizing different new CSN materials.

Table 6.1. Summary of the manganese oxide material context with different heating time and condition.

Condition/ Heating Time	2 hours	4 hours	8 hours
With tube blocks	Both Mn_2O_3 and Mn_3O_4 peaks	Strong Mn_2O_3 peaks with weak Mn_3O_4 peaks	Strong Mn_2O_3 peaks with weak Mn_3O_4 peaks
Without tube blocks	Mn_3O_4 peaks only	Strong Mn_3O_4 peaks with weak Mn_2O_3 peaks	Mn_2O_3 peaks only

Next, the thickness of carbon shells in MpMhMs can be tactfully tuned by the amount of glucose used and the annealing time control. The tuning can directly affect the corresponding LOB performance as the thicknesses of carbon influence the electroconductivity of materials and ORR–OER facilitation against discharge product

Li_2O_2 passivation. Too few carbon sources used or too long annealing time may fail to deliver any carbon shell, while very thick carbon shell fails to give satisfactory LOB performance results.

On the other hand, the synthesis method for CSNs can be applied to other transition metal oxides (TMOs) for LIB and LOB applications. For example, the usage of mixed-phase oxides hybrid as an intermediary core for constructing core@shell structure can be applied to other TMOs such as Co and Ni oxides, as they also possess multiple stable oxidation states with very different physical properties.

Finally, as the results have highlighted crucial supplement for carbon shell so as to enhance the catalytic performance of TMO nano-structured electrocatalysts, we could apply a similar concept to a wide range of applications, such as fuel cells, supercapacitors, and electromagnetic absorption.

List of References

[1] M. R. Palacín, “Recent advances in rechargeable battery materials: a chemist’s perspective,” *Chemical Society Reviews*, vol. 38, no. 9, pp. 2565–2575, 2009.

[2] L. Zhang, G. Zhang, H. B. Wu, L. Yu, and X. W. Lou, “Hierarchical tubular structures constructed by carbon-coated SnO_2 nanoplates for highly reversible lithium storage,” *Advanced Materials*, vol. 25, no. 18, pp. 2589–2593, 2013.

[3] L. Shao, J. Jeon, and J. L. Lutkenhaus, “Polyaniline/vanadium pentoxide layer-by-layer electrodes for energy storage,” *Chemistry of Materials*, vol. 24, no. 1, pp. 181–189, 2012.

[4] P. J. Hall and E. J. Bain, “Energy-storage technologies and electricity generation,” *Energy Policy*, vol. 36, no. 12, pp. 4352–4355, 2008.

[5] M. Winter and S. Passerini, “Lithium ion batteries as key component for energy storage in automotive and stationary applications,” *2011 IEEE 33rd International Telecommunications Energy Conference (INTELEC)*, 2011, pp. 1–3, doi: 10.1109/INTLEC.2011.6099839.

[6] Q. Xiao, Q. Zhang, Y. Fan, X. Wang, and R. A. Susantyoko, “Soft silicon anodes for lithium ion batteries,” *Energy & Environmental Science*, vol. 7, no. 7, pp. 2261–2268, 2014.

[7] H. Lee, M. Yanilmaz, O. Toprakci, K. Fu, and X. Zhang, “A review of recent developments in membrane separators for rechargeable lithium-ion batteries,” *Energy & Environmental Science*, vol. 7, no. 12, pp. 3857–3886, 2014.

[8] X. Fu and W. Zhong, “Biomaterials for high-energy lithium-based batteries: Strategies, challenges, and perspectives,” *Advanced Energy Materials*, vol. 9, no. 40, article 1901774, 2019.

[9] N. Mahmood and Y. Hou, “Electrode nanostructures in lithium-based batteries,” *Advanced Science*, vol. 1, no. 1, article 1400012, 2014.

[10] K. R. Bullock, *Batteries for sustainability*, New York: Springer, 2013, pp. 117–134.

[11] S. Petrovic, *Battery technology crash course*, Switzerland: Springer International Publishing, 2021, pp. 73–88.

[12] J. J. G. Willems and K. H. J. Buschow, “From permanent magnets to rechargeable hydride electrodes,” *Journal of the Less Common Metals*, vol. 129, pp. 13–30, 1987.

[13] T. Nagaura and K. Tozawa, “Lithium-ion rechargeable battery,” *Progress in batteries and solar cells*, vol. 9, pp. 209–212, 1990.

[14] X. Ji, K. T. Lee, and L. F. Nazar, “A highly ordered nanostructured carbon–sulphur

cathode for lithium–sulphur batteries," *Nature Materials*, vol. 8, no. 6, pp. 500–506, 2009.

[15] G. Girishkumar, B. McCloskey, A. C. Luntz, S. Swanson, and W. Wilcke, "Lithium−air battery: promise and challenges," *The Journal of Physical Chemistry Letters*, vol. 1, no. 14, pp. 2193–2203, 2010.

[16] C. Buzea, I. I. Pacheco, and K. Robbie, "Nanomaterials and nanoparticles: sources and toxicity," *Biointerphases*, vol. 2, no. 4, pp. MR17–MR71, 2007.

[17] P. Simon, Y. Gogotsi, and B. Dunn, "Where do batteries end and supercapacitors begin?," *Science*, vol. 343, no. 6176, pp. 1210–1211, 2014.

[18] V. V. Srdic, B. Mojic, M. Nikolic, and S. Ognjanovic, "Recent progress on synthesis of ceramics core/shell nanostructures," *Processing and Application of Ceramics*, vol. 7, no. 2, pp. 45–62, 2013.

[19] R. G. Chaudhuri and S. Paria, "Core/shell nanoparticles: classes, properties, synthesis mechanisms, characterization, and applications," *Chemical Reviews*, vol. 112, no. 4, pp. 2373–2433, 2011.

[20] L. Su, Y. Jing, and Z. Zhou, "Li ion battery materials with core–shell nanostructures," *Nanoscale*, vol. 3, no. 10, pp. 3967–3983, 2011.

[21] P. Hou, H. Zhang, Z. Zi, L. Zhang, and X. Xu, "Core–shell and concentration-gradient cathodes prepared via co-precipitation reaction for advanced lithium-ion batteries," *Journal of Materials Chemistry A*, vol. 5, no. 9, pp. 4254–4279, 2017.

[22] C. Tang, Y. Mao, J. Xie, Z. Chen, J. Tu, G. Cao, and X. Zhao, "$NiCo_2O_4/MnO_2$ core/shell arrays as a binder-free catalytic cathode for high-performance lithium–oxygen cells," *Inorganic Chemistry Frontiers*, vol. 5, no. 7, pp. 1707–1713, 2018.

[23] J. O. Besenhard, and M. Winter, "Insertion reactions in advanced electrochemical energy storage," *Pure and Applied Chemistry*, vol. 70, no. 3, pp. 603–608, 1998.

[24] M. Beaudin, H. Zareipour, A. Schellenberglabe, and W. Rosehart, "Energy storage for mitigating the variability of renewable electricity sources: an updated review," *Energy for Sustainable Development*, vol. 14, no. 4, pp. 302–314, 2010.

[25] H. Budde-Meiwes , J. Drillkens, B. Lunz, J. Muennix, S. Rothgang, J. Kowal, and D. U. Sauer, "A review of current automotive battery technology and future prospects," *Proceedings of the Institution of Mechanical Engineers, Part D: Journal of Automobile Engineering*, vol. 227, no. 5, pp. 761–776, 2013.

[26] C. A. Mack, "Fifty years of Moore's law," *IEEE Transactions on Semiconductor Manufacturing*, vol. 24, no. 2, pp. 202–207, 2011.

[27] J. H. Pikul, H. G. Zhang, J. Cho, P. V. Braun, and W. P. King, "High-power lithium ion microbatteries from interdigitated three-dimensional bicontinuous nanoporous electrodes," *Nature Communications*, vol. 4, article 1732, 2013.

[28] W. Lai, C. K. Erdonmez, T. F. Marinis, C. K. Bjune, N. J. Dudney, F. Xu, R. Wartena, and Y. Chiang, “Ultrahigh-energy-density microbatteries enabled by new electrode architecture and micropackaging design,” *Advanced Materials*, vol. 22, no. 20, pp. E139–E144, 2010.

[29] A. Patil, V. Patil, D. W. Shin, J. Choi, D. Paik, and S. Yoon, “Issue and challenges facing rechargeable thin film lithium batteries,” *Materials Research Bulletin*, vol. 43, no. 8–9, pp. 1913–1942, 2008.

[30] D. C. Bock, A. C. Marschilok, K. J. Takeuchi, and E. S. Takeuchi, “Batteries used to power implantable biomedical devices,” *Electrochimica Acta*, vol. 84, pp. 155–164, 2012.

[31] J. Liu, “Addressing the Grand Challenges in Energy Storage,” *Advanced Functional Materials*, vol. 23, no. 8, pp. 924–928, 2013.

[32] Y. Yang, Z. Peng, G. Wang, G. Ruan, X. Fan, L. Li, H. Fei, R. H. Hauge, and J. M. Tour, “Three-dimensional thin film for lithium-ion batteries and supercapacitors,” *Acs Nano*, vol. 8, no. 7, pp. 7279–7287, Jan. 2019.

[33] L. NISSAN MOTOR Co., “NISSAN | Nissan Midterm Plan Announcement,” *Nissan-global.com*, 2021. [Online]. Available: https://www.nissan-global.com/EN/DOCUMENT/HTML/FINANCIAL/SPEECH/2011/MTP2011_speech_414_e.html. [Accessed: 09- Jan- 2021].

[34] G. Jeong, Y. Kim, H. Kim, Y. Kim, and H. Sohn, “Prospective materials and applications for Li secondary batteries,” *Energy & Environmental Science*, vol. 4, no. 6, pp. 1986–2002, 2011.

[35] Q. Li, R. Cao, J. Cho, and G. Wu, “Nanostructured carbon-based cathode catalysts for nonaqueous lithium–oxygen batteries,” *Phys. Chem. Chem. Phys.*, vol. 16, no. 27, pp. 13568–13582, 2014.

[36] Q. Lu, Q. Zhao, H. Zhang, J. Li, X. Wang, and F. Wang, “Water dispersed conducting polyaniline nanofibers for high-capacity rechargeable lithium–oxygen battery,” *ACS Macro Letters*, vol. 2, no. 2, pp. 92–95, 2013.

[37] P. G. Bruce, S. A. Freunberger, L. J. Hardwick, and J. Tarascon, “Li–O_2 and Li–S batteries with high energy storage,” *Nature Materials*, vol. 11, pp. 19–29, 2012.

[38] C. Menictas, M. Skyllas-kazacos, and T. M. Lim, *Advances in batteries for medium and large-scale energy storage*, Sawston: Woodhead Publishing, 2014, pp. 609–616.

[39] A. Baasner, M. Piwko, S. Doerfler, H. Althues, and S. Kaskel, “Silicon based anodes and new electrolytes for next generation lithium-ion batteries and lithium-sulfur batteries,” *ECS Meeting Abstracts*, vol. MA2018-01, article 337, 2018.

[40] J. M. Tarascon and M. Armand, “Issues and challenges facing rechargeable

lithium batteries," *Nature*, vol. 414, pp. 359–367, 2001.

[41] V. Etacheri, R. Marom, R. Elazari, G. Salitra, and D. Aurbach, "Challenges in the development of advanced Li-ion batteries: a review," *Energy & Environmental Science*, vol. 4, no. 9, pp. 3243–3262, 2011.

[42] H. Li, Z. Wang, L. Chen, and X. Huang, "Research on advanced materials for Li-ion batteries," *Advanced Materials*, vol. 21, no. 45, pp. 4593–4607, 2009.

[43] Y. Guo, J. Hu, and L. Wan, "Nanostructured materials for electrochemical energy conversion and storage devices," *Advanced Materials*, vol. 20, no. 15, p. 2878–2887, 2008.

[44] T. Placke, R. Kloepsch, S. Dühnen, and M. Winter, "Lithium ion, lithium metal, and alternative rechargeable battery technologies: the odyssey for high energy density," *Journal of Solid State Electrochemistry*, vol. 21, pp. 1939–1964, 2017.

[45] G. Crabtree, E. Kócs, and L. Trahey, "The energy-storage frontier: lithium-ion batteries and beyond," *MRS Bulletin*, vol. 40, no. 12, pp. 1067–1078, 2015.

[46] Y. Nishi, "Lithium ion secondary batteries; past 10 years and the future," *Journal of Power Sources*, vol. 100, no. 1–2, pp. 101–106, 2001.

[47] M. Marca, *Batteries for Sustainability*, New York: Springer, 2012, pp. 5–49.

[48] D. Aurbach, Y. Ein-Eli, O. Chusid, Y. Carmeli, M. Babai, and H. Yamin, "The correlation between the surface chemistry and the performance of Li-carbon intercalation anodes for rechargeable "rocking-chair" type batteries," *Journal of The Electrochemical Society*, vol. 141, no. 3, pp. 603–611, 1994.

[49] D. Han, G. Song, B. Liu, and H. Yan, "Core–shell-structured nickel ferrite/onion-like carbon nanocapsules: an anode material with enhanced electrochemical performance for lithium-ion batteries," *RSC Advances*, vol. 5, no. 53, pp. 42875–42880, 2015.

[50] Y. Idota, T. Kubota, A. Matsufuji, Y. Maekawa, and T. Miyasaka, "Tin-based amorphous oxide: A high-capacity lithium-ion-storage material," *Science*, vol. 276, no. 5317, pp. 1395–1397, 1997.

[51] J. Chen, "Recent progress in advanced materials for lithium ion batteries," *Materials*, vol. 6, no. 1, pp. 156–183, 2013.

[52] Sony Global, "Sony's new nexelion hybrid lithium ion batteries to have thirty-percent more capacity than conventional offering," Sony Global - Sony Global Headquarters, 2005. [Online]. Available: https://www.sony.net/SonyInfo/News/Press/200502/05-006E/. [Accessed: 09-Jan- 2021].

[53] X. L. Wang,; W. Q. Han, J. Chen, and J. Graetz, "Single-crystal intermetallic M−Sn (M = Fe, Cu, Co, Ni) nanospheres as negative electrodes for lithium-ion

batteries," *ACS Appl. Mater. Interfaces*, vol. 2, no. 5, pp. 1548–1551, 2010.

[54] Y. Wan,; J. Liu, C. Liu, S. Ji, and Y. Zhou, "Facile synthesis of $FeSn_2$ alloy nanoparticles as anode materials for lithium-ion batteries," *Energy and Environment Focus*, vol. 2, no. 1, pp. 63–67, 2013.

[55] S. Liang, Y. J. Cheng, J. Zhu, Y. Xia, and P. Müller-Buschbaum, "A chronicle review of nonsilicon (Sn, Sb, Ge)-based lithium/sodium-ion battery alloying anodes," *Small Methods*, vol. 4, no. 8, article 2000218, 2020.

[56] K. T. Lee, Y. S. Jung, and S. M. Oh, "Synthesis of tin-encapsulated spherical hollow carbon for anode material in lithium secondary batteries," *Journal of the American Chemical Society*, vol. 125, no. 19, pp. 5652–5653, 2003.

[57] W. M. Zhang, J. S. Hu, Y. G. Guo, S. F. Zheng, L. S. Zhong, W. G. Song, and L. J. Wan, "Tin-nanoparticles encapsulated in elastic hollow carbon spheres for high-performance anode material in lithium-ion batteries." *Advanced Materials* , vol. 20, pp. 1160–1165, 2008.

[58] X. Liu, S. W. Or, C. Jin, Y. Lv, C. Feng, and Y. Sun, "NiO/C nanocapsules with onion-like carbon shell as anode material for lithium ion batteries," *Carbon*, vol. 60, pp. 215–220, 2013.

[59] Q. Y. Li, Q. C. Pan, G. H. Yang, X. L. Lin, Z. X. Yan, H. Q. Wang, and Y. G. Huang, "Synthesis of $Sn/MoS_2/C$ composites as high-performance anodes for lithium-ion batteries," *Journal of Materials Chemistry A*, vol. 3, no. 40, pp. 20375–20381, 2015.

[60] K. Kravchyk, L. Protesescu, M. I. Bodnarchuk, F. Krumeich, M. Yarema, M. Walter, C. Guntlin, and M. V. Kovalenko, "Monodisperse and inorganically capped Sn and Sn/SnO_2 nanocrystals for high-performance Li-ion battery anodes," *Journal of the American Chemical Society*, vol. 135, no. 11, pp. 4199–4202, 2013.

[61] P. Tang, H.R. Jiang, and X.B. Zhu, "Advances and challenges in lithium-air batteries," *Applied Energy*, vol. 204, pp. 780–806, 2017.

[62] M. Asadi, B. Sayahpour, P. Abbasi, A. T. Ngo, K. Karis, J. R. Jokisaari, C. Liu, B. Narayanan, M. Gerard, P. Yasaei, X. Hu, A. Mukherjee, K. C. Lau, R. S. Assary, F. Khalili-Araghi, R. F. Klie, L. A. Curtiss, and A. Salehi-Khojin, "A lithium–oxygen battery with a long cycle life in an air-like atmosphere," *Nature*, vol. 555, no. 7697, pp. 502–506, 2018.

[63] T. Liu, J. P. Vivek, E. W. Zhao, J. Lei, N. Garcia-Araez, and C. P. Grey, "Current challenges and routes forward for nonaqueous lithium–air batteries," *Chemical Reviews*, vol. 120, no. 14, pp. 6558–6625, 2020.

[64] T. Zhang, N. Imanishi, S. Hasegawa, A. Hirano, J. Xie, Y. Takeda, O. Yamamoto,

and N. Sammes, "Water-stable lithium anode with the three-layer construction for aqueous lithium–air secondary batteries," *Electrochemical and Solid-State Letters*, vol. 12, no. 7, article A132, 2009.

[65] P. He, Y. Wang, and H. Zhou, "A Li-air fuel cell with recycle aqueous electrolyte for improved stability," *Electrochemistry Communications*, vol. 12, no. 12, pp. 1686–1689, 2010.

[66] Y. Sun, "Lithium ion conducting membranes for lithium-air batteries," *Nano Energy*, vol. 2, no. 5, pp. 801–816, 2013.

[67] X. Liu, B. Cui, S. Liu, and Y. Chen, "Progress of non-aqueous electrolyte for Li-air batteries," *Journal of Materials Science and Chemical Engineering*, vol. 3, no. 5, pp. 1–8, 2015.

[68] K. M. Abraham and Z. Jiang, "A polymer electrolyte-based rechargeable lithium/oxygen battery," *Journal of The Electrochemical Society*, vol. 143, no. 1, pp. 1–5, 1996.

[69] K. M. Abraham and Z. Jiang, "Solid polymer electrolyte-based oxygen batteries," US Patent no. 5, 510, 209, 1996.

[70] M. V. Reddy, A. Mauger, C. M. Julien, A. Paolella, and K. Zaghib, "Brief history of early lithium-battery development," *Materials*, vol. 13, no. 8, article 1884, 2020.

[71] J. Xiao, D. Wang, W. Xu, D. Wang, R. E. Williford, J. Liu, and J. Zhang, "Optimization of air electrode for Li/air batteries," *Journal of The Electrochemical Society*, vol. 157, no. 4, article A487, 2010.

[72] G. Q. Zhang, J. P. Zheng, R. Liang, C. Zhang, B. Wang, M. Hendrickson, and E. J. Plichta, "Lithium–air batteries using SWNT/CNF buckypapers as air electrodes," *Journal of The Electrochemical Society*, vol. 157, no. 8, article A953, 2010.

[73] S. A. Freunberger, Y. Chen, N. E. Drewett, L. J. Hardwick, F. Bardé, and P. G. Bruce, "The lithium-oxygen battery with ether-based electrolytes," *Angewandte Chemie International Edition*, vol. 50, no. 37, pp. 8609–8613, 2011.

[74] Y. C. Lu, H. A. Gasteiger, and Y. Shao-Horn, "Catalytic activity trends of oxygen reduction reaction for nonaqueous Li-air batteries," *Journal of the American Chemical Society*, vol. 133, no. 47, pp. 19048–19051, 2011.

[75] M. A. Rahman, X. Wang, and C. Wen, "A review of high energy density lithium–air battery technology," *Journal of Applied Electrochemistry*, vol. 44, pp. 5–22, 2013.

[76] A. Kraytsberg and Y. Ein-Eli, "Review on Li–air batteries—opportunities, limitations and perspective," *Journal of Power Sources*, vol. 196, no. 3, pp. 886–893, 2011.

[77] Y. C. Lu, H. A. Gasteiger, E. Crumlin, R. M. Jr, and Y. Shao-Horn, “Electrocatalytic activity studies of select metal surfaces and implications in Li-air batteries,” *Journal of The Electrochemical Society*, vol. 157, no. 9, article A1016, 2010.

[78] Y. C. Lu, Z. Xu, H. A. Gasteiger, S. Chen, K. Hamad-Schifferli, and Y. Shao-Horn, “Platinum−gold nanoparticles: a highly active bifunctional electrocatalyst for rechargeable lithium−air batteries,” *Journal of the American Chemical Society*, vol. 132, no. 35, pp. 12170–12171, 2010.

[79] Z. Peng, S. A. Freunberger, Y. Chen, and P. G. Bruce, “A reversible and higher-rate Li-O_2 battery,” *Science*, vol. 337, no. 6094, pp. 563–566, 2012.

[80] C. C. Li, W. Zhang, H. Ang, H. Yu, B. Y. Xia, X. Wang, Y. H. Yang, Y. Zhao, H. H. Hng, and Q. Yan, “Compressed hydrogen gas-induced synthesis of Au–Pt core–shell nanoparticle chains towards high-performance catalysts for Li–O_2 batteries,” *Journal of Materials Chemistry A*, vol. 2, no. 27, pp. 10676–10681, 2014.

[81] Y. Yu, B. Zhang, Y. B. He, Z. D. Huang, S. W. Oh, and J. K. Kim, “Mechanisms of capacity degradation in reduced graphene oxide/α-MnO_2 nanorod composite cathodes of Li–air batteries,” *Journal of Materials Chemistry A*, vol. 1, no. 4, pp. 1163–1170, 2013.

[82] C. S. Park, K. S. Kim, and Y. J. Park, “Carbon-sphere/Co_3O_4 nanocomposite catalysts for effective air electrode in Li/air batteries,” *Journal of Power Sources*, vol. 244, pp. 72–79, 2013.

[83] Z. Sadighi, J. Huang, L. Qin, S. Yao, J. Cui, and J. K. Kim, “Positive role of oxygen vacancy in electrochemical performance of $CoMn_2O_4$ cathodes for Li-O_2 batteries,” *Journal of Power Sources*, vol. 365, pp. 134–147, 2017.

[84] S. Ma, L. Sun, L. Cong, X. Gao, C. Yao, X. Guo, L. Tai, P. Mei, Y. Zeng, H. Xie, and R. Wang, “Multiporous $MnCo_2O_4$ microspheres as an efficient bifunctional catalyst for nonaqueous Li–O_2 batteries,” *The Journal of Physical Chemistry C*, vol. 117, no. 49, pp. 25890–25897, 2013.

[85] A. Chatterjee, S. W. Or, and Y. Cao, “Transition metal hollow nanocages as promising cathodes for the long-term cyclability of Li–O_2 batteries,” *Nanomaterials*, vol. 8, no. 5, article 308, 2018.

[86] D. Oh, J. Qi, Y. C. Lu, Y. Zhang, Y. Shao-Horn, and A. Belcher, “Biologically enhanced cathode design for improved capacity and cycle life for lithium-oxygen batteries,” *Nature Communications*, vol. 4, article 2756, 2013.

[87] Y. P. Zheng, K. Song, J. Jung, C. Li, Y. U. Heo, M. S. Park, M. Cho, Y. M. Kang, and K. Cho, “Critical descriptor for the rational design of oxide-based catalysts in rechargeable Li-O_2 batteries: surface oxygen density,” *Chemistry of Materials*, vol.

27, no. 9, p. 3243–3249, 2015.

[88] B. Liu, Y. Sun, L. Liu, S. Xu, and X. Yan, "Advances in manganese-based oxides cathodic electrocatalysts for Li-air batteries," *Advanced Functional Materials*, vol. 28, no. 15, article 1704973, 2018.

[89] K. N. Jung, J. I. Lee, S. Yoon, S. H. Yeon, W. Chang, K. H. Shina, and J. W. Lee, "Manganese oxide/carbon composite nanofibers: electrospinning preparation and application as a bi-functional cathode for rechargeable lithium–oxygen batteries," *Journal of Materials Chemistry*, vol. 22, no. 41, pp. 21845, 2012.

[90] Y. Cao and S. W. Or, "Enhanced cyclability in rechargeable Li–O_2 batteries based on Mn_3O_4 hollow nanocage/ketjenblack catalytic air cathode," *IEEE Transactions on Magnetics*, vol. 52, no. 7, pp. 1–4, 2016.

[91] A. Ramírez, P. Hillebrand, D. Stellmach, M. M. May, P. Bogdanoff, and S. Fiechter, "Evaluation of MnO_x, Mn_2O_3, and Mn_3O_4 electrodeposited films for the oxygen evolution reaction of water," *The Journal of Physical Chemistry C*, vol. 118, no. 26, pp. 14073–14081, 2014.

[92] V. Bose, K. Maniammal, G. Madhu, C. L. Veenas, A. S. A. Raj, and V. Biju, "DC electrical conductivity of nanocrystalline Mn_3O_4 synthesized through a novel sol-gel route," *IOP Conference Series: Materials Science and Engineering*, vol. 73, article 012084, 2015.

[93] H. Dong, Y. Wang, P. Tang, H. Wang, K. Li, Y. Yin, and S. Yang, "A novel strategy for improving performance of lithium-oxygen batteries," *Journal of Colloid and Interface Science*, vol. 584, pp. 246–252, 2021.

[94] N. Mahne, O. Fontaine, M. O. Thotiyl, M. Wilkening, and S. A. Freunberger, "Mechanism and performance of lithium–oxygen batteries – a perspective," *Chemical Science*, vol. 8, no. 10, pp. 6716–6729, 2017.

[95] C. Q. Zhang, J. P. Tu, X. H. Huang, Y. F. Yuan, S. F. Wang, and F. Mao, "Preparation and electrochemical performances of nanoscale $FeSn_2$ as anode material for lithium ion batteries," *Journal of Alloys and Compounds*, vol. 457, pp. 81–85, 2008.

[96] J. P. Lei, X. L. Dong, X. G. Zhu, M. K. Lei, H. Huang, X. F. Zhang, B. Lu, W. J. Park, and H. S. Chung, "Formation and characterization of intermetallic Fe-Sn nanoparticles synthesized by an arc discharge method," *Intermetallics*, vol. 15, no. 12, pp. 1589–1594, 2007.

[97] J. M. Lee, W. S. Chang, B.C. Yu, H. Kim, D. Im, S.G. Doo, and H. J. Sohn, "Enhancement of cyclability using recombination reaction of Cu for Sn_2Fe nanocomposite anode for lithium-ion batteries," *Electrochemistry Communications*, vol. 12, no. 7, pp. 928–932, 2010.

[98] S. K. Yoon, J. M. Lee, H. S. Kim, D. M. Im, S. G. Doo, and H. J. Sohn, "An Sn–Fe/carbon nano composite as an alternative anode material for rechargeable lithium batteries," *Electrochimica Acta*, vol. 54, no. 10, pp. 2699–2705, 2009.

[99] C. J. Liu, F. H. Xue, H. Huang, X. H. Yu, C. J. Xie, M. S. Shi, G. Z. Cao, Y. G. Jung, and X. L. Dong, "Preparation and electrochemical properties of Fe-Sn (C) nanocomposites as anode for lithium-ion batteries," *Electrochimica Acta*, vol. 129, pp. 93–99, 2014.

[100] M. Armbrüster, W. Schnelle,; R. Cardoso-Gil, and Y. Grin, "Chemical bonding in compounds of the $CuAl_2$ family: $MnSn_2$, $FeSn_2$ and $CoSn_2$," *Chemistry—A European Journal*. vol. 16, no. 34, pp. 10357–10365, 2010.

[101] D. Han, S. W. Or, X. Dong, and B. Liu, "$FeSn_2$/defective onion-like carbon core-shell structured nanocapsules for high-frequency microwave absorption," *Journal of Alloys and Compounds*. vol. 695, pp. 2605–2611, 2017.

[102] D. Pech, M. Brunet, H. Durou, P. Huang, V. Mochalin, Y. Gogotsi, P. L. Taberna, and P. Simon, "Ultrahigh-power micrometre-sized supercapacitors based on onion-like carbon," *Nature Nanotechnology*. vol. 5, pp. 651–654, 2010.

[103] M. Zeiger, N. Jäckel, V. N. Mochalin, and V. Presser, "Review: Carbon onions for electrochemical energy storage," *Journal of Materials Chemistry A*, vol. 4, no. 9, pp. 3172–3196, 2016.

[104] K. L. Van-Aken, K. Maleski, T. S. Mathis, J. P. Breslin, and Y. Gogotsi, "Processing of onion-like carbon for electrochemical capacitors," *ECS Journal of Solid State Science and Technology*, vol. 6, pp. M3103–M3108, 2017.

[105] S. Wang, M. He, M. Walter, F. Krumeich, K. V. Kravchyk, and M. V. Kovalenko, "Monodisperse $CoSn_2$ and $FeSn_2$ nanocrystals as high-performance anode materials for lithium-ion batteries," *Nanoscale*, vol. 10, no. 15, pp. 6827–6831, 2018.

[106] M. Armbruster, M. Schmidt, R. Cardoso-Gil, H. Borrmann, and Y. Grin, "Crystal structures of iron distannide, $FeSn_2$, and cobalt distannide, $CoSn_2$," *Zeitschrift für Kristallographie – New Crystal Structures*, vol. 222, pp. 83–84, 2007.

[107] U. G. Nwokeke,; R. Alcántara, J. L. Tirado, R. Stoyanova, M. Yoncheva, and E. Zhecheva, "Electron paramagnetic resonance, X-ray diffraction, mössbauer spectroscopy, and electrochemical studies on nanocrystalline $FeSn_2$ obtained by reduction of salts in tetraethylene glycol," *Chemistry of Materials*, vol. 22, no. 7, pp. 2268–2275, 2010.

[108] X. Liu, N. Wu, C. Cui, P. Zhou, and Y. Sun, "Enhanced rate capability and cycling stability of core/shell structured $CoFe_2O_4$/onion-like C nanocapsules for lithium-ion battery anodes," *Journal of Alloys and Compounds*, vol. 644, pp. 59–65, 2015.

[109] L. Jiang, Z. Wang, D. Geng, Y. Lin, Y. Wang, J. An, J. He, D. Li, W. Liu, and Z. Zhang, “Structure and electromagnetic properties of both regular and defective onion-like carbon nanoparticles,” *Carbon*, vol. 95, pp. 910–918, 2015.

[110] C.V. Thompson, “On the role of diffusion in phase selection during reactions at interfaces,” *Journal of Materials Research and Technology*, vol. 7, pp. 367–373, 1992.

[111] J. Wright, “Growth mechanisms of carbon onions obtained by thermal treatment-diamond films,” *Texas Powerful Smart*, 2019. [Online]. Available: https://www.texaspowerfulsmart.com/diamond-films/growth-mechanisms-of-carbon-onions-obtained-by-thermal-treatment.html [Accessed: 29- Apr- 2021].

[112] J. Leibowitz, E. Allcorn, and A. Manthiram, “$FeSn_2$-TiC nanocomposite alloy anodes for lithium ion batteries,” *Journal of Power Sources*, vol. 295, pp. 125–130, 2015.

[113] C. Q. Zhang, J. P. Tu, X. H. Huang, Y. F. Yuan, S. F. Wang, and F. Mao, “Preparation an electrochemical performances of nanoscale $FeSn_2$ as anode material for lithium ion batteries,” *Journal of Alloys and Compounds*, vol. 457, no. 1–2, pp. 81–85, 2008.

[114] Y. Liu and D.Y. Kim, “Enhancement of capacitance by electrochemical oxidation of nanodiamond derived carbon nano-onions,” *Electrochimica Acta*, vol. 139, pp. 82–87, 2014.

[115] Y. Yuan, K. Amine, J. Lu, and R. Shahbazian-Yassar, “Understanding materials challenges for rechargeable ion batteries with in situ transmission electron microscopy,” *Nature Communications*, vol. 8, article 15806, 2017.

[116] S. J. An, J. Li, C. Daniel, D. Mohanty, S. Nagpure, and D. L. Wood, “The state of understanding of the lithium-ion-battery graphite solid electrolyte interphase (SEI) and its relationship to formation cycling,” *Carbon*, vol. 105, pp. 52–76, 2016.

[117] X. Liu, Y. Wu, X. Li, J. Yu, and Y. Sun, “FeS@onion-like carbon nanocapsules embedded in amorphous carbon for the lithium ion batteries with excellent cycling stability,” *Ceramics International*, vol. 44, pp. 13654–13661, 2018.

[118] N. Yabuuchi, K. Kubota, Y. Aoki, and S. Komaba, “Understanding particle-size-dependent electrochemical properties of Li_2MnO_3-based positive electrode materials for rechargeable lithium batteries,” *The Journal of Physical Chemistry C*, vol. 120, no. 2, pp. 875–885, 2016.

[119] X. Li, X. He, Y. Xu, L. Huang, J. Li, S. Sun, and J. Zhao, “Superiority of the bi-phasic mixture of a tin-based alloy nanocomposite as the anode for lithium ion batteries,” *Journal of Materials Chemistry A*, vol. 3, no. 7, pp. 3794–3800, 2015.

[120] T. Osaka, D. Mukoyama, and H. Nara, “Review—development of diagnostic

process for commercially available batteries, especially lithium ion battery, by electrochemical impedance spectroscopy," *Journal of the Electrochemical Society,* vol. 162, no. 14, pp. A2529–A2537, 2015.

[121] F. Qin, K. Zhang, J. Fang, Y. Lai, Q. Li, Z. Zhang, and J. Li, "High performance lithium sulfur batteries with a cassava-derived carbon sheet as a polysulfides inhibitor," *New Journal of Chemistry,* vol. 38, pp. 4549–4554, 2014.

[122] S. Chaitoglou, M.R. Sanaee, N. Aguiló-Aguayo, and E. Bertran, "Arc-discharge synthesis of iron encapsulated in carbon nanoparticles for biomedical applications," *Journal of Nanomaterials,* vol. 2014, article 178524, 2014.

[123] A. Dutta, D. Gupta, A. K. Patra, B. Saha, and A. Bhaumik, "Synthesis of 5-hydroxymethylfurural from carbohydrates using large-pore mesoporous tin phosphate," *ChemSusChem,* vol. 7, pp. 925–933, 2014.

[124] J. T. Lee, Y. Zhao, H. Kim, W. I. Cho, and G. Yushin, " Sulfur infiltrated activated carbon cathodes for lithium sulfur cells: the combined effects of pore size distribution and electrolyte molarity," *Journal of Power Sources*, vol. 248, pp.752–761, 2014.

[125] X. Lin, L. Zhou, T. Huang, and A. Yu, "Hierarchically porous honeycomb-like carbon as a lithium–oxygen electrode," *Journal of Materials Chemistry A*, vol. 1, no. 4, pp. 1239–1245, 2013.

[126] K. H. Kwak, D. W. Kim, Y. Kang, and J. Suk, "Hierarchical Ru- and RuO_2-foams as high performance electrocatalysts for rechargeable lithium–oxygen batteries," *Journal of Materials Chemistry A*, vol. 4, no. 42, pp. 16356–16367, 2016.

[127] J. Lu, Y. Lei, K. Lau, X. Luo, P. Du, J. Wen, R. S. Assary, U. Das, D. J. Miller, J. W. Elam, H. M. Albishri, D. A. El-Hady, Y. Sun, L. A. Curtiss, and K. Amine, "A nanostructured cathode architecture for low charge overpotential in lithium-oxygen batteries," *Nature Communications*, vol. 4, article 2383, 2013.

[128] S. Meini, N. Tsiouvaras, K. U. Schwenke, M. Piana, H. Beyer, L. Langea, and H. A. Gasteigera, "Rechargeability of Li–air cathodes pre-filled with discharge products using an ether-based electrolyte solution: implications for cycle-life of Li–air cells," *Physical Chemistry Chemical Physics*, vol. 15, no. 27, pp. 11478–11493, 2013.

[129] I. Jung, H. J. Kwon, M. Kim, D. Kim, J. Kim, H. Lee, D. Yun, S. Byun, D. Yu, H. An, J. Jang, D. Im, and H. Lee, "Rapid oxygen diffusive lithium–oxygen batteries using a restacking-inhibited, free-standing graphene cathode film," *Journal of Materials Chemistry A*, vol. 7, no. 17, pp. 10397–10404, 2019.

[130] C. Lin, K. Chuang, C. Lin, C. Tsay, and C. Chen, "Manganese oxide films

prepared by sol–gel process for supercapacitor application," *Surface and Coatings Technology*, vol. 202, no. 4–7, pp. 1272–1276, 2007.

[131] E. Lee, T. Lee, and B. S. Kim, "Electrospun nanofiber of hybrid manganese oxides for supercapacitor: Relevance to mixed inorganic interfaces," *Journal of Power Sources*, vol. 255, pp. 335–340, 2014.

[132] A. T. Chidembo, S. H. Aboutalebi, K. Konstantinov, C. J. Jafta, H. K. Liu, and K. I. Ozoemena, "In situ engineering of urchin-like reduced graphene oxide–Mn_2O_3–Mn_3O_4 nanostructures for supercapacitors," *RSC Advances*, vol. 4, no. 2, pp. 886–892, 2014.

[133] M. Augustin, D. Fenske, I. Bardenhagen, A. Westphal, M. Knipper, T. Plaggenborg, J. Kolny-Olesiak, and J. Parisi, "Manganese oxide phases and morphologies: A study on calcination temperature and atmospheric dependence," *Beilstein Journal of Nanotechnology*, vol. 6, pp. 47–59, 2015.

[134] B.D. Cullity and S.R. Stock, *Elements of X-ray Diffraction*, New York: Prentice-Hall, 2001, pp. 96–102.

[135] C. V. Brolly, J. Parnell, and S. Bowden, "Raman spectroscopy: Caution when interpreting organic carbon from oxidising environments," *Planetary and Space Science*, vol. 121, pp. 53–59, 2016

[136] O. Beyssac, B. Goffé, C. Chopin, and J. N. Rouzaud, "Raman spectra of carbonaceous material in metasediments: a new geothermometer," *Journal of Metamorphic Geology*, vol. 20, no. 9, pp.859–871, 2002

[137] Z. L. Xu, Y. Gang, M. A. Garakani, S. Abouali, J. Q. Huang, and J. K. Kim, "Carbon-coated mesoporous silicon microsphere anodes with greatly reduced volume expansion," *Journal of Materials Chemistry A*, vol. 4, no. 16, pp.6098–6106, 2016

[138] M. Youssry, F. Z. Kamand, M. I. Magzoub, and M. S. Nasser, "Aqueous dispersions of carbon black and its hybrid with carbon nanofibers," *RSC Advances*, vol. 8, no. 56, pp. 32119–32131, 2018.

[139] A. M. Toufiq, F. P. Wang, and Q. U. Javed, "Synthesis, characterization and photoluminescent properties of 3D nanostructures self-assembled with Mn_3O_4 nanoparticles," *Materials Express*, vol. 4, no. 3, pp. 258–262, 2014.

[140] A. Shahverdi, K. S. Kim, Y. Alinejad, G. Soucy, and J. Mostaghimi, "Selective oxidation of excess amorphous carbon during single-walled carbon nanotubes synthesis by induction thermal plasma process," *Journal of Nano Research*, vol. 2, pp. 800–812, 2009.

[141] M. Ujihara, M. M. M. Ahmed, T. Imae, and Y. Yamauchi, "Massive-exfoliation of magnetic graphene from acceptor-type GIC by long-chain alkyl amine," *Journal*

of Materials Chemistry A, vol. 2, no. 12, p. 4244, 2014.

[142] Z. L. Xu, K. Cao, S. Abouali, M. A. Garakani, J. Huang, J. Huang, E. K. Heidari, H. Wang, and J. Kim, “Study of lithiation mechanisms of high performance carbon-coated Si anodes by in-situ microscopy,” *Energy Storage Materials*, vol. 3, pp. 45–54, 2016.

[143] D. Geng, N. Ding, T. S. Hor, S. W. Chien, Z. Liu, D. Wuu, X. Sun, and Yun Zong, “From lithium-oxygen to lithium-air batteries: challenges and opportunities,” *Advanced Energy Materials*, vol. 6, no. 9, article 1502164, 2016.

[144] Y. Bae, D. H. Ko, S. Lee, H. D. Lim, Y. J. Kim, H. S. Shim, H. Park, Y. Ko, S. K. Park, H. J. Kwon, H. Kim, H. T. Kim, Y. S. Min, D. Im, and K. Kang, “Enhanced stability of coated carbon electrode for Li–O_2 batteries and its limitations,” *ECS Meeting Abstracts*, vol. 8, no. 16, 2018.

[145] C. O. Laoire, S. Mukerjee, K. M. Abraham, E. J. Plichta, and M. A. Hendrickson, “Elucidating the mechanism of oxygen reduction for lithium-air battery applications,” *The Journal of Physical Chemistry C*, vol. 113, no. 46, pp. 20127–20134, 2009.

[146] V. G. Anju and S. Sampath, “Stable, rechargeable lithium − oxygen battery in liquid and gel-based electrolytes,” *Electrochimica Acta*, vol. 252, pp. 119–126, 2017.

[147] N. Mahne, S. E. Renfrew, B. McCloskey, and S. A. Freunberger, “Electrochemical oxidation of lithium carbonate generates singlet oxygen,” *Angewandte Chemie International Edition*, vol. 57, no. 19, pp. 5529–5533, 2018.

[148] B. D. McCloskey, D. S. Bethune, R. M. Shelby, G. Girishkumar, and A. C. Luntz, “Solvents’ critical role in nonaqueous lithium–oxygen battery electrochemistry,” *The Journal of Physical Chemistry Letters*, vol. 2, no. 10, pp. 1161–1166, 2011.

[149] Z. Sadighi, J. Liu, L. Zhao, F. Ciucci, and J. K. Kim, “Metallic MoS_2 nanosheets: multifunctional electrocatalyst for the ORR, OER and Li–O_2 batteries,” *Nanoscale*, vol. 10, no. 47, pp. 22549–22559, 2018.

[150] J. Yang, D. Zhai, H. Wang, K. C. Lau, J. A. Schlueter, P. Du, D. J. Myers, Y. Sun, L. A. Curtiss, and K. Amine, “Evidence for lithium superoxide-like species in the discharge product of a Li–O_2 battery,” *Physical Chemistry Chemical Physics*, vol. 15, no. 11, pp. 3764–3771, 2013.

[151] S.M. Lee, S.H. Lee, and J.S. Roh, "Analysis of activation process of carbon black based on structural parameters obtained by XRD analysis," *Crystals*, vol. 11, no. 153, pp. 1–11, 2021.

[152] Z. Sadighi, J. Liu, F. Ciucci, and J. K. Kim, “Mesoporous $MnCo_2S_4$ nanosheet

arrays as an efficient catalyst for Li–O_2 batteries," *Nanoscale*, vol. 10, no. 33, pp. 15588–15599, 2018.

[153] E. Fermi, "Statistical method to determine some properties of atoms," *Rendiconti Lincei*, vol. 6, pp. 602–607, 1927.

[154] P. A. Dirac, "Note on exchange phenomena in the Thomas atom," *Proceedings of the Cambridge Philosophical Society,* vol. 26, no. 3, pp. 376–385, 1930.

[155] E. Teller, "On the stability of molecules in the Thomas-Fermi theory," *Reviews of Modern Physics*, vol. 34, no. 4, pp. 627–631, 1962.

[156] P. Hohenberg and W. Kohn, "Inhomogeneous electron gas," *Physical Review*, vol. 136, no. 3, pp. B864–B871, 1964.

[157] W. Kohn and L. J. Sham, "Self-consistent equations including exchange and correlation effects," *Physical Review*, vol. 140, no. 4, pp. A1133–A1138, 1965.

[158] L. Hedin and B. I. Lundqvist, "Explicit local exchange-correlation potentials," *Journal of Physics C: Solid State Physics*, vol. 4, no. 14, pp. 2064–2083, 1971.

[159] J. P. Perdew and K. Burke, "Comparison shopping for a gradient-corrected density functional," *International Journal of Quantum Chemistry*, vol. 57, no. 3, pp. 309–319, 1996.

[160] J. P. Perdew, J. A. Chevary, S. H. Vosko, K. A. Jackson, M. R. Pederson, D. J. Singh, and C. Fiolhais, "Atoms, molecules, solids, and surfaces: Applications of the generalized gradient approximation for exchange and correlation," *Physical Review B*, vol. 48, no. 7, pp. 4978–4978, 1992.

[161] P. Giannozzi, S. Baroni, N. Bonini, M. Calandra, R. Car, C. Cavazzoni, D. Ceresoli, G. L. Chiarotti, M. Cococcioni, I. Dabo, A. D. Corso, S. Gironcoli1, S. Fabris, G. Fratesi, R. Gebauer, U. Gerstmann, C. Gougoussis, A. Kokalj, M. Lazzeri, L. Martin-Samos, N. Marzari, F. Mauri, R. Mazzarello, S. Paolini, A. Pasquarello, L. Paulatto, C. Sbraccia, S. Scandolo, G. Sclauzero, A. P. Seitsonen, A. Smogunov, P. Umari, and R. M. Wentzcovitch, "QUANTUM ESPRESSO: a modular and open-source software project for quantum simulations of materials," *Journal of Physics: Condensed Matter*, vol. 21, no. 39, article 395502, 2009.

[162] P. Giannozzi, O. Andreussi, and T.Brumme, "Advanced capabilities for materials modelling with Quantum ESPRESSO," *J. Physics: Condensed Matter*, vol. 29, no. 46, article 465901, 2017.

[163] J. P. Perdew, K. Burke, and M. Ernzerhof, "Generalized Gradient Approximation Made Simple," *Physical Review Letters*, vol. 77, no. 18, pp. 3865–3868, 1996.

[164] S. Grimme, J. Antony, S. Ehrlich, and H. Krieg, "A consistent and accurate ab initio parametrization of density functional dispersion correction (DFT-D) for the

94 elements H-Pu," *The Journal of Chemical Physics*, vol. 132, no. 15, article 154104, 2010.

[165] D. Vanderbilt, "Soft self-consistent pseudopotentials in a generalized eigenvalue formalism," *Physical Review B*, vol. 41, no. 11, pp. 7892–7895, 1990.

[166] K. Lejaeghere, G. Bihlmayer, and T. Björkman, "Reproducibility in density functional theory calculations of solids," *Science*, vol. 351, no. 6280, pp. AAD 3000-1–3000-7, 2016.

[167] S. Yao, J. Cui, Z. Lu, Z. L. Xu, L. Qin, J. Huang, Z. Sadighi, F. Ciucci, and J. K. Kim, "Unveiling the unique phase transformation behavior and sodiation kinetics of 1D van der Waals Sb_2S_3 anodes for sodium ion batteries," *Advanced Energy Materials*, vol. 7, no. 8, article 1602149, 2016.

[168] L. Wang, Y. Zhang, Z. Liu, L. Guo, and Z. Peng, "Understanding oxygen electrochemistry in aprotic $Li–O_2$ batteries," *Green Energy and Environment*, vol. 2, no. 3, pp. 186–203, 2017.

[169] D. Aurbach, B. D. McCloskey, L. F. Nazar, and P. G. Bruce, "Advances in understanding mechanisms underpinning lithium–air batteries," *Nature Energy*, vol. 1, article 16128, 2016.

[170] G. Fernando, *Metallic multilayers and their applications: theory, experiments, and applications related to thin metallic multilayers.*, Amsterdam: Elsevier, 2008, pp. 11.

[171] Y. D. Gong, W. Ding, and Z. P. Li, "Inverse spinel cobalt-iron oxide and N-doped graphene composite as an efficient and durable bifuctional catalyst for $Li-O_2$ batteries," *ACS Catalysis*, vol. 8, no. 5, pp. 4082–4090, 2018.